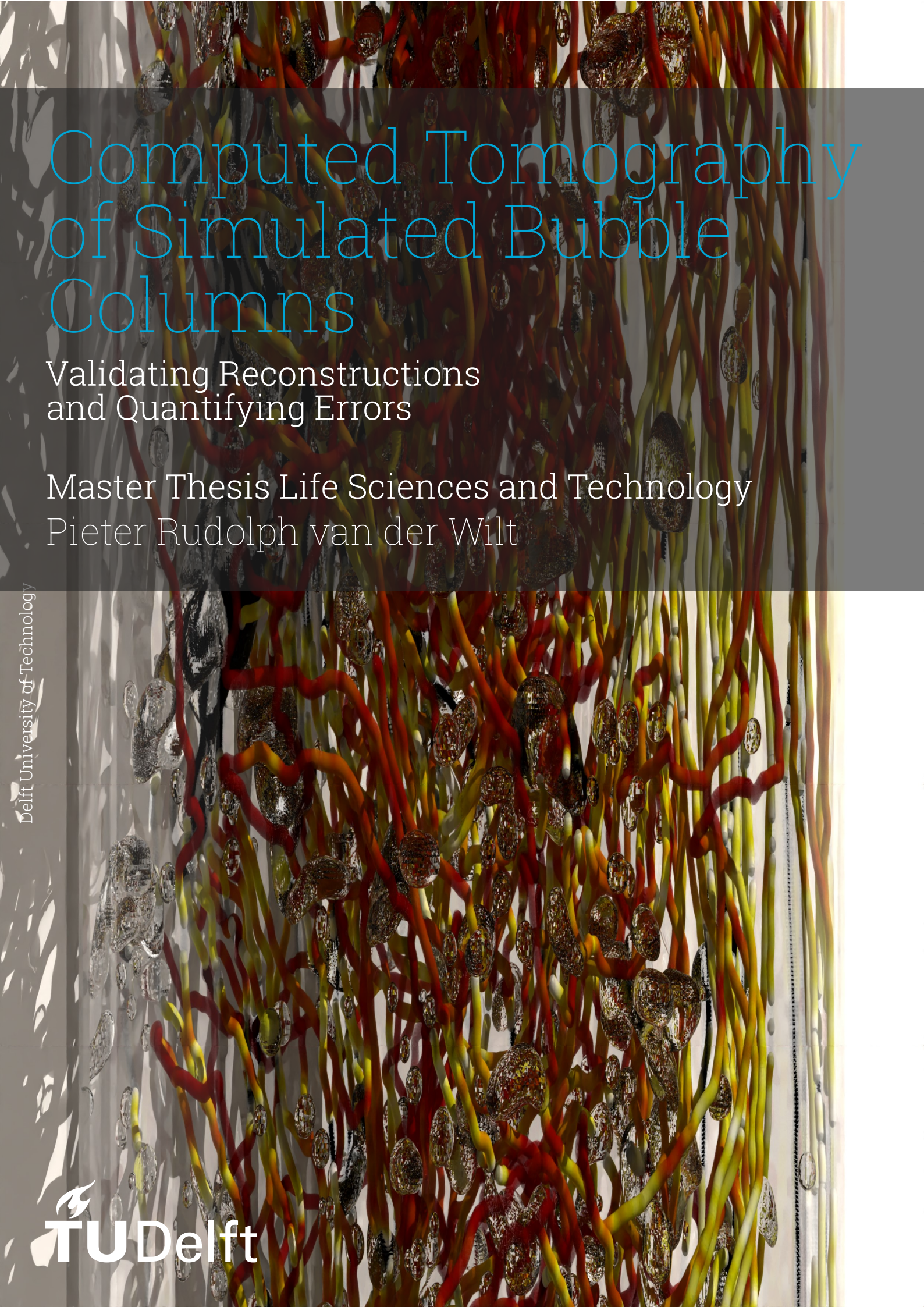

Computed Tomography of Simulated Bubble Columns

Validating Reconstructions and Quantifying Errors

Master Thesis Life Sciences and Technology

Pieter Rudolph van der Wilt

Delft University of Technology

TU Delft

Computed Tomography of Simulated Bubble Columns

Validating Reconstructions and Quantifying Errors

by

Pieter Rudolph van der Wilt

to obtain the degree of Master of Science

at the Delft University of Technology,

to be defended publicly on Tuesday May 27, 2025 at 9:30 AM.

Student number:	5031850	
Project duration:	September 2, 2024 – May 27, 2024	
Daily supervisor:	Ir. R. Volger	TU Delft
Thesis committee:	Dr. ir. C. Haringa,	TU Delft (supervisor)
	Dr. ir. T.M.J. Nijssen,	TU Delft
	Prof. dr. S. Kenjereš	TU Delft
Section:	Applied Sciences, Bioprocess Engineering	

Cover: Ray traced render of the Volger bubble column (case #3) showing velocity streamlines by Pieter van der Wilt (CC-BY-NC-SA 4.0)

Style: TU Delft Report Style, with modifications by Daan Zwaneveld & Pieter van der Wilt

An electronic version of this thesis will be available at http://repository.tudelft.nl/.

TU Delft

Acknowledgements

Writing a thesis is no easy feat. Without the help of many people this would not have been possible. First, I would like to thank Rik Volger for being my daily supervisor. He has a critical eye for determining what is relevant and irrelevant information. His feedback has been incredibly valuable. In the same vein, I would like to thank Cees Haringa as the thesis supervisor. Having supervised me during my bachelor thesis, he has played an important role in developing my passion for (computational) fluid dynamics. I would also like to thank Sam den Hartog for the discussion on the challenges of tomography and for helping me with some of the diagrams in the thesis as well as the rest of the Bubble Buddies. In regards to understanding the mathematics behind tomography, I want to thank Adriaan Graas and Felix Lucka from the Centrum Wiskunde & Informatica for helping me with the maths and recommending the books by Buzug and Hanssen. In regards to M-Star CFD, I want to thank Ramon van Valderen and Johannes Wutz for all the help with understanding the cumulant lattice Boltzmann method and the UDFs / inner workings of M-Star respectively. Finally, I want to thank all the PhD candidates, technicians, professors and especially the other students in the BPE group for providing a welcoming, friendly and engaging environment.

Pieter Rudolph van der Wilt
Delft, May 2025

Abstract

As the world increasingly decarbonises, there is an increasing pressure on chemical manufacturing to move away from fossil carbon sources. Industrial bioprocesses provide one such alternative for fossil carbon. Bubble columns as a bioreactor type are particularly well suited to such large scale applications. However, models of bubble columns, whether based on design correlations or computational fluid dynamics, have been shown to break down when air-water systems are replaced with systems containing actual fermentation broth. The additional broth components can significantly affect interphase mass transfer through e.g. limiting bubble breakup, which can in turn make or break the economics of a bioprocess [1]. Experimental data on the effects of broth components on the physics in bubble columns is essential to develop better models. Gathering such data requires experimental methods capable of penetrating the industrially-relevant but opaque churn-turbulent flows. A promising method for determining the state of a large section of the bubble field in a bubble column is X-ray computed tomography. The TU Delft X-ray tomography setup seeks to achieve this using three source-detector pairs capable of capturing X-ray data at high frame rates. However, in order to be able to apply any experimental technique, it must first be validated and the sources of and magnitude of its various measurement errors must be quantified.

This thesis uses computational fluid dynamics to validate tomographic reconstruction algorithms. The computational fluid dynamics model was validated using experimental data from Sanyal et al.[2] Furthermore, this thesis finds ways of improving tomographic reconstructions through discovering which reconstruction algorithms perform best for different datasets. It was found that for time-resolved bubble fields, a version of SIRT (Simultaneous Iterative Reconstruction Technique) with generalised Tikhonov regularisation using the derivative operator performed best with a NRMSE (Normalised Root Mean Squared Error) of 0.0867 over a baseline value of 0.1123 using the default SIRT method and an F-score of 0.641 for the binary classification of air and water. For time-averaged reconstructions of the gas holdup, an SIRT with standard Tikhonov regularisation with an offset to the mean gas holdup was found to perform best with a NRSME of 0.0137 over a SIRT baseline of 0.0160. Finally, this thesis shows the improvement to tomographic reconstructions for an upgraded version of the TU Delft X-ray tomography setup and provides recommendations for future research on this topic. It was shown that increasing the number of source-detector pairs to five, leads to significant improvements in the time-resolved bubble field reconstructions, with a new NRMSE of 0.0617 (-28%) and F-score of 0.823 (+28%).

Contents

Nomenclature

Abbreviations

Abbreviation	Definition
CARPT	Computer Automated Radioactive Particle Tracking
CFD	Computational Fluid Dynamics
CT	Computed Tomography
DSD	Daughter Size Distribution
DPM	Discrete Particle Model
LBM	Lattice-Boltzmann Method
MRT	Multiple Relaxation Time
(N)RMSE	(Normalised) Root Mean Squared Error
PCM	Particle Centroid Method
PPV	Positive Predictive Value
SIRT	Simultaneous Iterative Reconstruction Technique
STRs	Stirred-Tank Reactors
SVD	Singular Value Decomposition
TPR	True Positive Rate

Symbols

Symbol	Definition	Unit
$\boldsymbol{A}$	System matrix	[-]
$A_{\perp}$	Frontal area	[m^2]
B	Convex set B (box constraints)	[-]
c_f	Speed of sound in fluid	[$m\,s^{-1}$]
$\boldsymbol{C}$	Diagonal inverse column-sum matrix	[-]
C_D	Coefficient of drag	[-]
C_L	Coefficient of lift	[-]
d	Diameter	[m]
d_H	Hydraulic diameter	[m]
d_i	Parent bubble diameter	[m]
d_j	Daughter bubble diameter	[m]
$d_{p,FPC}$	Fluid-to-Particle conversion diameter	[mm]
$d_{p,PFC}$	Fluid-to-Particle conversion diameter	[mm]
$\vec{f}_b$	Body forces	[$N\,m^{-3}$]
$\vec{f}_s$	Surface forces	[$N\,m^{-3}$]
$\vec{f}_\sigma$	Surface tension force	[$N\,m^{-3}$]
f_V	Daughter bubble fraction	[-]
$\vec{F}_D$	Drag force vector	[N]
$\vec{F}_{GB}$	Net gravity-buoyancy force vector	[N]

Symbol	Definition	Unit
$\vec{F}_L$	Lift force vector	[N]
$\vec{F}_M$	Virtual mass force vector	[N]
$\vec{F}_P$	Horizontal pressure gradient force vector	[N]
g	Gravitational acceleration	[m s^{-2}]
$\boldsymbol{I}$	Identity matrix	[-]
N, M	Number of rows and columns in matrix $\boldsymbol{A}$	[-]
N_s	Number of samples	[-]
N_{bins}	Number of bins	[-]
NL	Noise level	[-]
m_p	Particle mass	[kg]
p	Pressure	[Pa]
P_c	Coalescence probability	[-]
$\boldsymbol{R}$	Diagonal inverse row-sum matrix	[-]
t	Time	[s]
Δt	Time step discretisation	[s]
$\vec{u}$	Velocity vector	[m s^{-1}]
$\overline{u}$	Mean velocity component	[m s^{-1}]
$\vec{u}'$	Fluctuating velocity component	[m s^{-1}]
u_{max}	Maximum reference velocity	[m s^{-1}]
u_s	Superficial velocity	[m s^{-1}]
$\vec{x}$	Coordinate vector	[m]
Δx	Length interval discretisation	[m]
α	Regularisation parameter	[-]
β	Regularisation offset	[kg m^{-3}]
κ	Local interface curvature	[m^{-1}]
ν	Kinematic viscosity	[m^2 s^{-1}]
ρ	Density	[kg m^{-3}]
σ	Surface tension	[N m^{-1}]
$\sigma_\square$	Singular value	[-]
ϕ	Phase indicator	[-]
φ	Volume fraction	[-]
$\vec{\omega}$	Vorticity vector ($\nabla \times \vec{u}$)	[s^{-1}]

Mathematical operators and symbols

Symbol	Definition
$\arg\min_{\boldsymbol{x}}$	Argument $\boldsymbol{x}$ of the minimum
$\dot{\vec{u}}$	First-order time derivative of $\vec{u}$
$\mathrm{Cond}(\boldsymbol{A})$	Condition number of matrix $\boldsymbol{A}$
$\mathrm{erf}()$	Error function
∇	Nabla operator (gradient)
$\nabla\cdot$	Divergence operator
$\nabla\times$	Rotation / rotor operator
∇^2	Laplacian operator
$\max$	Maximum
$\min$	Minimum

Symbol	Definition
$\overline{\square}$	Time-averaged mean / Population mean
P_B	Projection onto convex set B
$\times$	Cross product
$\|\cdot\|$	Vector / Matrix norm
$\|\cdot\|_2$	Eulerian norm (vector) / Spectral norm (matrix)
$\|\cdot\|_{\boldsymbol{A}}$	Norm weighted by matrix $\boldsymbol{A}$
$\mathbf{0}$	Zero vectors
$\mathbf{1}$	All-ones vectors

Indices

Subscript	Definition
i, j	Indeces
x, y, z	Cartesian dimensions, y referring to vertical height
max	Maximum value
min	Minimum value
f	Fluid phases (liquid: $f, 1$, gas: $f, 2$)
p	Particle phase (Euler-Lagrange model)
s	Sample

Dimensionless numbers

Symbol	Definition	Equation
Co	Courant number	$\frac{u_{max}\Delta t}{\Delta x}$
Eo	Eötvös number	$\frac{gd_p^2(\rho_f - \rho_p)}{\sigma}$
Ma	Mach number	$\frac{\lvert u_f\rvert}{c_f}$
Mo	Morton number	$\frac{g\rho_f^2\nu_f^4(\rho_f - \rho_p)}{\sigma^3}$
Re_f	Reynolds number	$\frac{d_H\lvert\vec{u}_f\rvert}{\nu_f}$
Re_p	Particle Reynolds number	$\frac{d_p\lvert\vec{u}_{f,p}\rvert}{\nu_f}$

1 Introduction

1.1. Bubble columns and fermentation

With the world increasingly transitioning away from fossil fuels, the chemical industry has been exploring alternative feedstocks and processes in chemical manufacturing. This has led to an increased research interest in industrial-scale bioprocesses as a way to utilise biogenic feedstocks [3, 4]. Bubble columns reactors are well suited to such industrial-scale bioprocesses, such as syngas fermentation [5]. Often being just a vertical cylindrical tank with a sparger plate at the bottom, optional internal structures to change the flow characteristics and no moving parts, these reactors are inexpensive to build and maintain [6, 7]. Additionally, bubble columns are easy to operate since the gas sparging rate the only operational variable in regards to interphase mass transfer and mixing. This is also the main disadvantage of bubble columns. Mixing and interphase mass transfer are both dependent on the gas sparging rate and thus unable to be changed independently. Therefore, the required mixing and interphase mass transfer rates at scale need to be taken into account during the reactor design phase.

This is easier said than done however. There are many design correlations [8, 9] and Computational Fluid Dynamics (CFD) models [10, 11] available in literature. Yet, these models tend to have significant errors compared to experimental data on the order of 15% and above [11]. Furthermore, most models are based on air-water systems, which excludes the effects of other broth components. These additional broth components can have industrially significant effects on interphase mass transfer via inhibiting bubble coalescence [1, 12]. The current theory underlying this coalescence inhibition by solutes such as salts and fermentation products is the Gibbs-Marangoni pressure [13, 14]. Though other effects are also thought to play a role [15]. Improved models incorporating the effects of broth components such as Gibbs-Marangoni pressure on bubble dynamics and flow behaviour would be a valuable contribution to existing literature.

1.2. Experimental measurement and Computed Tomography

However, a solid foundation of experimental data is essential to develop and validate such improved models. However, gathering data on the flow in bubble columns is difficult. Although image-based methods work at low gas holdups, they are not useful at high gas holdups or when using opaque liquids such as fermentation broths with high biomass concentrations [16, 17]. Semi-local measurement of the gas holdup can be achieved via measurement of the pressure drop across an axial section of the bubble column, although this does not provide information on individual bubbles [18]. Recent developments in optical fibre probes now allow

for the measurement of phase information over time at individual points in bubble columns. Using Doppler measurement of the velocity of the interface, the length of the bubble chord and the velocity of the bubble can be measured to create bubble size and velocity distributions [19]. However, these fibre probes do influence the local fluid flow to some extent and can only measure interfaces in a specific direction at one location at the time. Non-invasive measurement technique capable of determining the local holdup without influencing the fluid flow. X-ray computed tomography may be able to provide the best of both worlds.

Computed Tomography (CT) is the process of using a penetrating wave, ray or other signal to image multiple lower dimensional slices of a system and using a computer to reconstruct the higher dimensional system from these slices. X-ray CT is a particularly useful form of tomography in both medical and industrial fields. X-ray CT uses the fact that different materials attenuate X-rays according to the Beer-Lambert law, with the attenuation coefficient being roughly proportional to density [20]. In the context of bubble columns and other two-phase systems, CT has been applied to measure the time-averaged local holdup at various points in the reactor simultaneously [21, 22]. Furthermore, by using Computer Automated Radioactive Particle Tracking (CARPT) where the motion of radio-tagged particles is tracked over time, the local instantaneous velocities can be recorded. These can be used to reconstruct the local time-averaged velocity profile and turbulent kinetic energy, which in turn can be used for CFD model validation [2, 23, 24].

As stated above, these techniques are effective for gathering time-averaged data. However, time-resolved data are essential for studying bubble dynamics such as coalescence and break-up. Recently, Graas et al. have applied the three-angle high frame rate X-ray tomography setup at Delft University of Technology to reconstruct the time-resolved bubble field in a fluidised bed [25]. Work is now being performed to apply this same technique to produce time-resolved reconstructions of bubble columns using this setup. In order to be able to apply this new experimental measurement technique, it must be verified that the results produced by the method align with the ground truth. However, as stated previously, measuring the internal state of a bubble column is difficult and the measurement techniques have limitations.

Alternatively, rather than attempting to validate the time-resolved CT method using other experimental measurements, one could attempt to model both the time-resolved CT setup as well as the bubble column system in order to create a digital twin of the experiment. A CFD model of an (air-water) bubble column system provides a ground truth to compare with the CT reconstruction. Assuming that the CFD model can approximate the bubble field inside a real bubble column to a reasonable degree of accuracy, the errors present in the experimental reconstructions can be estimated via comparison to this digital twin. In addition, the effects of modifications and upgrades to the X-ray setup on CT reconstructions may be modelled a priori in order to determine which changes are most relevant to improving reconstructions.

1.3. Thesis statement

This master thesis seeks to develop and validate a CFD model capable of reproducing bubble fields in homogeneous bubbly and heterogeneous churn-turbulent bubble columns. Subsequently, this thesis seeks to quantify the accuracy and errors of limited-angle CT reconstructions of such a bubble field for both time-averaged and time-resolved data. Finally, this thesis will explore methods of improving the accuracy of these CT reconstructions and give recommendations for future experimental CT setups and reconstruction methods.

1.4. Project outline

In the next chapter, the theoretical background for the CFD model and the tomographic reconstruction algorithm is covered in detail. The limitations and assumptions underlying the models used are discussed and used to justify the final choices made in model design and numerical implementation. Next, the model implementation and numerical methods are explained including the fluid models, system geometries, boundary conditions, etc. for the CFD model. In addition, the X-ray system and projection geometries for CT are described.

In the following chapter, the results will be described as discussed. First, the CFD model is validated using data from a paper by Sanyal et al.[2] Using both time-resolved and time-averaged data from the CFD model, CT reconstructions are performed and compared using different reconstruction algorithms. The errors for these different methods will be quantified using both the continuous Normalised Root Mean Squared Error and discrete performance measures of binary classifiers. The effect of increasing the number of projection angles on time-resolved reconstructions is also explored to show a possible future upgrade path for the TU Delft X-ray setup. Finally, the assumption of axisymmetry during tomographic reconstruction and its effect on reconstruction error is examined.

2

Theoretical Background

2.1. Hydrodynamics

The behaviour of fluids at the continuum scale is described by the continuity equation (equation (2.1)) and Navier-Stokes equation (equation (2.2)). Where ρ is the density, $\vec{u}$ is the velocity, p is the pressure, ν is the kinematic viscosity, $\vec{f_b}$ are the body forces and $\vec{f_s}$ are the surface forces.

$$\frac{\partial \rho}{\partial t} + \nabla \cdot (\rho \vec{u}) = 0 \tag{2.1}$$

$$\rho \left(\frac{\partial \vec{u}}{\partial t} + \vec{u} \cdot \nabla \vec{u} \right) = -\nabla p + \rho \nu \nabla^2 \vec{u} + \vec{f_b} + \vec{f_s} \tag{2.2}$$

A common simplification is the assumption of incompressibility as seen in equations (2.3) and (2.4), where the density is assumed to be constant and thus the divergence of the velocity field is zero. This assumption holds for low Mach numbers [26, 27].

$$\nabla \cdot \vec{u} = 0 \tag{2.3}$$

$$\frac{\partial \vec{u}}{\partial t} + \vec{u} \cdot \nabla \vec{u} = -\frac{\nabla p}{\rho} + \nu \nabla^2 \vec{u} + \frac{1}{\rho} \vec{f_b} + \frac{1}{\rho} \vec{f_s} \tag{2.4}$$

Most conventional CFD software discretises the Navier-Stokes equation for small fluid domains resulting the Finite Volume method. The continuity and Navier-Stokes equations are then solved over these finite volumes. However, finding a satisfactory numerical solution requires significant computational resources to solve the non-linear Navier-Stokes equation which often requires several iterations per time-step for transient simulations. Therefore, alternative methods such as the Lattice Boltzmann method have become increasingly popular.

2.1.1. Lattice Boltzmann method

For a more complete exploration of the Lattice Boltzmann method and underlying maths and physics, please refer to *The Lattice Boltzmann Method: Principles and Practice* by T. Krüger et al. [28] which will be referenced throughout this section. As mentioned previously, the Navier-Stokes equation applies at the macroscopic scale where the fluid can be treated as a continuum. While at the microscopic scale fluids consist of discrete particles interacting via collisions. Both model descriptions accurately describe the same system at different scales.

The Boltzmann equation from statistical mechanics can be used to describe fluid systems at the intermediate mesoscopic scale; where the probability distribution of the particle positions and momentums are considered rather than keeping track of the position and momentum of individual particles [28, ch. 1.2]. Similarly to how the Navier-Stokes equation can be discretised across several finite volumes, the Boltzmann equation can be discretised across a uniform lattice of grid points resulting in the Lattice Boltzmann method:

$$f_i(\vec{x} + c_i\Delta t, t + \Delta t) = f_i(\vec{x}, t) + \Omega_i(\vec{x}, t) \tag{2.5}$$

In this equation, $f_i(x,t)$ describes the set of probability density distributions of the momentum and position of the fluid particles. Each component of the momentum distribution in $f_i(x,t)$ streams with velocity c_i to the respective lattice points at $\vec{x} + c_i\Delta t$ in what is known as the 'streaming step'. At their destination lattice points, the momentum distributions are relaxed according to the collision operator $\Omega_i(\vec{x}, t)$ in what is known as the 'collision step'. [28, ch. 3]. Despite statistically describing the movement of discrete particles, it has been shown via the Chapman-Enskog expansion that the Lattice Boltzmann method indirectly solves the Navier-Stokes equation [28, ch. 4][29]. Hence, macroscopic fluid variables are tied to the mesoscopic particle distribution via the moments describing the distribution of $f_i(x,t)$. LBM has seen increasing adoption over Finite Volume solvers as it allows for parallelised numerical solving schemes which take advantage of modern graphical processing unit (GPU) hardware. This is due to the streaming step being a large linear matrix operation and the collision step being non-linear but entirely local to the grid cell. Both these steps are very amenable to parallelisation on the GPU [28, ch. 2.4].

2.1.2. Immiscible two-fluid model

Bubble columns, being two-phase / two-component systems, require some form of tracking the two phases and method of resolving the interface boundary conditions between them. M-Star CFD provides the Immiscible Two-Fluid (ITF) model with the High Density Ratio (ITF-HDR) option for simulating resolved multiphase flows in gas-liquid systems. The ITF-HDR model implementation in M-Star CFD is based on a paper by Sitompul & Aoki [30]. The ITF model keeps track of the phases using the phase indicator function $\phi(\vec{x}, t)$ across the fluid domain. The fluid properties are set according to the local value of the phase indicator (equations (2.6) and (2.7)).

$$\rho_f = \rho_{f,1} + \phi(\rho_{f,2} - \rho_{f,1}) \tag{2.6}$$
$$\nu_f = \nu_{f,1} + \phi(\nu_{f,2} - \nu_{f,1}) \tag{2.7}$$

The evolution of the phase-field over time is modelled using a conservative form of the Allen-Cahn equation shown in equation (2.8), where M and W are the interface mobility and interface width parameters respectively and $\vec{n}$ represents the normal vector of the interface [31, 32]. M and W are tied to the lattice grid size and time-step and are set automatically. In real multiphase systems the interface width in the order of nanometres. One of the limitations of this phase-field method is that, being a diffuse interface model, the interface width must be resolved over several grid cells. Despite this limitation, diffuse interface models are capable of dealing with lattice spacing above the nanometre scale as long as relevant fluid length scales are larger than the interface width [28, pp. 339-340][32].

$$\frac{\partial \phi}{\partial t} + \nabla \cdot \phi \vec{u} = \nabla \left[M \left(\nabla \phi - \frac{1 - 4\left(\phi - \frac{1}{2}\right)^2}{W} \vec{n} \right) \right], \vec{n} = \frac{\nabla \phi}{|\nabla \phi|} \tag{2.8}$$

The surface tension force is implemented as a surface force term in the Navier-Stokes equation based on the continuum surface force model according to equation (2.9) [31, 33]. The surface tension force acts normal to the interface and is proportional to the local curvature of the interface κ.

$$\vec{f_\sigma} = \sigma \kappa \nabla \phi \tag{2.9}$$

$$\kappa = \nabla \cdot \vec{n} = \nabla \cdot \left(\frac{\nabla \phi}{|\nabla \phi|} \right) \tag{2.10}$$

2.1.3. Turbulence models

The conventional LBM turbulence model is Large Eddy Simulation (LES) with some sort of sub-grid closure model. In this model, turbulence is divided between the large eddies (a.k.a. filtered component) which are explicitly modelled and small eddies which are approximated using sub-grid closure model. M-Star CFD uses LES with the Smagorinsky sub-grid model for most fluid models [34]. The Smagorinsky sub-grid model assumes isotropic turbulence at sub-grid eddy sizes, which affects the fluid via an additional turbulent viscosity ν_t atop the molecular viscosity ν_f based on the magnitude of the filtered strain rate tensor $\bar{S}$. The local strain rate tensor can be derived directly from the second order moments or cumulants of the particle distribution function [35].

$$\nu = \nu_f + \nu_t \tag{2.11}$$

$$\nu_t = (C_s \Delta x)^2 \bar{S} \tag{2.12}$$

However, the ITF-HDR model does not use an explicit sub-grid turbulence model like the Smagorinsky model [35]. Rather it relies on modelling turbulence implicitly via Implicit Large Eddy Simulation (ILES). ILES is based on tuning the numerical diffusion of momentum in the solver to act as a form of turbulent viscosity approximating a sub-grid closure model. Furthermore, the ITF-HDR model has an optional velocity filter to improve numerical stability at high Reynolds number, which also acts as an additional source of viscosity [30]. It should be noted that these sources of numerical viscosity are determined heuristically and do not have a physical justification as opposed to the Smagorinsky sub-grid model; although the Smagorinsky model is also not without its detractors [36]. Besides, the relaxation rates and velocity filter are coupled to the grid sizing and time step, which may lead to additional grid and time step dependence. Therefore, the turbulence model should be validated against other models and/or experimental data to validate that accurate turbulent energy dissipation is achieved.

2.2. Lagrangian bubble dynamics

An alternative to capturing resolved bubbles using the immiscible two-fluid model is the Euler-Lagrange approach of modelling bubbles. Specifically, M-Star CFD implements the conventional Discrete Particle Model (DPM) using the Particle Centroid Method (PCM) of fluid coupling [34]. In this model gas bubbles are treated as Lagrangian point masses moving through a continuous Eulerian liquid phase. The movement of gas bubbles is determined by numerically integrating the momentum balance over time (equation (2.13)). The fluid forces affecting

the gas bubbles can be either be one-way coupled, thus only affecting the particle, or two-way coupled using Newton's third law as described in equation (2.14), affecting both the particle and the fluid. Since gravity is an external force affecting both fluid and particles separately, it is not included in the two-way coupling.

$$\vec{F}_{p,i} = m_{p,i}\frac{d\vec{u_{p,i}}}{dt} = \vec{F}_{GB,i} + \vec{F}_{M,i} + \vec{F}_{P,i} + \vec{F}_{D,i} + \vec{F}_{L,i} \tag{2.13}$$

$$\vec{F}_f = -\sum_{i\in\vec{x}} \left(\vec{F}_{M,i} + \vec{F}_{P,i} + \vec{F}_{D,i} + \vec{F}_{L,i}\right) \tag{2.14}$$

The advantages of this method include lower resolution requirements for fluid simulation since the interface does not have to be grid-resolved. Therefore, bubbles smaller than the grid size can be captured accurately. Additionally, forces can be excluded if they do not significantly affect the dynamics of the system which can speed up computation.

The disadvantages of this method are the fact that the forces affecting the particles have to be defined explicitly, often according to empirical correlations. One has to verify that the chosen empirical model is applicable for the given conditions as a model developed for e.g. laminar conditions may not be valid when extrapolated to turbulent conditions. Similar verification is required for bubble break-up and coalescence models as explored in section 2.2.2.

Furthermore, as explained in detail by Ling et al. [37], the assumptions underlying the particle force models such as the drag, lift and pressure gradient forces may not be valid when using a PCM-based particle implementation. PCM-based particle models only expose the fluid parameters for the grid cell containing the particle centroid. Generally, for the assumptions of particle force models to be fully valid, the local fluid velocity unperturbed by the particle are required since these forces act close to the interface. The local fluid velocity does approximate this unperturbed state in cases where particle diameter is an order magnitude smaller than the grid cell ($d_p << \Delta x$) However, in cases where the particle diameter approaches the grid cell size ($d_p \sim \Delta x$), the two-way coupling will cause the fluid velocity to become perturbed by the particle. This effect will be further exacerbated when the particle diameter exceeds the grid cell size ($d_p > \Delta x$) as the particle forces will be applied to only a single grid cell containing the particle centroid despite the actual particle and associated force coupling being distributed over several grid cells. On top of this, the model describing the lattice Boltzmann fluid in which the Lagrangian particles move is based on the assumption that the volume fraction of particles is also low.

Ling et al. [37] propose two solutions to this issue: either only performing one-way fluid-to-particle coupling for low Lagrangian particle mass fractions in resolved simulations with fluid-particle conversion, or using a custom Gaussian kernel for applying two-way coupling between a particle and multiple fluid cells. In either case, the local fluid velocity is decomposed into local unperturbed fluid velocity and a particle contribution, which can then be acted on independently. Only the first method is implemented in M-Star CFD via one-way fluid-to-particle coupling.

2.2.1. Forces

The following section explores the models which may be used for each of the force terms. One notable exclusion from the momentum balance in most Euler-Lagrange models is the Basset force due to difficulty of implementation and high-computational requirements. The Basset history force represents the viscous effects in the boundary layer near the particle interface which delay the response to acceleration of the particle relative to the surrounding fluid [38] [39, pp. 19-20]. Despite its exclusion from the momentum balance in equation (2.13), research

by Muniz & Sommerveld appears to show that Basset force is the most important interfacial force in bubble columns after drag and added mass over short timescales [40].

Gravity & Buoyancy forces

The gravity and buoyancy force can be combined into one net force by taking the weight of the bubble and subtracting the weight of the displaced fluid as described by equation (2.15).

$$\vec{F}_{GB} = \frac{m_p g(\rho_p - \rho_f)}{\rho_p} \tag{2.15}$$

Pressure gradient force

The pressure gradient force is effectively equivalent to the buoyancy force, arising from the hydrostatic pressure gradient, and the pressure swings arising from fluid acceleration [39]. M-Star's implementation of the pressure gradient force is somewhat opaque as the buoyancy force is computed separately as shown above, though equation (2.16) is provided in the documentation.

$$\vec{F}_P = -V_p \nabla p \tag{2.16}$$

Virtual mass effect

As derived by Odar et al. [41, 42], the virtual mass (also called added mass) force results from inertia of the displaced fluid surrounding the particle. When the particle accelerates relative to the surrounding fluid, the fluid near the interface of the particle must also be accelerated in accordance with the interface boundary condition. This manifests as a force opposing the acceleration relative to the fluid due to the inertia of the fluid near the interface. The virtual mass force is particularly relevant when modelling gas bubble in liquid as the inertia of the low-density gas bubble is far exceeded by the inertia of the surrounding fluid.

$$\vec{F}_M = \left(2.1 - \frac{0.132}{0.12 + A_c^2}\right) V_p \rho_f \frac{\dot{\vec{u}}_f - \dot{\vec{u}}_p}{2} \tag{2.17}$$

$$A_c = \frac{|\vec{u}_f - \vec{u}_p|^2}{d_p |\dot{\vec{u}}_f - \dot{\vec{u}}_p|} \tag{2.18}$$

Drag force

The drag force as described by equation (2.19) results from the difference in velocity between the bubble and the surrounding fluid. The default drag force model for all Lagrangian particles used in M-Star CFD is the Brown and Lawler drag force coefficient [43] as described by equation (2.20).

$$\vec{F}_D = C_D A_\perp \frac{1}{2} \rho_f |\vec{u}_{f,p}| \vec{u}_{f,p} = \frac{\pi}{8} C_D d_p^2 \rho_f |\vec{u}_f - \vec{u}_p| (\vec{u}_f - \vec{u}_p) \tag{2.19}$$

$$C_D = \frac{24}{Re_p}(1 + 0.15 Re_p^{0.681}) + \frac{0.407}{1 + \frac{8710}{Re_p}} \tag{2.20}$$

However, using the Brown and Lawler model for bubble dynamics assumes perfectly spherical bubbles. To account for deformed bubbles, an alternative model is required. The drag correlations by Tomiyama account for deformed bubbles under a wide range of conditions

($10^{-2} < Eo < 10^3, 10^{-3} < Re_p < 10^5$) in air-water systems [44]. Furthermore, Tomiyama developed separate drag correlation based on different levels of water contamination. The correlation for the drag coefficient in fully contaminated systems as described by equation (2.21) is most applicable to the system being simulated.

$$C_D = \max\left[\frac{24}{Re_p}(1 + 0.15Re_p^{0.687}), \frac{8}{3}\frac{Eo}{Eo+4}\right] \tag{2.21}$$

If a fully Lagrangian bubble representation is chosen, an addition of a correction factor may be necessary at higher gas holdups to account for bubble-bubble interactions in swarms. When the larger bubble structures are resolved, effects such as the wake entrainment may be captured implicitly [11, 45, 46]. Additional research is required to determine the necessity of drag corrections in such hybrid models.

Lift force

The lift force, also called the Saffman force, is a transverse force which arises in shear flows as a result of particle rotation. The default lift force model used by M-Star CFD is based on Saffman's derivation as described in equation (2.22).

$$\vec{F}_L = 1.61 d_p^2 \rho_f \sqrt{\frac{\nu_f}{|\vec{\omega}_f|}} \left[(\vec{u}_f - \vec{u}_p) \times \vec{\omega}_f\right] \tag{2.22}$$

However, like the default drag model, this model applies for rigid spherical particles. Tomiyama derived lift correlations for bubbles using a modified Eötvös number (Eo_d) as calculated using equation (2.24), where the diameter used is the length of the bubbles major axis [47]. The bubble major axis size can calculated using the empirical correlation based on the unmodified Eötvös number in contaminated systems (equation (2.25)) [48].

$$\vec{F}_L = C_L \rho_f V_p (\vec{u}_f - \vec{u}_p) \times \vec{\omega}_f \tag{2.23}$$

$$C_L = \begin{cases} \min\left[0.288 \tanh\left(0.121 Re_p\right), f(Eo_d)\right] & Eo_d \leq 4 \\ f(Eo_d) & 4 < Eo_d \leq 10 \\ -0.27 & 10 < Eo_d \end{cases} \tag{2.24}$$

$$f(Eo_d) = 0.00105 Eo_d^3 - 0.0159 Eo_d^2 - 0.0204 Eo_d + 0.474$$

$$d_H = d_p \sqrt[3]{1 + Eo^{0.757}} \tag{2.25}$$

However, it should be noted that the Tomiyama lift correlations where developed significantly higher Morton numbers ($-5.5 < log\ Mo < -2.8$) than occur in air-water systems ($log\ Mo \approx -11$) and are only strictly valid for a limited range of Eötvös numbers ($1.38 < Eo < 5.74$). Despite these limitations, the correlations have seen broad application in CFD modelling outside of these original conditions.

2.2.2. Bubble breakup & coalescence

There are several proposed physical mechanisms and empirical models for fluid particle breakup and coalescence. These models have been reviewed extensively by Liao and Lucas [49, 50]. They conclude that for both phenomena, mechanistic models are preferable over empirical models. According to the 2009 review, the turbulent eddy collision breakup model is by far the most popular model with the most available literature. Coalescence models on the whole are more varied in their approaches. In terms of applicability to fermentation bubble column, the film drainage model has the advantage of including parameters for modelling the effect of electrolytes on bubble coalescence [13, 51, 52].

Breakup

The breakup criteria of a gas bubble can be defined using the dimensionless Weber number, which describes the ratio between the inertial forces on the bubble and the surface tension (equation (2.26)) [53]. Break-up occurs when a critical Weber number is reached and the disruptive inertial forces exceed the restorative force of surface tension [17, 54].

$$We = \frac{\rho_f |\vec{u}|^2 d_H}{\sigma} \tag{2.26}$$

In the turbulent eddy collision breakup model, the $|\vec{u}|^2$ can be substituted by the mean turbulent velocity $\overline{u'}$ using the relation $\overline{(u')^2} = C(\varepsilon d)^{\frac{2}{3}}$ where the constant C has experimentally been determined to be 2.0 [54–56]. Since the Weber number is dimensionless, this constant is often subsumed into the Weber number, leading to the definition of the Weber number described in equation (2.27)

$$We = \frac{\rho_f \varepsilon^{\frac{2}{3}} d^{\frac{5}{3}}}{\sigma} \tag{2.27}$$

Experiments performed by Mast and Takors [17] have derived a critical Weber number for a bubble column by fitting CFD data to experimentally determined bubble size distributions. They arrive at a value of $We_c = 6.1$ using a minimum time between consecutive breakup events of 30 ms. However, the system studied in the Mast and Takors system is a homogenous system with little to no bubble-bubble interactions, which is required in order to use optical methods. Prince and Blanch [52] derive a value of $We_c = 4.5$ for turbulent gas-liquid flows based on the maximum stable bubble size expression provided by Bhavaraju et al [57].

After breakup the sizes of resulting daughter bubbles are not uniform. The bubble sizes resulting from breakup can be modelled by randomly sampling a daughter bubble distribution (DSD), which provides the probability density function for a given daughter bubble size (d_j) given a parent bubble size (d_i). Liao and Lucas [49] reviewed several DSD models and concluded that: ”The M-shape daughter bubble distribution is most reasonable.” Mast and Takors [17, 58] also apply an M-shaped DSD based on the work by Lehr et al. [59] as described in equation (2.28) in their models, though their implementation of this model appears flawed as discussed in appendix A. This results in overestimation of symmetrical bubble break-up, which in turn may have affected the We_c estimate since it is determined by the fitting of the bubble size distributions to experimental data.

$$DSD(d_j, d_i) = \frac{1}{\sqrt{\pi} f_V} \frac{\exp\left\{-\frac{9}{4}\left[ln\left(2^{\frac{2}{5}} \frac{d_j \rho^{\frac{3}{5}} \varepsilon^{\frac{2}{5}}}{\sigma^{\frac{3}{5}}}\right)\right]^2\right\}}{1 + \text{erf}\left\{\frac{3}{2}\left[ln\left(2^{\frac{1}{15}} \frac{d_i \rho^{\frac{3}{5}} \varepsilon^{\frac{2}{5}}}{\sigma^{\frac{3}{5}}}\right)\right]\right\}}, \; f_V = \frac{d_j^3}{d_i^3} \tag{2.28}$$

Coalescence

The default coalescence model in M-Star CFD is the criticial Reynolds number model based on a paper by Boshenyatov [60, 61]. M-Star specifically applies the correlation for turbulent bubble systems with low Weber numbers ($Re > 100, We < 1$). In this model, pair-wise collision are either a coalescence event where ($P_c = 1$) or a bounce ($P_c = 0$) based on the bubble pair Reynolds number Re_c (equations (2.29) to (2.32)). Where $U_{i,j}$ is relative bubble velocity and $d_{i,j}$ is the harmonic mean of the bubble diameters. Additionally, the M-Star CFD coalescence model limits the maximum bubble size at which coalescence takes place to 10 mm.

$$P_c = \begin{cases} 0 & Re_c < 40 \\ 1 & Re_c \geq 40 \end{cases} \tag{2.29}$$

$$Re_c = \frac{U_{i,j} d_{i,j}}{\nu_f} \tag{2.30}$$

$$U_{i,j} = \left| \frac{(\vec{u}_i - \vec{u}_j) \cdot (\vec{x}_i - \vec{x}_j)}{|\vec{x}_i - \vec{x}_j|} \right| \tag{2.31}$$

$$d_{i,j} = \frac{2 d_i d_j}{d_i + d_j} \tag{2.32}$$

A search of English language scientific literature does not yield independent validation of this model, except indirectly through M-Star mass transfer predictions in turbulent STRs [62–67]. Furthermore, the maximum coalescent bubble size parameter was shown to have a significant effect on the bubble size distribution, despite this limit having no apparent physical basis. This coalescence limiting may lead to non-physical accumulation of bubbles with sizes close to the maximum coalescent bubble size [65]. This hints at a possible overprediction of coalescence when using the critical Reynolds model when such an upper coalescence limit is not applied. Conversely, the complete exclusion of a coalescence model in turbulent STRs leads to a +50% overprediction of mass-transfer, which can be explained by the higher relative interfacial area of smaller bubbles [62].

An alternative to the critical Reynolds model is the film drainage model as it has been well-studied in literature [50]. It has previously been adapted to Euler-Lagrange simulations in work by Sommerfeld [68]. The film drainage model is based on the comparison of time scales of coalescence and contact between two bubbles. Bubbles coalesce if the contact time scale is longer than the coalescence time and vice versa. The coalescence time has several regimes depending on the bubble rigidity and contact interface mobility, which in turn depend on bubble size and the presence of surfactants [50, 69]. Considering the applicability to tap water as opposed to pure water and considering future applications using fermentation broth, the models pertaining to immobile and partially mobile interfaces are the most relevant to this research. Lee et al. [70] developed a model for partially mobile interface using a surface immobility parameter which has to determined empirically. Alternatively, there is the Oolman and Blanch model [51] using surface tension gradient / Gibbs-Marangoni pressure which can be determined experimentally or modelled [14, 71].

2.3. Computed tomography

In X-ray tomography, an object of interest is placed in the beam path of an X-ray source and detector. The object absorbs and scatters a fraction of X-rays emitted from the source in a process called attenuation. The detectors measure the intensity of the surviving fraction of X-rays after traversing the object. The detector measures the intensity in terms of detector counts, which is proportional to the number of photons hitting a detector pixel. The surviving fraction of X-rays a.k.a. the attenuation can then be determined by comparing the detector counts with and without the object in the beam path [20]. Modern detectors can output high-resolutions images with each pixel corresponding to a separate beam path which allows for rapid parallel data gathering.

The attenuation of a monochromatic X-ray beam $\frac{I}{I_0}$ along beam path l is described by Beer-Lambert's law along the beam path (equation (2.33)). The intensity of the attenuated X-ray beam I is equal to the initial intensity I_0 multiplied by the attenuation coefficient μ integrated along the beam path, where η describes the position along the beam. Tomography is the inverse problem of reconstructing the value of the attenuation coefficient μ at each point of the object given the attenuation along numerous beam paths [20, 72].

$$\frac{I}{I_0} = exp\left(-\int_l \mu(\eta)d\eta\right) \Leftrightarrow I = I_0 exp\left(-\int_l \mu(\eta)d\eta\right) \tag{2.33}$$

2.3.1. Mathematics behind tomography

In the following section, the mathematics behind computed tomography will be explained to level of detail judged to be relevant to the current research questions. Therefore, detailed mathematical proofs will be foregone in favour of a more concise explanation of the topics. For a detailed exploration of the derivations in this section, please refer to chapter 6 in *Computed Tomography: From Photon Statistics to Modern Cone-Beam CT* by T.M. Buzug [20] and the entirety of *Computed Tomography: Algorithms, Insight, and Just Enough Theory* by P.C. Hansen et al. [72] which will both be referenced throughout this section.

Equation 2.33 can be linearised by taking the logarithm of the attenuation (equation (2.34)). The attenuation coefficient integral can subsequently be discretised according to equation (2.35), where the product of the local attenuation coefficient μ_i and the path length along that local section of the beam path $\Delta\eta$ is summed along the entire beam. The discretised forward projection of the object to an X-ray image can then be represented as a linear system (equation (2.36)).

$$ln\left(\frac{I}{I_0}\right) = -\int_l \mu(\eta)d\eta \tag{2.34}$$

$$ln\left(\frac{I_0}{I}\right) = \sum_{i \in l} \mu_i \Delta\eta \tag{2.35}$$

$$\boldsymbol{b} = \boldsymbol{A}\boldsymbol{x} \tag{2.36}$$

In this system, the object vector $\boldsymbol{x}$ contains the local attenuation coefficients u_i for the object. The image vector $\boldsymbol{b}$ contains the total linearised attenuation $ln\left(\frac{I_0}{I}\right)$ along the various beam paths. The system matrix $\boldsymbol{A}$ represents the projection the object space to the image space; it is a real-valued positive matrix which maps the contribution of the local attenuation coefficient of each entry in the object vector $\boldsymbol{x}$ along the respective beam paths to the total linearised attenuation in $\boldsymbol{b}$ (equation (2.38)) [20, pp. 203–205] [73]. In other terms, the linear operation

$\boldsymbol{Ax}$ represent forwards projection with the adjoint $\boldsymbol{A}^T\boldsymbol{b}$ representing simple backprojection [72, pp. 167–171].

$$\boldsymbol{x} = \begin{pmatrix} \mu_i \\ \mu_{i+1} \\ \vdots \\ \mu_N \end{pmatrix}, \quad \boldsymbol{A} = \begin{pmatrix} a_{i,j} & a_{i+1,j} & \cdots & a_{N,j} \\ a_{i,j+1} & a_{i+1,j+1} & \cdots & a_{N,j+1} \\ \vdots & \vdots & \ddots & \vdots \\ a_{i,M} & a_{i+1,M} & \cdots & a_{N,M} \end{pmatrix}, \quad \boldsymbol{b} = \begin{pmatrix} ln\frac{I_{0,j}}{I_j} \\ ln\frac{I_{0,j+1}}{I_{j+1}} \\ \vdots \\ ln\frac{I_{0,M}}{I_M} \end{pmatrix} \tag{2.37}$$

$$\boldsymbol{A} \in \mathbb{R}_+^{N\times M},\ \boldsymbol{x} \in \mathbb{R}_+^N,\ \boldsymbol{b} \in \mathbb{R}_+^M \tag{2.38}$$

In an ideal case, the problem in equation (2.36) is well posed and one can just take the matrix inverse of $\boldsymbol{A}$ to calculate $\boldsymbol{x}$. In practice, the CT inverse problem is effectively always ill-posed. A problem is considered ill-posed when it does not meet all of the Hadamard criteria [74] shown below. The nonexistence of a solution is due to the presence of noise, which leads to an inconsistent linear problem. For example, if one imagines three affine planes intersecting at one point in space, any perturbation due to noise to any of the three planes would result in the point no longer intersecting all the planes. The non-uniqueness of the solution is due to the fact that tomography systems are almost always underdefined a.k.a. the matrix has fewer rows than columns. For example, if one imagines two affine plane intersecting, there is now a line of infinite length where they are equal to each other. The final criterium is difficult to explain. How this criterium and the others can be addressed using the least-squares method and regularisation is explained in detail in appendix B.

Hadamard's criteria

1. A solution exists; for the image vector, there exist a object vector which solves the problem.
2. The solution is unique; for the image vector, there exist only one associated object which solves the problem.
3. The solution is stable; for a large or small change in the image vector, there is a proportional change in the object vector.

2.3.2. Iterative reconstruction algorithms & Regularisation methods

As shown in the previous section and appendix B, solving the CT system directly via matrix inversion is unfeasible due to the ill-posed nature of the problem. Combined with the fact that the system matrix is often sufficiently large and sparse that its explicit storage is unfeasible, other solving methods are required. Iterative methods can address these issues by iteratively approaching a solution without needing to directly compute the matrix inverse. No storage of the explicit system matrix is required as these algorithms only rely on vector matrix multiplication. Additionally, iterative methods can provide a degree of implicit regularisation which limits the effect of noise at lower iterations [73, 75]. Furthermore, iterative methods can readily incorporate several explicit regularisation methods, such as generalised Tikhonov or total variation regularisation [20, 72, 76]. Finally, iterative reconstruction algorithms can apply box constraints to the reconstructed object vector by simply clipping the minimum and maximum values after each iteration, more formally known as projection onto a convex set [72, p. 221].

Simultaneous Iterative Reconstruction Technique

The Simultaneous Iterative Reconstruction Technique (SIRT) and associated algorithms known as SIRT-like methods were developed by Gilbert in 1972 [77]. These methods solve the geo-

metrically weighted least-squares problem according to the distance each ray travels through the object (equation (2.39)). The weighting is determined by taking the inverse of the row sums of system matrix $\boldsymbol{A}$. Rays that traverse through more of the object can therefore accept proportionally higher residuals and vice versa [73]. This prevents the algorithm from preferentially changing the voxels with a higher number of traversing rays. Additionally, box constraints can be applied via iterative projection P_B of the reconstruction onto a convex set B through clipping the data to the maximum and minimum allowed values (equation (2.40)). This provides superior reconstructions by constricting the solution space [72, fig. 11.14].

$$\arg\min_{\boldsymbol{x}} \frac{1}{2}\|\boldsymbol{A}\boldsymbol{x}-\boldsymbol{b}\|_{\boldsymbol{R}}^2 \tag{2.39}$$

$$\arg\min_{\boldsymbol{x}\in B} \frac{1}{2}\|\boldsymbol{A}\boldsymbol{x}-\boldsymbol{b}\|_{\boldsymbol{R}}^2 \tag{2.40}$$

To describe the iterative notation of SIRT, the two diagonal matrices $\boldsymbol{R}$ and $\boldsymbol{C}$ are required. These matrices contain the inverse of the row and column sums of $\boldsymbol{A}$ along their diagonals respectively. The $\boldsymbol{R}$ matrix is used to apply the previously described geometric weighting. The $\boldsymbol{C}$ matrix is used as a diagonal preconditioning matrix. The final iterative notation of the unconstrained and box constrained versions of SIRT is shown below (equations (2.44) and (2.45)).

$$\boldsymbol{R} = diag\left(\frac{1}{\sum_j a_{ij}}\right) \tag{2.41}$$

$$\boldsymbol{C} = diag\left(\frac{1}{\sum_i a_{ij}}\right) \tag{2.42}$$

$$\tag{2.43}$$

$$\boldsymbol{x}^{(k+1)} = \boldsymbol{x}^{(k)} + \lambda \boldsymbol{C}\boldsymbol{A}^T\boldsymbol{R}\left(\boldsymbol{b}-\boldsymbol{A}\boldsymbol{x}^{(k)}\right) \tag{2.44}$$

$$\boldsymbol{x}^{(k+1)} = P_B\left[\boldsymbol{x}^{(k)} + \lambda \boldsymbol{C}\boldsymbol{A}^T\boldsymbol{R}\left(\boldsymbol{b}-\boldsymbol{A}\boldsymbol{x}^{(k)}\right)\right] \tag{2.45}$$

The preconditioning matrix $\boldsymbol{C}$ is chosen as such because it guarantees convergence for any arbitrary initial object vector $\boldsymbol{x}_0$. SIRT is a form of Richardson Iteration which converges when the condition in equation (2.46) is met [78, pp. 181–187]. This convergence condition is based on the maximum eigenvalue σ_{max}^2 of $\boldsymbol{C}\boldsymbol{A}^T\boldsymbol{R}\boldsymbol{A}$. The maximum eigenvalue a.k.a. spectral radius of a non-negative matrix is bounded by its row sums. Since all entries in $\boldsymbol{A}$ are positive, $\boldsymbol{R}\boldsymbol{A}$ and $\boldsymbol{C}\boldsymbol{A}^T$ are non-negative and stochastic, where stochastic refers to all row sums being equal to unity. Therefore, for $0 < \lambda < 2$ SIRT will converge, though $\lambda = 1$ tends to be used by convention [73, 75].

$$0 < \lambda < \frac{2}{\sigma_{max}^2} \tag{2.46}$$

However, while SIRT attempts to converge to a least-squares solution, it does not necessarily converge to the minimum-norm least-squares solution $\boldsymbol{x}_{LS}$ in underdetermined systems. The minimum-norm least-squares solution refers to the solution with the smallest $\|\boldsymbol{x}\|$ which satisfies the least-square solution. The advantage of the minimum-norm least-squares solution is

that it has no components in the null space of the system matrix and hopefully all components of the solution can be attributed to the data [79, pp. 32-33]. The initial guess x_0 can affect the solution to which SIRT converges. However, when using a null vector as the initial guess, SIRT will converge to the minimum-norm least-squares solution [75].

Additionally, while SIRT addresses issues of ill-posedness via implicit regularisation, it does come with the problem of semiconvergence. Semiconvergence refers to the error compared to ground truth decreasing during initial iterations but this error increasing during later iterations by fitting to the noise rather than signal [80]. This is shown experimentally in appendix C.1. Therefore, when implementing SIRT for noisy data, a stopping rule is required to stop the algorithm when the solution ceases to improve compared to the ground truth. One such stopping rule for constrained problems is the Discrepancy Principle, where the algorithm is halted once the squared norm of the residual $\|\boldsymbol{b} - \boldsymbol{A}\boldsymbol{x}^{(k)}\|_2^2$ is lower than or equal to the squared norm of the error vector $\|\boldsymbol{e}\|_2^2$. For implementation of the Discrepancy Principle the noise is assumed to be Gaussian and its standard deviation must be quantified [72, pp. 234-235]. This assumption of Gaussian noise is not always appropriate for tomographic data, which tends to be mostly Poisson distributed since photon emission, scattering and detection are stochastic Poisson processes [20, ch. 2.6]. When the intensity (number of counts) is high enough, the central limit theorem can be applied to assume a Gaussian distribution [72, pp. 49–52]. An additional 'safety factor' η of e.g. 1.02 can be applied to stop the algorithm slightly early to account for inaccuracies in the estimate of the error vector, resulting in using $\eta\|\boldsymbol{e}\|_2^2$. Other stopping rules are covered by Hansen et al. in their 2021 paper [81]. Do note that in experimental setups there are additional sources of error which can affect noise such as dead pixels and beam hardening effects which must be taken into account as well.

Standard Tikhonov regularisation

Standard Tikhonov regularisation solves the issue of underdetermined systems by adding an a priori assumption of normality to the underlying object data. This assumption is applied by minimising $\boldsymbol{x}$ for $\|\boldsymbol{I}\boldsymbol{x}\|_2^2$ according to the regularisation weighting factor α which is proportional to the variance of the Gaussian prior [72, pp. 256–260]. This method of explicit regularisation does not suffer from semiconvergence, removing the need for a stopping rule. The Tikhonov regularised least-squares problem will converge to $\boldsymbol{x}_{Tik,LS}$. The performance of standard Tikhonov regularisation depends on whether the distribution of data in the object vector is close to normal. If the entries of the object vector are not normally distributed, as is the case in binary systems such as bubble columns, poor performance is to be expected.

$$\arg\min_{\boldsymbol{x}} \|\boldsymbol{A}\boldsymbol{x} - \boldsymbol{b}\|_2^2 + \alpha \|\boldsymbol{x}\|_2^2 \tag{2.47}$$

$$\arg\min_{\boldsymbol{x}} \left\| \begin{pmatrix} \boldsymbol{A} \\ \sqrt{\alpha}\boldsymbol{I} \end{pmatrix} \boldsymbol{x} - \begin{pmatrix} \boldsymbol{b} \\ \boldsymbol{0} \end{pmatrix} \right\|_2^2 \tag{2.48}$$

Applying standard Tikhonov regularisation to SIRT results in the following iterative notation. The projection onto a convex set can be applied in the same way as when using SIRT as shown below (equation (2.50)).

$$\boldsymbol{x}^{(k+1)} = \boldsymbol{x}^{(k)} + \lambda \boldsymbol{C}\boldsymbol{A}^T\boldsymbol{R}\left(\boldsymbol{b} - \boldsymbol{A}\boldsymbol{x}^{(k)}\right) - \alpha\lambda\boldsymbol{C}\boldsymbol{x}^{(k)} \tag{2.49}$$

$$\boldsymbol{x}^{(k+1)} = P_B\left[\boldsymbol{x}^{(k)} + \lambda \boldsymbol{C}\boldsymbol{A}^T\boldsymbol{R}\left(\boldsymbol{b} - \boldsymbol{A}\boldsymbol{x}^{(k)}\right) - \alpha\lambda\boldsymbol{C}\boldsymbol{x}^{(k)}\right] \tag{2.50}$$

Generalised Tikhonov regularisation

Standard Tikhonov regularisation may not be an appropriate technique when the entries in the object vector are not normally distributed. However, Tikhonov regularisation can be generalised to apply the normal prior distribution to the gradient of the data, which may be used to enforce the smoothness of a solution (equation (2.51)). Any appropriate linear operator can be used in place of ∇, however, in this case the gradient / derivative operator is used since reducing gradients leads to a smoother and less noisy solution [72, p. 261]. The gradient operator can be approximated using the central finite-difference in each dimension.

$$\underset{\boldsymbol{x}}{\arg\min} \left\| \boldsymbol{A}\boldsymbol{x} - \boldsymbol{b} \right\|_2^2 + \alpha \left\| \nabla \boldsymbol{x} \right\|_2^2 \tag{2.51}$$

Applying generalised Tikhonov regularisation to SIRT results in the following iterative notation (equations (2.52) and (2.53)). Notice that the gradient operator ends up as the Laplace operator in the iterative notation. Using the central finite-difference approximation of the gradient, a finite-difference approximation of the Laplacian can be constructed. The Laplacian of $\boldsymbol{x}$ is calculated each iteration to apply the Tikhonov regularisation. As an example, the heat equation should provide a degree of intuition on how this works; the Laplacian smooths out the object vector over increasing iterations in the same way that diffusion and conduction smooth out the concentration and temperature profiles over time. Projection onto a convex set works the same as before (equation (2.54)).

$$\boldsymbol{x}^{(k+1)} = \boldsymbol{x}^{(k)} + \lambda \boldsymbol{C}\boldsymbol{A}^T\boldsymbol{R}\left(\boldsymbol{b} - \boldsymbol{A}\boldsymbol{x}^{(k)}\right) - \alpha\lambda \boldsymbol{C}\nabla^T\nabla\boldsymbol{x}^{(k)} \tag{2.52}$$

$$\boldsymbol{x}^{(k+1)} = \boldsymbol{x}^{(k)} + \lambda \boldsymbol{C}\boldsymbol{A}^T\boldsymbol{R}\left(\boldsymbol{b} - \boldsymbol{A}\boldsymbol{x}^{(k)}\right) + \alpha\lambda \boldsymbol{C}\nabla^2\boldsymbol{x}^{(k)} \tag{2.53}$$

$$\boldsymbol{x}^{(k+1)} = P_B\left[\boldsymbol{x}^{(k)} + \lambda \boldsymbol{C}\boldsymbol{A}^T\boldsymbol{R}\left(\boldsymbol{b} - \boldsymbol{A}\boldsymbol{x}^{(k)}\right) + \alpha\lambda \boldsymbol{C}\nabla^2\boldsymbol{x}^{(k)}\right] \tag{2.54}$$

Total variation regularisation & the Chambolle-Pock algorithm

One downside of generalised Tikhonov regularisation of the gradient is that it always provides a smooth solution. While this assumption is reasonable for time-averaged data, time resolved data has regions of air and water with a discrete rather than a smooth boundary. This can be addressed by taking the 1-norm of object vector gradient rather than the 2-norm (equation (2.55)). The advantage of the 1-norm is that it penalises steep slopes in the object-vector less severely than 2-norm leading to a piece-wise smooth solution rather than an L^2 smoothed solution.

$$\underset{\boldsymbol{x}}{\arg\min} \left\| \boldsymbol{A}\boldsymbol{x} - \boldsymbol{b} \right\|_2^2 + \alpha \left\| \nabla \boldsymbol{x} \right\|_1 \tag{2.55}$$

However, solving the TV regularised problem cannot rely on traditional methods based on gradient decent as the gradient of the 1-norm is not smooth. Therefore, one can either use a smooth approximation of the 1-norm or an algorithm capable of convergence with non-smooth gradients such as the Chambolle-Pock (CP) algorithm.

The details of how the CP algorithm works are considered well beyond the scope of this thesis. Such details can be found in the original 2010 paper by Chambolle and Pock describing their method [82]. The implementation used in this work is based on the GitHub repository by Pierre Paleo showing the implementation of the CP algorithm in Python [83].

TV-regularisation is also possible in 4D (3 spatial and 1 temporal dimension) as shown in work by Boigné et al. This can reduce the effects of motion artifacts and may be interesting research direction to explore in future [84]. However, it is considered beyond the scope of this thesis due to the absence of motion blur in simulated data, difficulty of implementation and high computational resource requirements.

3

Model development & Methods

3.1. System description

The bubble column models are based on the dimensions of and conditions present in the experimental bubble column designed by Rik Volger at the TU Delft. First, a half-scale model capable of being run on a desktop GPU (NVIDIA GeForce RTX 4090 24GB) was developed for testing and model development. The full-scale model was developed based on this half-scale model to be run on the DelftBlue supercomputer GPU partition (NVIDIA Tesla A100 80GB) [85]. Two different gas debits set in different flow regimes (bubbly / turbulent) were simulated based on available experimental data of the Volger column. This results in four different cases as shown in table 3.1. Volumetric data is collected over the time range of 5 s to 15 s.

Table 3.1: Simulation case descriptions

#	Case name	Gas debit	u_s	Diameter	Fill height
1	Volger half-scale bubbly	8.1 L min^{-1}	1.7 cm s^{-1}	0.100 m	0.40 m
2	Volger half-scale turbulent	22 L min^{-1}	4.6 cm s^{-1}	0.100 m	0.40 m
3	Volger full-scale bubbly	30 L min^{-1}	1.7 cm s^{-1}	0.192 m	0.80 m
4	Volger full-scale turbulent	80 L min^{-1}	4.6 cm s^{-1}	0.192 m	0.80 m

3.1.1. Model geometries

Full-scale column

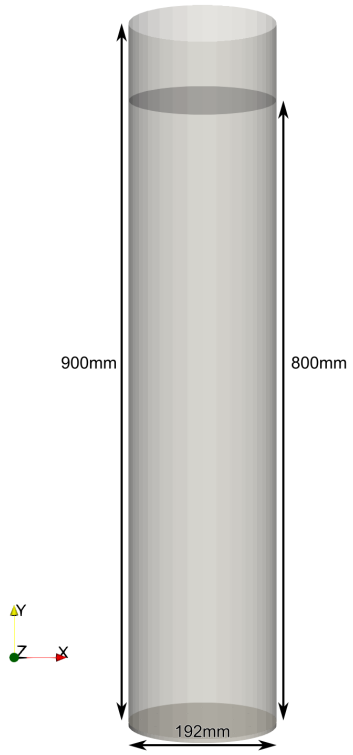

(a) Full-scale column geometry

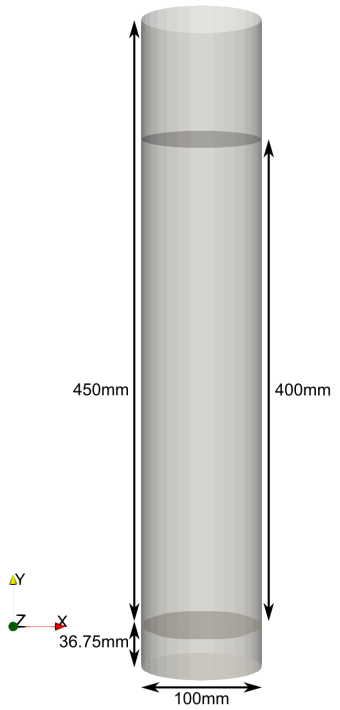

(b) Half-scale column geometry

Figure 3.1: Bubble column geometries: Note that axial measurements are taken from top of sparger plate.

Figure 3.1a shows the full-scale column model geometry which is based of the dimensions on the Volger bubble column (table 3.2). The simulated domain of the bubble column can be reduced compared to the experimental column. The experimental column is designed with coalescence inhibition compounds in mind which can significantly increase holdup [15]. Since this thesis only covers air-water systems, the simulated domain can be cropped safely down to only cover the top 0.90 m for a fill level of 0.80 m.

According to scale-up criteria proposed by Wilkinson et al. [86], the fill level is insufficient to generalise the gas holdup for larger scales. Wilkinson et al. state that a diameter to unexpanded fill level aspect ratio of at least 5 is required in order for the gas holdup to be scale independent, while this aspect ratio in the current geometry is only 4. The other two Wilkinson criteria are met, as the column diameter exceeds 15 cm and the sparger hole diameter exceeds 1 mm to 2 mm. While increasing the fill level to 1 m would resolve this limitation, this is would necessitate a reduction in grid resolution which would lead to more severe underresolution of the sparger plate geometry as explained in sections 3.3.1 and 3.4. Therefore, the fill level was kept at 0.80 m.

The perforated sparger plate has a triangular pitch of 40 mm with a hole diameter of 3 mm and a thickness of 5 mm. During experiments, seven of the 19 holes in the sparger plate were sealed to prevent excessive weeping. Therefore, the sparger plate model was adjusted to align with the experimental setup (figure 3.2a). This results in an overall sparger open area of 0.3%. The centre of the top of the sparger plate is defined as the system origin, with the Y-axis being the axial direction of the column and the X- and Z-axes being radial directions.

Table 3.2: Volger bubble column and sparger dimensions.

	Dimension
Full column height	1.70 m
Lower section column height	1.20 m
Simulated column height	0.90 m
Column internal diameter	0.192 m
Water fill height	0.80 m
Sparger hole diameter	3 mm
Sparger hole pitch	40 mm
Sparger open area	0.3%

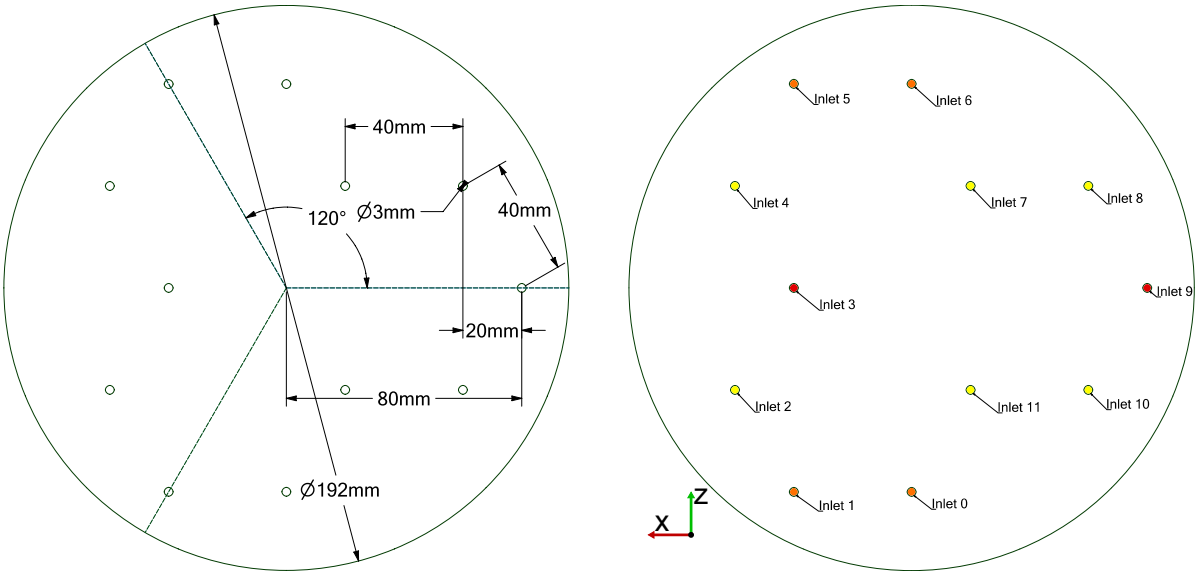

(a) Dimensions of the sparger plate.

(b) Labels of the inlet boundary conditions, coloured according to resolved area. Red: 48% orange: 56%, yellow: 64% (table 3.7).

Figure 3.2: The full-scale Volger column perforated sparger plate: dimensions and inlet labels.

Half-scale column

Figure 3.1b shows the half-scale column model geometry. The height and diameter are about half that of the full-scale column, resulting in column height of 0.45 m with a fill height of 0.40 m and a diameter of 0.10 m. The upper section of the sparger box was included to check whether pressure and velocity fluctuations occur within. Significant pressure and velocity fluctuations below the sparger plate may result in differences in the mass-flow between sparger holes, which would require the inclusion of a sparger box model in the full-scale simulation in order to capture these effects.

As with the full-scale geometry, the half-scale geometry does not conform to the Wilkinson scale-up criteria in relation to fill level / diameter aspect ratio [86]. Additionally, the column diameter criterion is also not met, being under 15 cm. Hence, slug flow may occur when simulating the half-scale geometry at high superficial gas velocities and the gas holdup distribution is not scale independent.

The half-scale sparger is based on the centre of the full-scale sparger plate. The sparger is not scaled in order to assure similar initial bubble sizes since this depends strongly on sparger geometry. Specifically, hole diameter and to a lesser extent the gas flow rate per hole affect the bubble size distribution in both experimental measurements and theoretical derivations [87, 88]. Only the centre 7 holes fall within the column domain. While four of these holes are sealed in the full-scale column, these holes are unsealed in the half-scale simulation in order to provide a more uniform sparging profile compared to only having 3 holes. The resulting sparger open area is 0.6%, twice the value of the full-scale column. Therefore, the gas flow rate per sparger hole is lower, which will in turn affect the bubble size distribution. In hindsight, sealing 3 holes along the outer ring may have resulted in more comparable spargers between the full- and half-scale columns. The resulting sparger is shown in figure 3.3.

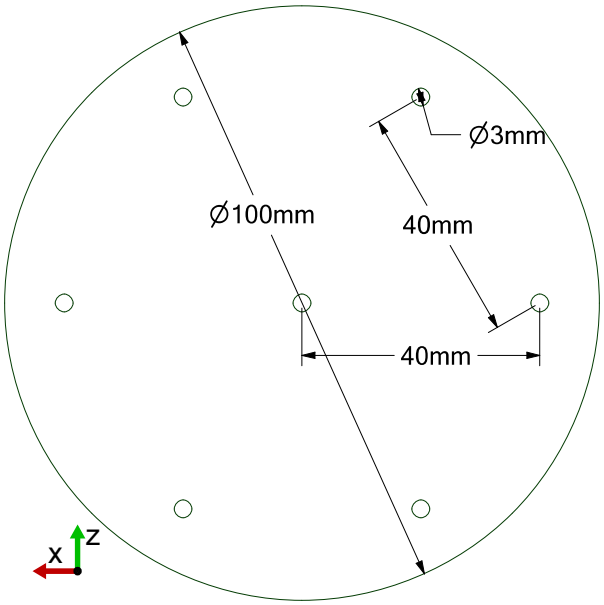

Figure 3.3: The half-scale column perforated sparger plate dimensions.

3.1.2. Physical parameters

The cylindrical column wall and sparger plate are made of polycarbonate and stainless steel respectively. Contact line forces at both the column wall and the sparger were enabled since absence of these forces appears to lead to bubble adherence to the wall and the sparger

orifices. This in turn leads to excessive jetting in the near-sparger region. The contact angles of these materials were estimated based on literature data (table 3.3). The physical parameters are based on air-water properties at ambient conditions for both the Euler-Lagrange model and Immiscible Two-Fluid model (table 3.4).

Table 3.3: Material contact angles used for contact line forces.

Material	Contact angle	Reference
Polycarbonate	82° (rounded to 80°)	[89]
Stainless steel	74.2° (rounded to 75°)	[90]

Table 3.4: Physical properties used in the ITF and EL models based on air-water at ambient conditions.

Property	Symbol	Value	Unit	Source
Density liquid	$\rho_{f,1}$	1000	[kg m^{-3}]	[53, p. 106]
Density gas	$\rho_{f,2}$, (ρ_p)	1.2	[kg m^{-3}]	[53, p. 114]
Kinematic viscosity liquid	$\nu_{f,1}$	1×10^{-6}	[m^2 s^{-1}]	[53, p. 119]
Kinematic viscosity gas	$\nu_{f,2}$	1.5×10^{-5}	[m^2 s^{-1}]	[53, p. 115]
Physical speed of sound gas	$c_{f,2}$	347	[m s^{-1}]	[53, p. 116]
Reference pressure	-	101325	[Pa]	[53, p. 15]
Surface tension	σ	0.072	[N m^{-1}]	[53, p. 119]

3.2. Solver information & Fluid models

All simulations were performed using M-Star CFD version 3.11.41 (stable) to solve the incompressible Navier-Stokes equations using the lattice Boltzmann method (see section 2.1.1). The two-phase flow is modelled using the ITF-HDR model (see section 2.1.2). Resolved air bubbles below a critical diameter are converted to Lagrangian particles via fluid-particle conversion and are modelled according to the Lagrangian bubble model described in section 3.5.

The ITF-HDR model fluid solver is based on the cumulant lattice Boltzmann method as developed by Geier et al. as opposed to the default Multiple Relaxation Time (MRT) model used in M-Star [35]. In cumulant-based methods, the probability distributions of the Boltzmann equation are described by their cumulants rather than their moments, which has several advantages as described in detail by Geier et al. such as improved Galilean invariance [91]. Rather the D3Q19 discretisation used for explicit LES by M-Star CFD, the cumulant-based method relies on D3Q27 discretisation. The details of the cumulant lattice Boltzmann method are considered beyond the scope of this thesis and can be found in the papers by Geier et al.[35, 91]

Water, being a liquid, is assumed to be incompressible at the conditions in the bubble column. Air, being a compressible gas, requires analysis of the static and dynamic pressure involved to assume pseudo-incompressibility. The maximum hydrostatic pressure of 0.8 m water on the sparger plate is 7848 Pa, which is about 7.7% of the reference atmospheric pressure. Therefore, compressibility due to hydrostatic pressure is assumed to be negligible. Likewise, the compressibility of air as a result of dynamic pressure can be estimated using the physical Mach number as defined in equation (3.1). Air can be considered pseudo-incompressible for low Mach number flows ($Ma < 0.3$) [26, 27].

$$Ma = \frac{|u_{f,2}|}{c_{f,2}} < 0.3 \tag{3.1}$$

The Mach number needs to be determined for each case individually, since the Mach number depends on the velocities of the fluid which in turn depend on the sparging rate. During start-up several peaks in max velocity are observed. These peak are excluded since they are transient and do not occur after the flow is developed. All cases meet the criterium set in equation (3.1) except for case 4, the full-scale turbulent case. However, looking at the velocity field in detail shows that these velocities only occur in a few grid cells near the inlets. Hence, the assumption of incompressibility near the sparger inlets is incorrect. This may result in inaccuracies in the fluid dynamics in the near-sparger region. Additional analysis would be required to study whether these compressibility effects significantly affect the results outside the near-sparger region. Since case #4 is not available at time of writing, these results are not included anyway.

Table 3.5: Maximum Mach numbers per case for $t > 5\,\mathrm{s}$.

#	Case name	Max. velocity	Ma
1	Volger half-scale bubbly	$35.2\,\mathrm{m\,s^{-1}}$	0.101
2	Volger half-scale turbulent	$79.6\,\mathrm{m\,s^{-1}}$	0.229
3	Volger full-scale bubbly	$46.8\,\mathrm{m\,s^{-1}}$	0.135
4	Volger full-scale turbulent	$149\,\mathrm{m\,s^{-1}}$	0.429

3.3. Discretisation

3.3.1. Grid independence

Performing a rigorous grid-independence study on this model is difficult, since the LBM is generally performed on a uniform grid and a certain minimum resolution is required to resolve the holes in the sparger plate. At these resolutions, computation times already become prohibitive for multiple simulations at scales where reliable validation data is available. Hence, the maximum feasible resolution was chosen for the full-scale geometry given the available resources on the DelftBlue supercomputer and the allotted project time. For the half-scale geometry, the maximum resolution was chosen given the available (V)RAM resources on the NVIDIA GeForce RTX 4090. The resulting grid resolutions are shown in table 3.6.

The Fluid-Particle conversion diameter is set to four grid cells in accordance with Ling et al.[37] as was discussed at the start of section 2.2. Below this diameter bubbles become underresolved. Hence why fluid parcels are converted into Lagrangian particles. The resulting diameter of Fluid-Particle conversion $d_{p,FPC}$ for each case is shown in table 3.6. The diameter of particle to fluid conversion $d_{p,PFC}$ is set such that the spherical volume is 5% higher than the volume corresponding to the Fluid-Particle conversion diameter.

Table 3.6: Grid sizing and diameters for Fluid-Particle and Particle-Fluid conversion between the ITF and EL models.

Case #	Lattice resolution	Δx	$d_{p,FPC}$	$d_{p,PFC}$
1	224 × 1202 × 224	0.446 mm	1.786 mm	1.815 mm
2	224 × 1202 × 224	0.446 mm	1.786 mm	1.815 mm
3	360 × 1696 × 360	0.533 mm	2.133 mm	2.168 mm
4	360 × 1696 × 360	0.533 mm	2.133 mm	2.168 mm

3.3.2. Time-step independence

When using the LBM, a time-step is chosen such that the fluctuation in the Lattice-Boltzmann density remain below about 1%. Fluctuation in the LB density can lead to inaccuracies and divergence of the model, since this LBM implementation assumes a constant density under fluid incompressibility. For LBM, a Courant number below 0.10 based on the maximum reference velocity (u_{max}) has been found to assure stable simulations [92]. It should be noted that in stirred systems, the maximum reference velocity is generally known a priori as it equivalent to the tip speed of the impeller. Since the maximum fluid velocity in a bubble column is hard to predict due to the chaotic movements of bubbles and interfaces, an adequate time-step was found iteratively and adjusted until it matched the numerical stability criterion (equation (3.2)). Plots of the lattice Boltzmann density over time for cases #3 and #4 can be found in appendix D: figure D.1.

$$Co = \frac{u_{max}\Delta t}{\Delta x} < 0.1 \tag{3.2}$$

3.4. Boundary conditions

All walls and the sparger plate have no-slip boundary conditions applied. These boundaries are of the grid-aligned half-way bounce-back type. In the half-scale column, the bottom of the sparger box is set as a uniform velocity inlet boundary condition and the sparger is included as an internal geometry. In the full-scale column, the bottom side of the sparger holes are each set as a uniform velocity inlet boundary condition such that the volumetric inflow aligns with experimental measurements. Due to resolution limitations, these inlet boundary conditions are quite underresolved (table 3.7). The meshing algorithm in M-Star CFD is 'greedy', in the sense that when a grid cell intersects **any** part of a solid geometry, it is considered a no-slip boundary. Due to keeping the sparger hole diameter constant between the half-scale and full-scale geometries, this underresolution is not significant for the half-scale simulations. The top of the column is a gas pressure outlet boundary condition set at the reference pressure (table 3.4).

Table 3.7: Degree of inlet resolution in the full-scale column. Labelled according to figure 3.2b.

Inlet labels	**Grid cells**	**Resolved area** [m^2 / %]
Inlet 0	14	3.98×10^{-6} / 56%
Inlet 1	14	3.98×10^{-6} / 56%
Inlet 2	16	4.55×10^{-6} / 64%
Inlet 3	12	3.41×10^{-6} / 48%
Inlet 4	16	4.55×10^{-6} / 64%
Inlet 5	14	3.98×10^{-6} / 56%
Inlet 6	14	3.98×10^{-6} / 56%
Inlet 7	16	4.55×10^{-6} / 64%
Inlet 8	16	4.55×10^{-6} / 64%
Inlet 9	12	3.41×10^{-6} / 48%
Inlet 10	16	4.55×10^{-6} / 64%
Inlet 11	16	4.55×10^{-6} / 64%

3.5. Lagrangian bubble model

Using the theoretical background explored in section 2.2, a Langrangian bubble model was developed based on the M-Star CFD discrete particle model (DPM). Particles are created using fluid particle conversion for fluid droplets with a diameter smaller than $4\Delta x$. One-way particle centroid method (PCM) coupling is applied from the fluid to the particles, since the particles represent less than 10% of the total holdup. All forces from the momentum balance shown in equation (2.13) are included except for the pressure gradient force, resulting in equation (3.3).

$$\vec{F}_{p,i} = m_{p,i}\frac{d\vec{u_{p,i}}}{dt} = \vec{F}_{GB,i} + \vec{F}_{M,i} + \vec{F}_{D,i} + \vec{F}_{L,i} \tag{3.3}$$

The pressure gradient force is excluded because the radial pressure gradients are minor compared to other forces. The drag and lift forces calculated based on the correlations developed by Tomiyama et al. [44, 47]. The buoyancy, gravity and virtual mass forces are included based on M-Star CFD's default implementations [34]. Bubble breakup is modelled according to the modified Mast & Takors critical Weber number model as shown in appendix A. A critical Weber number of 6.1 is used [17]. Bubble coalescence is modelled according to an M-Star implementation of the Euler-Lagrange version of the film drainage model based on work by Sommerfeld et at. which was based on work by Prince & Blanch [52, 68]. The M-Star implementation of the Sommerfeld model is shown in appendix A.

3.6. Computed tomography

Tomographic reconstruction methods were implemented using the ASTRA toolbox [93, 94]. The usage of the ASTRA toolbox simplifies the implementation of reconstruction techniques suited to specific problems. In short, the ASTRA toolbox constructs the system matrix $\boldsymbol{A}$ (see section 2.3) as a linear operator based on the spatial geometry of the tomography setup and provides the backend for computing matrix-vector products with $\boldsymbol{A}$ and $\boldsymbol{A}^T$. Furthermore, the ASTRA toolbox provides several built-in implementations of common (reconstruction) algorithms, including FBP and SIRT.

3.6.1. Spatial projection geometry

The source-detector pairs are uniformly distributed in the angular direction around the bubble column at constant radial distances (figure 3.4). The detector specification are based on the CMOS detectors of the TU Delft experimental setup [25]. These data combined in table 3.8 where the detector-origin distances are described from the centre of the detector plane. The volume output rate of the CFD simulation is set to 22 Hz to align with experimental frame rates.

The volume outputs of the CFD simulation are converted to a density field for forward projection based on the ITF gas volume fraction $\varphi_{f2,ITF}$, which is equivalent to the value of the phase indicator function ϕ, and EL gas volume fraction φ_p according to equations (3.4) and (3.5). The grid cells that lie above and below the field of view of the X-ray setup in the axial direction are excluded to improve performance. The density of grid cells outside the cylindrical fluid domain are set to zero. Attenuation arising from the column wall is neglected. It should be noted that some effects present in experimental data such as motion blur and a non-point X-ray source are not present in simulated data. Motion blur and a larger focal spot would result in smoother transitions in density between phases. However, due to limitations in the ITF model, the air-water interfaces have a diffuse interface width of around four grid cells [30]. In order to very roughly approximate, these interface were kept diffuse to roughly approximate these smoothing effects. For two-phase systems were these blurring effects are not significant, a threshold may be applied to the density field to define interface rather than keeping it diffuse.

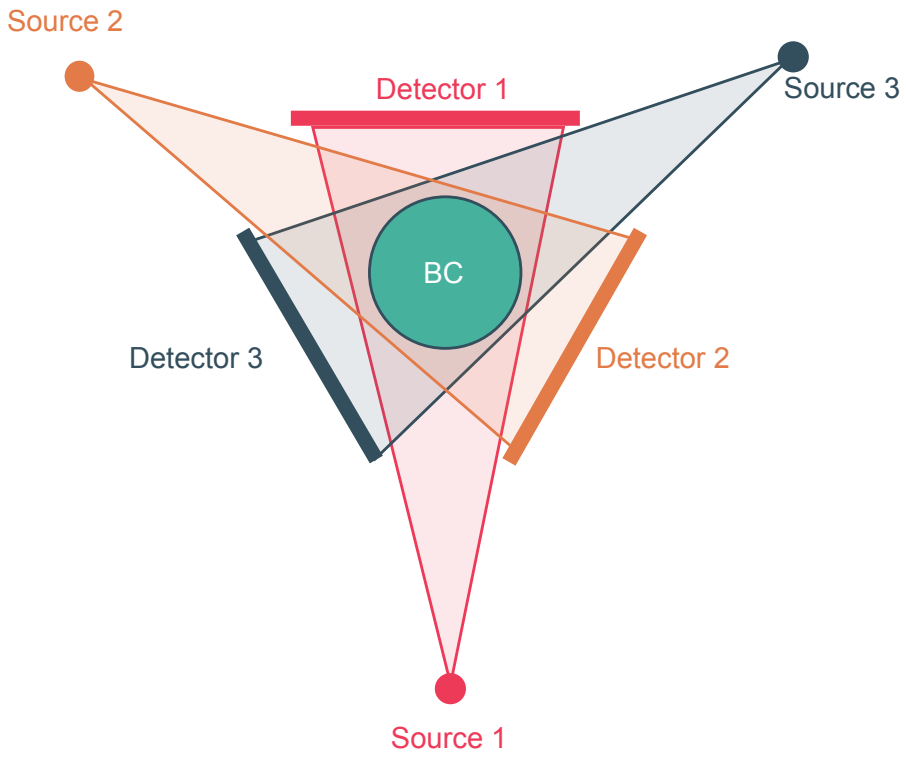

Figure 3.4: Schematic of the X-ray setup. Diagram by Sam den Hartog, reproduced with permission.

Table 3.8: Virtual X-ray setup geometry specifications: Bubble column

Detector specifications	**Dimension**
Resolution	1548 × 1524
Pixel spacing	0.2 mm/pixel
Frame rate (max. 200 Hz)	22 Hz
X-ray setup geometry	
Radial source-origin distance	0.940 m
Radial detector-origin distance	0.275 m
Axial source-origin distance	0.450 m
Axial detector-origin distance	0.450 m
Number of angles	3

$$\varphi_{f2} = \varphi_{f2,ITF} + (1 - \varphi_{f2,ITF})\varphi_p \tag{3.4}$$

$$\rho = \varphi_{f2}(\rho_{f2} - \rho_{f1}) + \rho_{f1} \tag{3.5}$$

For the 3D Shepp-Logan phantom, the following projection geometry is used (table 3.9). The detector and X-ray setup geometry are set to include the entire phantom. The phantom is generated using the ASTRA toolbox function `data3d.shepp_logan` in a 256 × 256 × 256 volume geometry. A noise level of 2% is used which is approximately the noise level in the experimental setup. The background intensity value I_0 used in the `add_noise_to_sino` function is set to 20,000 to achieve the correct noise level for the Shepp-Logan phantom.

Table 3.9: Virtual X-ray setup geometry specifications: Shepp-Logan phantom.

Detector specifications	**Dimension**
Resolution	256 × 256
Pixel spacing	1.5 pixel
X-ray setup geometry	
Radial source-origin distance	768
Radial detector-origin distance	$\sqrt{512}$
Number of angles	379

3.6.2. Reconstruction geometry

The reconstruction geometry is set based on the resolution of the CFD simulation output and its relation to the projection geometry. Only a subsection of the CFD simulation is intersected by the cone beam. Hence, the volume geometries used for forward projections and reconstructions are cropped to the axial section of the CFD simulation which is intersected by any cone beam. The volume geometry is further cropped to the voxels intersected by all three cone beams when calculating the reconstruction error and plotting reconstructions (figure 3.5).

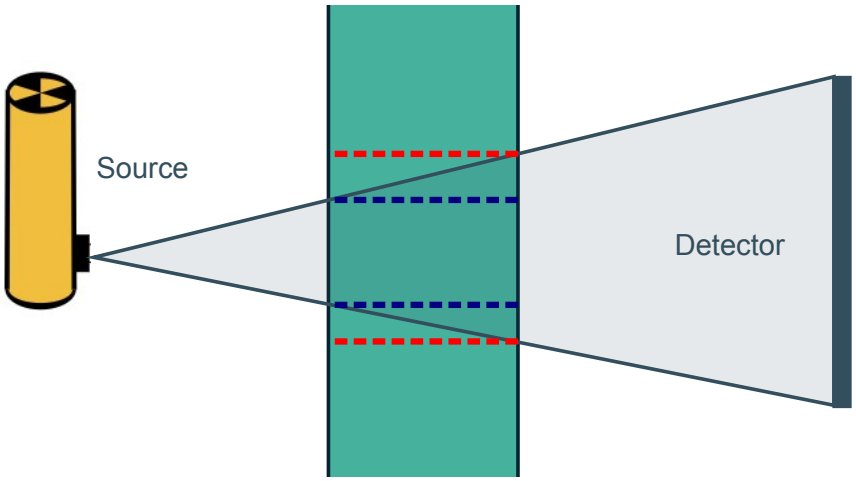

Figure 3.5: Schematic of the axial cropping of the volume geometry. Red line: cropping applied for forward projection and backward projection. Blue line: cropping applied for calculated error and plotting reconstructions. Base diagram by Sam den Hartog, reproduced with permission.

Outside the cylindrical simulation domain, the box constraints are not applied and the density is set to zero. In order to prevent issues when determining gradients for the *SIRT+dT* algorithm,

the boundary voxel on the outside of the simulated domain is set to the same value as the bordering voxel. If two voxels border the boundary voxel, the maximum value of the two is used. A similar boundary condition ought to be applied for the *TVmin* algorithm when calculating the total variation, but this was not implemented due to time constraints.

3.6.3. Sinogram noise level

Poisson noise is applied to the sinogram in order to approximate the noise level found in the experimental setup. The experimental setup's noise level was determined by taking the data from a stationary column measurement and determining the normalised root mean square error (NRMSE) compared to the time-averaged sinogram $\bar{\boldsymbol{b}}$ according to equation (3.6). Since no gas is sparged into the column, all variance in the X-ray measurement can be assumed to be the result of photon and detector noise. The noise measurement was taken over 10 seconds resulting in 220 samples which should provide a good estimate of $\bar{\boldsymbol{b}}$.

$$\mathrm{NL} = \frac{\|\boldsymbol{e}\|_2}{\|\bar{\boldsymbol{b}}\|_2} = \frac{\|\boldsymbol{b} - \bar{\boldsymbol{b}}\|_2}{\|\bar{\boldsymbol{b}}\|_2} \tag{3.6}$$

Based on this measurement the setup noise level of each time step NL_s is 2%. This noise level was reproduced in the virtual setup using the ASTRA toolbox using the `add_noise_to_sino` function, which takes a background intensity I_0 as an input. A background intensity value of 10,000 was found to produce a similar noise level of around 2% for the simulated bubble columns.

4

Results

4.1. CFD Model validation

In order to validate the results produced by the CFD model developed in chapter 3, results are compared to experimental data. However, experimental data on the hydrodynamics of the Volger bubble column is limited. Therefore, simulations were compared to literature data by Sanyal et al. on a bubble column with similar dimensions at similar superficial gas velocities. Due to time constraints, the results of case #3 are limited to the time range of 5 s to 10 s and the results of case #4 are unavailable at time of writing. The half-scale results from cases #1 and #2 are available in their entirety over the 5 s to 15 s time range.

Before outputting any fluid variables, the flow is allowed to the develop. The condition for flow development was based on a stabilisation of the fluid kinetic and potential energy which occurred after 5 s (see appendix D: figure D.2).

4.1.1. Literature comparison to Sanyal et al.

The geometry of the Sanyal column is taken from the 1999 paper by Sanyal et al, the dimensions of which are shown in table 4.1 [2]. The main differences between the Sanyal and Volger (see table 3.2) bubble columns are related to the sparger plate geometry. The Sanyal column's perforated sparger plate has approximately 330 holes based on the sparger hole diameter and open area, compared to only 12 holes in the Volger sparger plate. Note that the hole diameter reported in the paper by Sanyal et al. (0.33 mm) contradicts the number provided by Kumar (0.5 mm) [cf. 95, p. 112]. The open area of Volger sparger plate (0.3%) is three times that of the Sanyal sparger (0.1%). While the sparger geometry does influence the overall flow in the bubble column, the effects outside the near-sparger region are on the order of $\pm 10\%$. Therefore, these differences are assumed to be negligible [95, 96]. One exception being the regime transition from bubble flow to churn-turbulent, which is strongly influenced by the sparger geometry with less uniform spargers generally transitioning at lower superficial velocities. These effects have been explored in detail in a review by Ruzicka et al. [97]. Due to the Volger sparger plate being less uniform compared to the sparger plate of the Sanyal column, the transition to the heterogenous regime is expected to take place at lower superficial gas velocities. The fill height of the Volger column is lower. In all other regards, the Sanyal and Volger geometries are similar.

Initially, an attempt was made to simulate the Sanyal column using a uniform inlet boundary condition at the sparger plate. This resulted in an annular flow pattern which is not observed

experimentally. The resolution required to capture the Sanyal sparger geometry is prohibitively high in terms of computational resources. Therefore, simulation of the Sanyal geometry using the CFD model developed in this thesis for direct comparison with experimental data was not possible. However, due to the similarities in geometry, the Sanyal and simulated Volger bubble columns were compared directly.

Table 4.1: Sanyal bubble column and sparger plate dimensions reproduced from Sanyal et al. (1999) [2].

	Dimension
Column height	1.20 m
Column internal diameter	0.190 m
Fill height ($u_s = 0.02\,\mathrm{m\,s^{-1}}$)	1.045 m
Fill height ($u_s = 0.12\,\mathrm{m\,s^{-1}}$)	0.950 m
Sparger hole diameter	0.33 mm
Sparger open area	0.1%

Sanyal et al. performed measurements on the Sanyal column using a combination of X-ray CT and CARPT at superficial velocities of 0.02 m s^{-1} (homogeneous bubble regime) and 0.12 m s^{-1} (heterogeneous churn-turbulent regime) [2, 24, 95]. However, reproducing the high superficial velocity of 0.12 m s^{-1} in the simulated Volger column is computationally unfeasible. Therefore, only the results for the lower superficial velocity of 0.02 m s^{-1} can be quantitatively compared with the simulated data. However, the Sanyal churn-turbulent case can be used as an upper bound for the Volger churn-turbulent case in holdup, velocities and turbulent kinetic energy.

Holdup profiles

The gas holdup profile of the Sanyal column was determined experimentally using CT at a height of 53 cm above the sparger plate [95]. However, Sanyal et al. do caution that: 'Unfortunately, the experimental data for gas holdup at this condition were not of the highest accuracy.', when referring to the holdup measurements taken at a superficial velocity of 0.02 m s^{-1} [2].

As noted in section 3.1.1, the current CFD simulations do not conform to the scale-up criteria by Wilkinson et al.[86] Therefore, the gas holdup of both the half- and full-scale columns are not generalisable for larger scale bubble columns. Despite the diameter under 15 cm, slug flow was not observed for the half-scale column even at the higher superficial velocity of 4.6 cm s^{-1}.

The holdup profiles will be compared on the flatness of the holdup profile and the average holdup over the column. Compared to the experimental holdup data at low superficial gas velocities (case #1 / case #3), the holdup in the simulation is underestimated for both the full and half scale columns (figure 4.1). Sanyal et al. also reported a lower holdup profile in their CFD simulations [2]. As mentioned previously, the experimental data for the lower u_s (2.0 cm s^{-1}) were considered inaccurate by Sanyal et al. This indicates a possible overestimation of the holdup in this experimental data. Additional experimental measurement of the (mean) holdup in the Volger column could be used as verification of this conjecture. The holdup profile is more flat for the full-scale than the half-scale column results. This may be explained due the boundary layer near the wall taking up a larger section of the dimensionless radius in the half-scale column.

The half-scale simulation at the higher superficial gas velocities (case #2) shows a higher holdup and a more parabolic holdup profile. Assuming that the experimental data at $u_s = 2.0\,\mathrm{cm\,s^{-1}}$ is overestimated, the holdup profile lies between the two experimental measurements. Considering that the experimental churn-turbulent case can be considered an upper

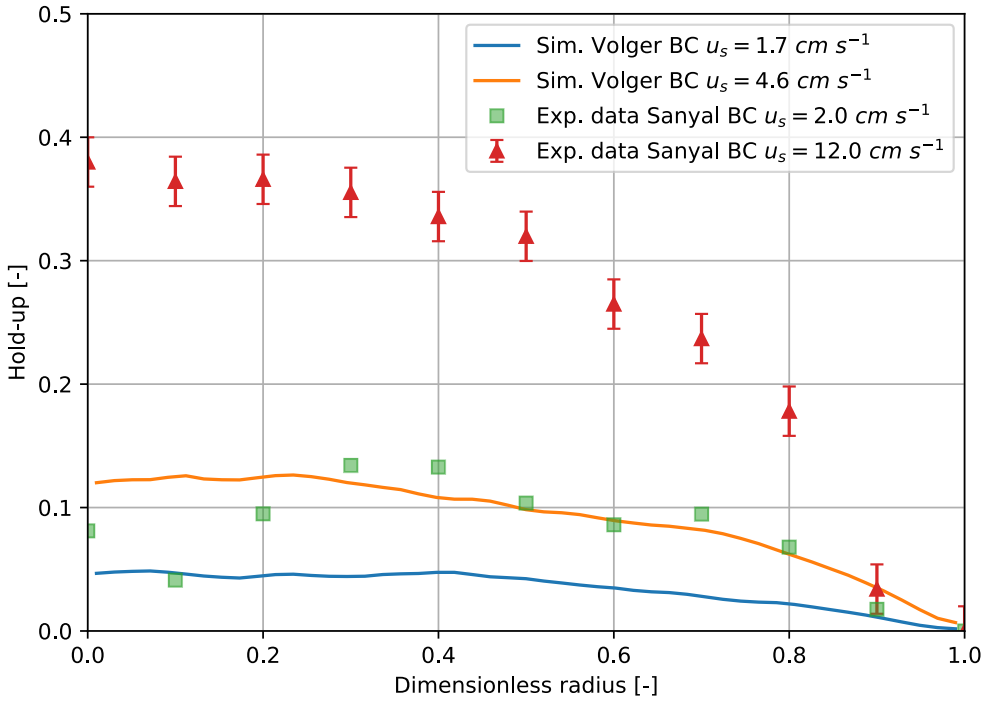

(a) Half-scale column (case #1 / case #2) at $Y = 26.5\,\mathrm{cm}$ over $5\,\mathrm{s} \leq t \leq 15\,\mathrm{s}$.

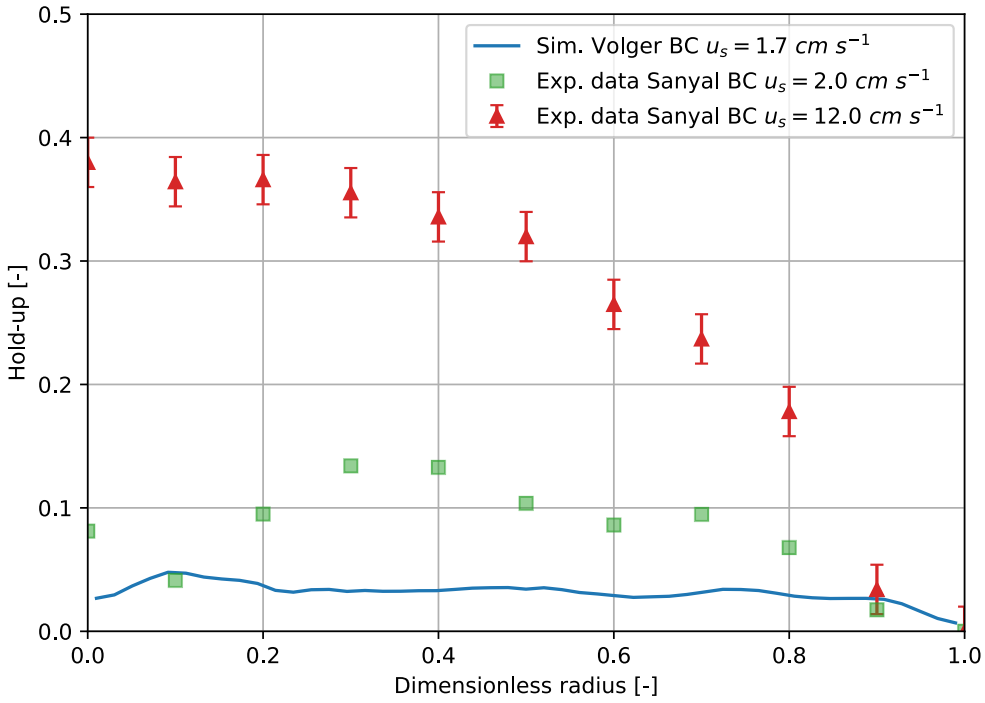

(b) Full-scale column (case #3) at $Y = 53\,\mathrm{cm}$ over $5\,\mathrm{s} \leq t \leq 10\,\mathrm{s}$.

Figure 4.1: Comparisons of holdup profiles between the Sanyal column and half- / full-scale Volger columns. Note that Epx. data Sanyal BC $u_s = 0.02\,\mathrm{cm\,s^{-1}}$ are considered inaccurate and therefore are plotted with transparency.

bound on holdup and that holdup increases when increasing the sparging rate, the results for this case are line with theoretical expectations.

Therefore, the holdup profiles generated by the current model can be considered valid within the limitations of the available data. Additional comparision to experimental holdup data from the Volger column collected using pressure probes could be used in future as additional validation of the mean holdup.

Axial velocity profiles

Instantaneous fluid velocities were measured in the Sanyal column using CARPT [2, 24]. CARPT allows for measurement of the local fluid velocity near the tracked particles. By measuring over the course of several hours, a representative sample of these instantaneous velocities can be taken over the fluid domain. Consequently, instantaneous velocities can be divided into a mean time-averaged velocity component $\overline{\vec{u}}$ and a fluctuating velocity component $\vec{u}'$ via Reynolds decomposition [98] (equation (4.1)).

$$\vec{u} = \overline{\vec{u}} + \vec{u}' \tag{4.1}$$

Reynolds decomposition is performed likewise on the velocities in the simulations. The experimentally measured axial component of the time-averaged velocity is compared to the simulation results (figure 4.2).

Examined features of the velocity profile are the overall shape of the profile, the cross-over point where the mean axial velocity becomes zero and the maximum / minimum axial velocities. Starting with the simulation data from the half-scale column (case #1 / case #2) in figure 4.2a, the velocity profiles of the experimental Sanyal and simulated Volger columns match closely for the bubbly regime in all previously described features except for a slight underprediction of the minimum axial velocity. For the churn-turbulent regime, the velocity profile lies firmly between the measurements by Sanyal. A small underprediction is once again observed near the minimum axial velocities.

The simulation results from the full-scale column (case #3) in figure 4.2b show a strong deviation from the measured velocity profile in the Sanyal column. Plotting the time-averaged axial velocity across the axial slice shows that the upwards plume is deviated in the negative X direction. This coincides with the more resolved inlets on the negative X side of the bubble column as shown in figure 3.2b.

Therefore, while the mean velocity profiles generated by the current model for the half-scale geometry can be considered valid, the velocity data produced for the full-scale model is not valid due to underresolution of the inlets. This may be addressed by rerunning the simulation using either a higher resolution or an altered geometry (artificially increasing the sparger hole diameter during meshing) for which the greedy meshing algorithm provides less underresolved inlet geometries.

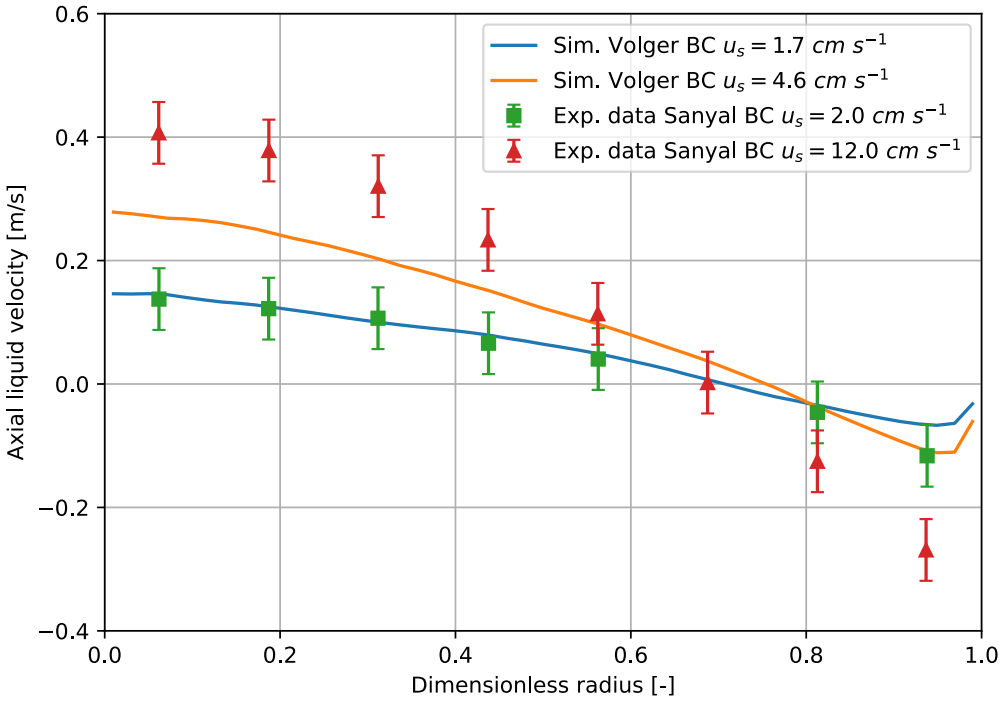

(a) Half-scale column (case #1 / case #2) at $Y = 26.5\,\mathrm{cm}$ over $5\,\mathrm{s} \leq t \leq 15\,\mathrm{s}$.

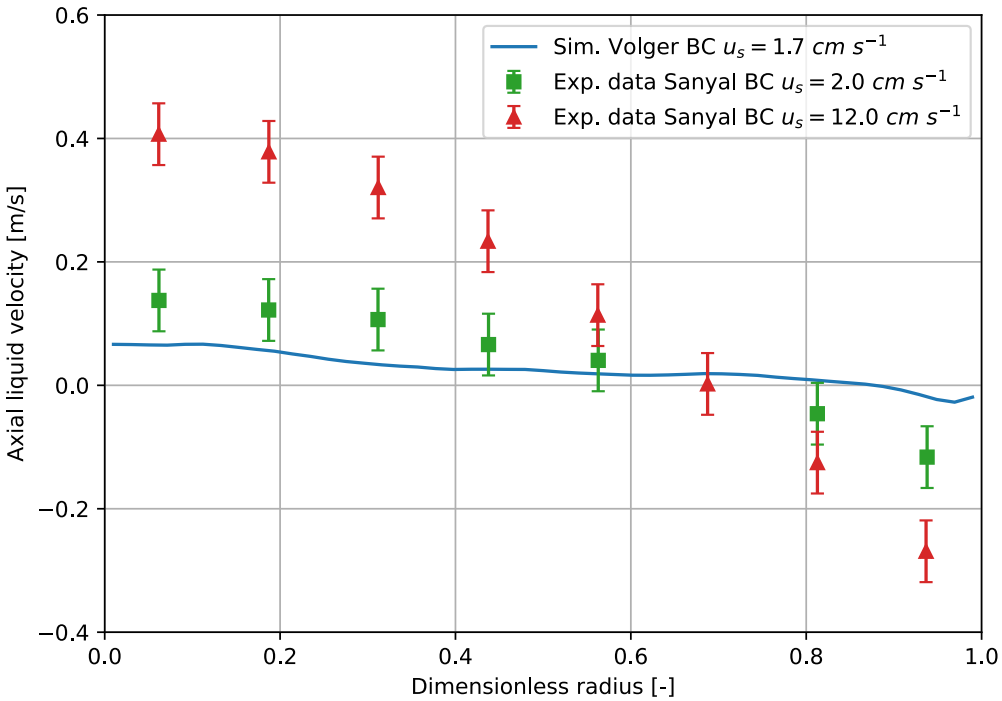

(b) Full-scale column (case #3) at $Y = 53\,\mathrm{cm}$ over $5\,\mathrm{s} \leq t \leq 10\,\mathrm{s}$.

Figure 4.2: Comparisons of time-averaged axial velocity profiles between the Sanyal column and half- / full-scale Volger columns.

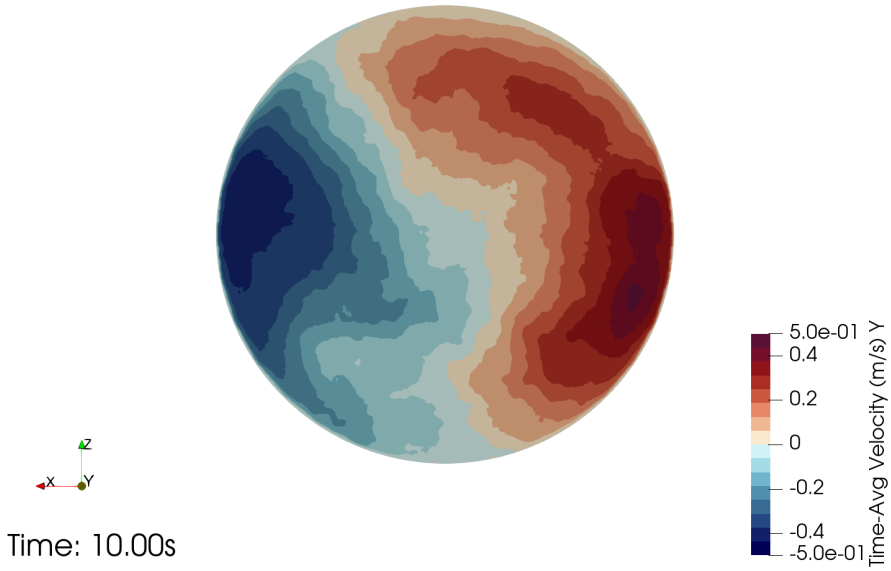

Figure 4.3: Contour plot showing the time-averaged axial velocity in the full-scale column (case #3) at $Y = 53\,\mathrm{cm}$ over $5\,\mathrm{s} \leq t \leq 10\,\mathrm{s}$.

Turbulent kinetic energy profiles

As stated in the previous section, both the time-averaged and fluctuating components of the velocity can be determined using CARPT [2, 24]. The turbulent kinetic energy k can be calculated from the variance of the fluctuating velocity component (equations (4.1) and (4.2)). The experimental measurement of the fluctuating velocity component using CARPT is limited by the response time of the particle to velocity fluctuations in the fluid at frequencies above 20 Hz to 25 Hz. This limitation is not present in the simulation results. In the simulation, all deviation from the time-averaged velocity field over the simulated interval are included in the turbulent kinetic energy. Therefore, the experimental turbulent kinetic energy is underestimated compared to the simulation.

$$k = \frac{1}{2}\,\mathrm{Var}(\vec{u}') = \frac{1}{2}\overline{(\vec{u}' \cdot \vec{u}')} \tag{4.2}$$

The turbulent kinetic energy profiles in figure 4.4 are compared based on profile shape and average energy over the column. Starting with case #1 and case #3, the turbulent kinetic energy is double the experimental measurement. The energy in experimental data being lower, but in the same order of magnitude shows close agreement with expectations. The energy profile for case #1 shows a decline towards the outer wall, while case #3 shows a more flat profile. This may once again be explained by the boundary layer near the wall taking up a larger section of the dimensionless radius in the half-scale column. Moving on to case #2, the turbulent kinetic energy is high, on the same order as the Sanyal churn-turbulent measurement, despite having only 40% of the superficial velocity. This may be explained by the non-uniformity of the Volger sparing plate leading to a transition to the churn-turbulent regime at lower superficial velocities. The highest turbulent kinetic energy occurs in the centre of the column rather than around the velocity crossover point. Future comparison with case #4 can provide insight into whether this discrepancy is due to the difference in geometry or

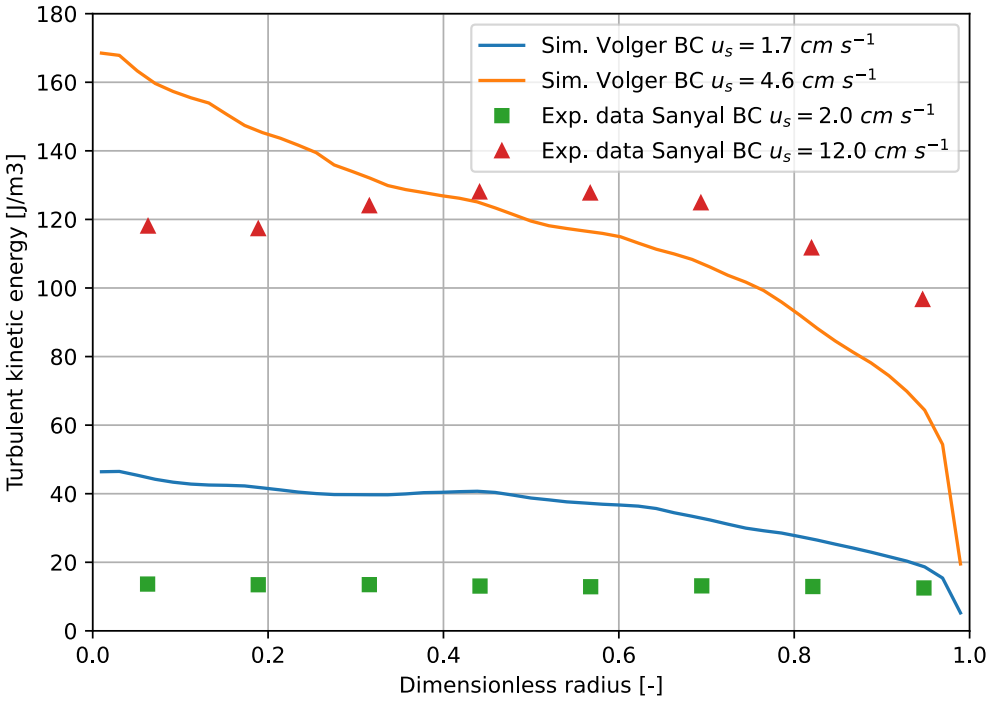

(a) Half-scale column (case #1 / case #2) at $Y = 26.5\,\mathrm{cm}$ over $5\,\mathrm{s} \leq t \leq 15\,\mathrm{s}$.

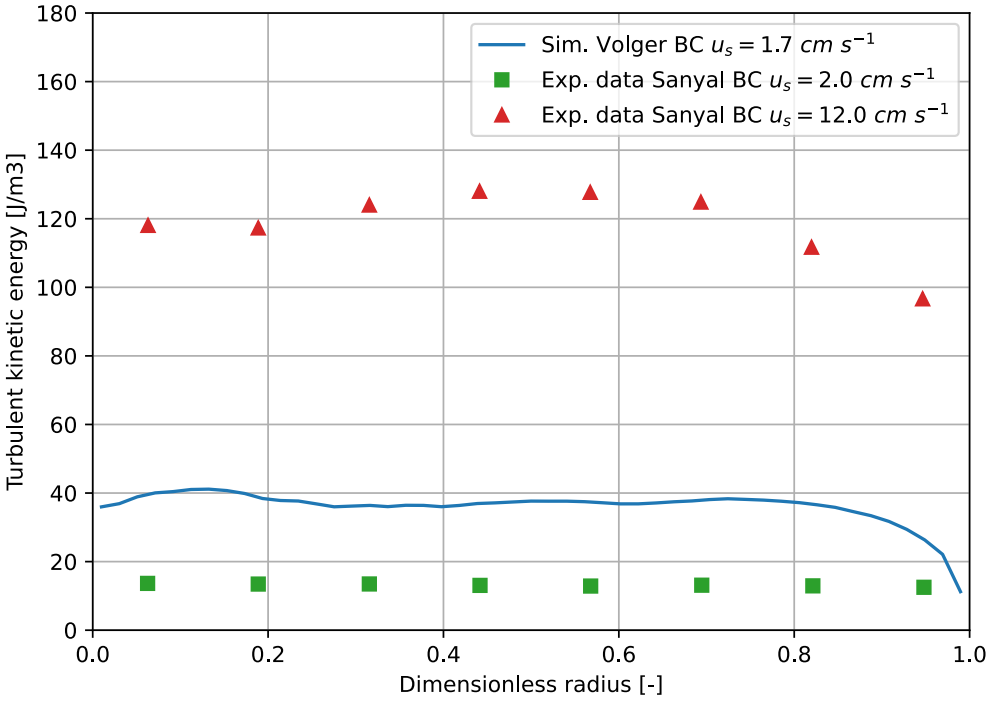

(b) Full-scale column (case #3) at $Y = 53\,\mathrm{cm}$ over $5\,\mathrm{s} \leq t \leq 10\,\mathrm{s}$.

Figure 4.4: Comparisons of kinetic energy profiles between the Sanyal column and half- / full-scale Volger columns.

inherent to the fluid model.

One source of error in the turbulence field can be the velocity filter in the ITF model, which provides additional viscosity in areas with high velocities in order to preserve numerical stability. Turbulent fluctuations in velocity can be reduced when such perturbations lead to velocities exceeding the velocity filter threshold. While the velocity filter can be disabled, doing so leads to severe numerical instability.

Sanyal et al. discuss the limitations of turbulent kinetic energy as a proxy for the accuracy of the turbulence model [2]. Although turbulent kinetic energy shows the total magnitude of the velocity fluctuations across all scales of turbulence, it provides no information on whether the models accurately captures the velocity fluctuations at any specific scale. Therefore, accurate reproduction of the turbulent kinetic energy profile does not necessarily imply that the entire turbulence field is accurately captured. However, an inaccurate reproduction of the turbulent kinetic energy profile does show that the turbulence field is not accurately captured.

In summary, the turbulent kinetic energy in the homogeneous bubbly cases (case #1 / case #3) is captured accurately using the current model. However, the turbulent kinetic energy in the heterogeneous churn-turbulent case (case #2) shows features which deviated from the experimental results. Without data from case #4, it is not possible to show whether this is due to the half-scale geometry or an inherent issue with the fluid model.

4.2. Computed Tomography validation & performance

Four reconstruction algorithms were implemented and compared on performance: SIRT, SIRT with standard Tikhonov regularisation (*SIRT+sT*), SIRT with generalised Tikhonov regularisation using the derivate operator (*SIRT+dT*) and Total Variation minimisation using the Chambolle-Pock algorithm (*TVmin*). Furthermore, a new reconstruction algorithm *SIRT+sT Offset* is derived by shifting the Tikhonov regularisation parameter from *SIRT+sT*. These methods are explained in detail in section 2.3.2. How well these different methods perform under idealised conditions is shown in appendix C.

4.2.1. Time-resolved bubble fields

Time-resolved bubbles field were generated using the CFD simulation developed previously. Only data from case #3 is used, since data from case #4 is unavailable at time of writing. Applying the reconstruction algorithms to the time-resolved bubble fields using the three-angle X-ray geometry (table 3.8) requires finding the appropriate regularisation parameter values. The values of α of 0.0008 for *SIRT+sT* / *SIRT+dT* and 0.15 for *TVmin* were chosen by minimising the NRMSE of reconstruction at a noise level of 2%. 250 iterations were found to be sufficient to achieve good convergence for the *SIRT+sT* and *SIRT+dT* algorithms. For the *TVmin* algorithm, the first 50 pre-iterations are applied using the *SIRT+dT* algorithms. After which 1000 iterations of the *TVmin* algorithm were found to be sufficient for convergence. SIRT with the discrepancy principle stopping rule is included as a baseline for comparison (figure 4.5). The box constraints are set to the densities of air (minimum) and water (maximum).

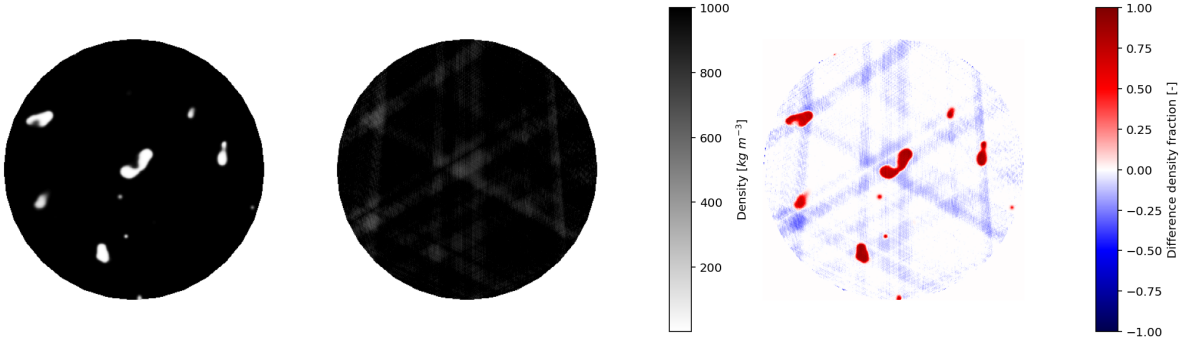

(a) Horizontal slice. Left to right: ground truth, reconstruction, difference.

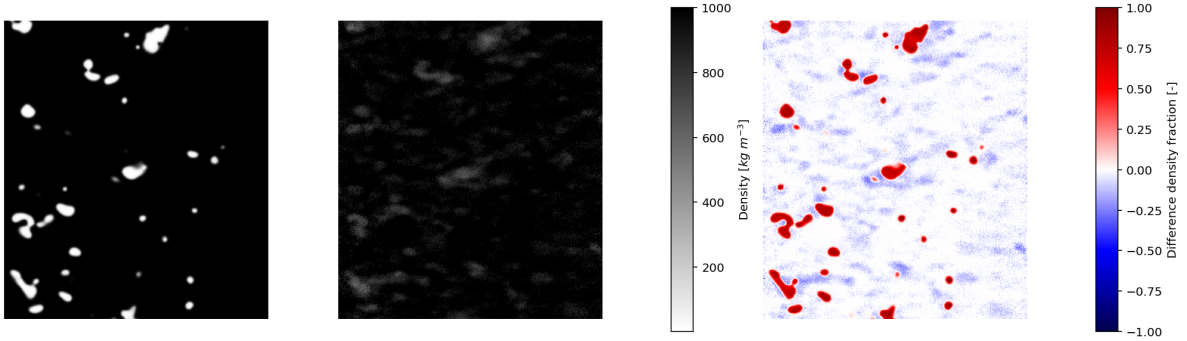

(b) Vertical slice. Left to right: ground truth, reconstruction, difference.

Figure 4.5: SIRT reconstruction using the DP stopping rule of the full-scale transient bubble field (case #3) at $t = 5.545\,\mathrm{s}$. Number of angles $= 3$, noise level $= 2\%$, iterations $= 250$.

The reconstruction generated using the *SIRT+sT* algorithm underestimates the density in the dense water phase (figure 4.6). This can be explained by Tikhonov regularisation applying an assumption of normality on the data with a mean at zero. This pushes the higher density

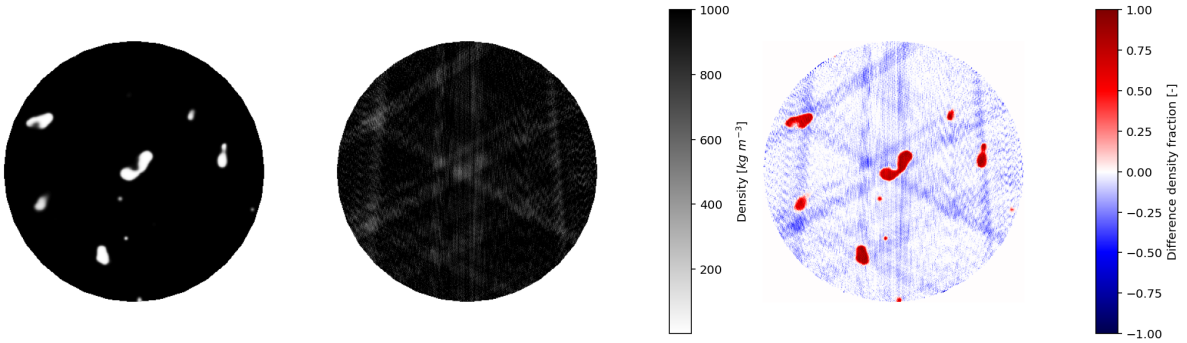

(a) Horizontal slice. Left to right: ground truth, reconstruction, difference.

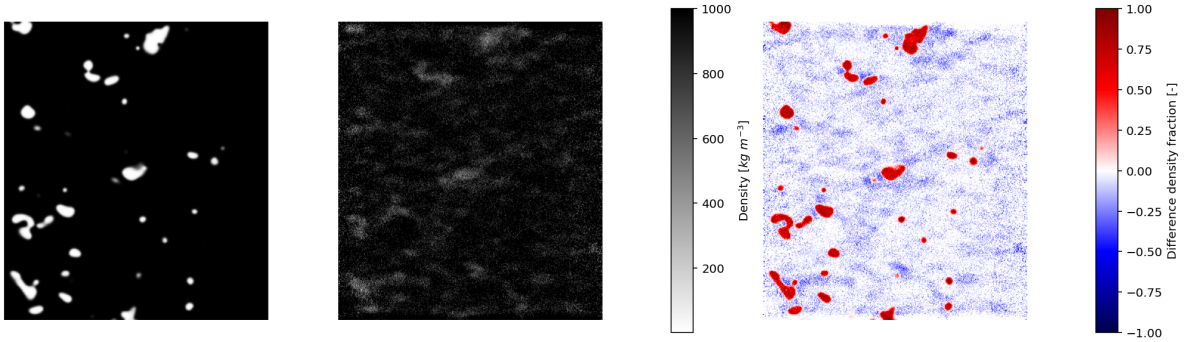

(b) Vertical slice. Left to right: ground truth, reconstruction, difference.

Figure 4.6: *SIRT+sT* reconstruction of the full-scale transient bubble field (case #3) at $t = 5.545\,\mathrm{s}$. Number of angles $= 3$, noise level $= 2\%$, $\alpha = 0.0008$, iterations $= 250$.

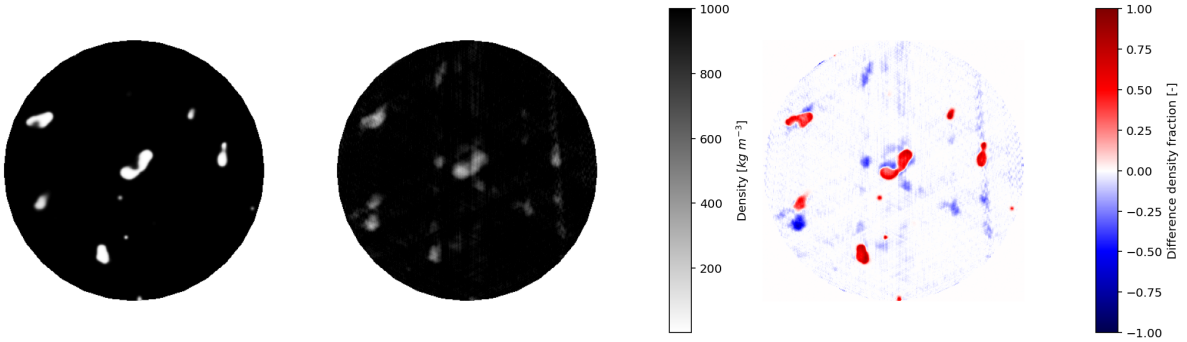

(a) Horizontal slice. Left to right: ground truth, reconstruction, difference.

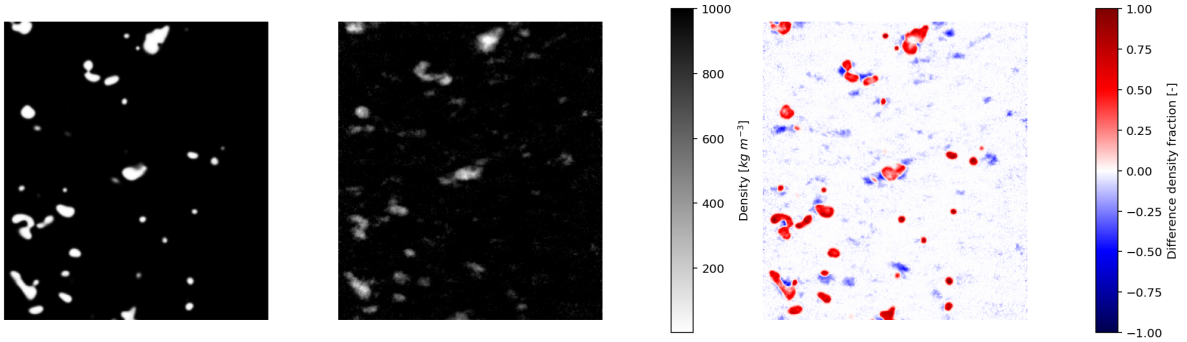

(b) Vertical slice. Left to right: ground truth, reconstruction, difference.

Figure 4.7: *SIRT+dT* reconstruction of the full-scale transient bubble field (case #3) at $t = 5.545\,\mathrm{s}$. Number of angles $= 3$, noise level $= 2\%$, $\alpha = 0.0008$, iterations $= 250$.

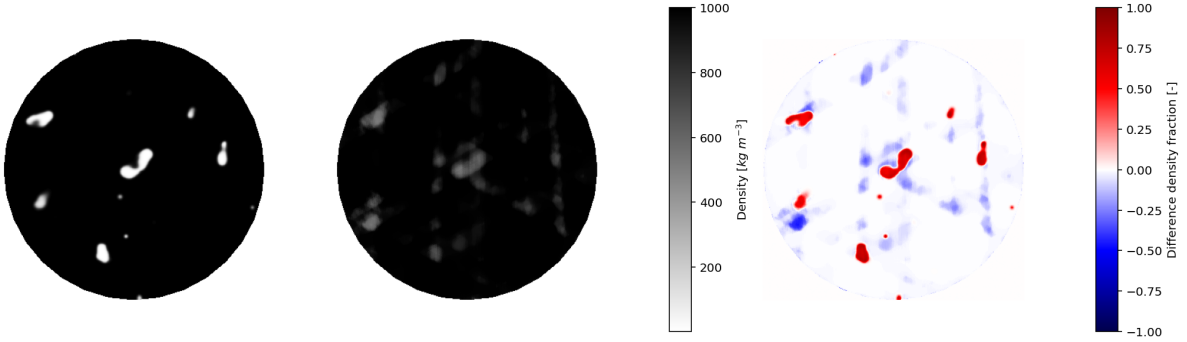

(a) Horizontal slice. Left to right: ground truth, reconstruction, difference.

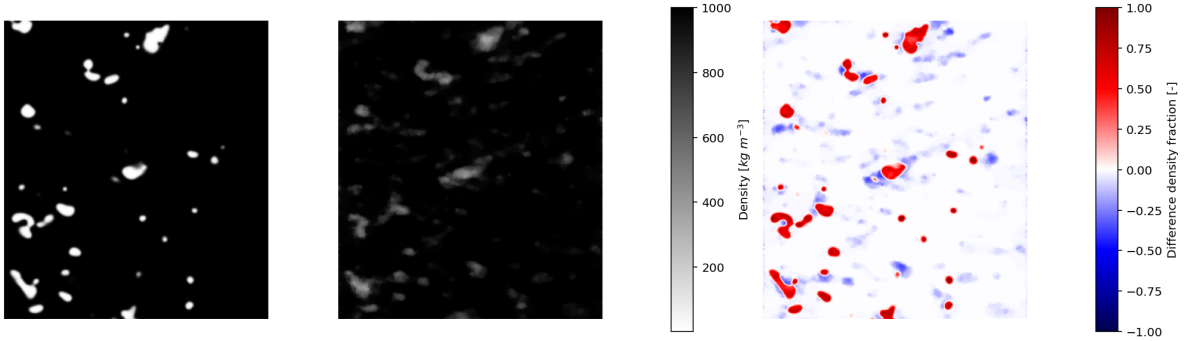

(b) Vertical slice. Left to right: ground truth, reconstruction, difference.

Figure 4.8: *TVmin* reconstruction of the full-scale transient bubble field (case #3) at $t = 5.545\,\mathrm{s}$. Number of angles $= 3$, noise level $= 2\%$, $\alpha = 0.15$, *SIRT+dT* pre-iterations $= 50$, iterations $= 1000$.

voxels down, leading to the density underestimation in the water phase. Increasing the regularisation parameter leads to lower noise level, but also increases this underestimation leading to higher errors. This underestimation limits the value of the regularisation parameter leading to a significant amount of salt and pepper noise. Furthermore, the reconstruction shows significant streaking artefacts in the horizontal slice. This algorithm is therefore unsuitable for the time-resolved bubble field data.

The reconstruction error can be quantified using the NRMSE between the reconstruction and the ground truth (table 4.2). This shows that the *SIRT+sT* algorithm underperforms even the baseline SIRT algorithm. The reconstruction generated using the *SIRT+dT* algorithm shows an improvement over both the SIRT and the *SIRT+sT* results (figure 4.7), which is reflected in the NRMSE. As stated in section 3.6.1, the air-water interfaces were left diffuse to emulate blurring effects from motion blur and a non-point X-ray source present in the experimental setup. Therefore, the smoothing applied by minimising the gradient in the *SIRT+dT* algorithm aligns with the smoothing in the underlying data. It should be noted that the degree of smoothing resulting from the diffuse interfaces in the ITF methods are only a very rough approximation of these experimental blurring effects. In experimental data, the blurring would likely be anisotropic and of a different magnitude depending on the velocity of the bubble structures and geometry of the focal spot in the X-ray source.

Despite improvement over *SIRT+sT*, there are still significant streaking artifacts present in the horizontal slice. Furthermore, there are numerous bubble-like artefacts where bubbles overlap on all three projections. These ‘spurious bubbles’ also increase the reconstructed density of the true bubbles by effectively spreading out the air phase along a ray over both the true and spurious bubbles. Such artifacts have also been reported by Graas et al.[25]

The *TVmin* reconstruction shows the least visual noise over the reconstruction compared to *SIRT+sT* and *SIRT+dT* (figure 4.8). This is reflected in the reconstruction error, though *TVmin* is outperformed slightly by *SIRT+dT* (table 4.2). The streaking artefacts are reduced compared to the other algorithms. However, spurious bubbles are still present in the reconstruction resulting in a similar overestimation of the density the true bubbles. The assumption of a piece-wise linear function applies quite well to the discrete phases of the bubble field. There may be some increase in reconstruction error due to the absence of smooth transitions near interfaces. Furthermore, an underestimation is observed near the outer cylindrical boundary. This is due to the lack of proper boundary conditions when calculating the total variation referred to in section 3.6.2. In the current implementation, there is a steep change in density between the fluid and the area outside the fluid domain which is set to zero. The algorithm converges to a solution which minimises this steep change, leading to an underestimation near this boundary.

Overall, the *SIRT+dT* algorithm performs best based on the NRMSE with the *TVmin* algorithm being a close second. The performance of the *TVmin* may be improved by implementing proper boundary conditions when computing the total variation. Additionally, other methods for solving the total variation minimisation problem besides the Chambolle-Pock algorithm are available which may be more performant and may require fewer iterations to converge [72, pp. 306–311] [99].

Table 4.2: NRMSE of reconstruction: time-resolved full-scale (case #3).

Algorithm	**Iterations**	**NRMSE**	**Change** [%]
SIRT (DP)	18	0.1123	baseline
SIRT+sT	250	0.1428	+27%
SIRT+dT	250	0.0867	-23%
TVmin	1000	0.0955	-11%

4.2.2. Binary classification

NRMSE is a useful measure of error for continuous data. However, a time-resolved immiscible two-phase system is more accurately represented as a binary system. Setting a threshold for the reconstructed density field allows for the classification of each voxel into either the air or the water phase. This form of binary classification is applied to the reconstruction by the *SIRT+dT* algorithm, since it performed best in time-resolved reconstruction based on NRMSE. The threshold is chosen such that the mean holdup after binary classification is equal to the mean holdup of the ground truth. This crossover threshold is chosen since the mean holdup can be determined experimentally using various alternate methods aside from CT. After applying the holdup crossover threshold to the reconstruction, the same operation is applied to the ground truth density field using the threshold of average density of the two phases. A confusion matrix is constructed to quantify the error in the classification of the reconstruction (table 4.3). For the purpose of deriving the performance metrics of the binary classifier, the air phase is considered ‘true’ and the water phase is considered ‘false’.

Table 4.3: Confusion matrix from binary classifier using density threshold: 736 kg m^{-3}.

	Classified air	**Classified water**
Actual air	TP: 501,686	FN: 280,994
Actual water	FP: 280,044	TN: 39,503,724

Numerous performance measures and metrics are available for binary classifiers [100, 101].

Given that the prevalence of the air phase is two orders of magnitude smaller than that of the water phase, the relevant statistics are the True Positive Rate (TPR) or recall and the Positive Predictive Value (PPV) or precision of the binary classifier (equations (4.3) and (4.4)). The TPR gives the sensitivity of the classifier by showing what percentage of the air phase is correctly classified as air. The PPV shows the probability of a voxel actually being air, given that it was classified as such. A Prediction-Recall curve can be constructed by varying the threshold (figure 4.9). This is preferred over a Receiver Operating Characteristic curve due to the previously stated difference in prevalence of the phases. At the holdup crossover threshold, the TPR and PPV are 0.641 and 0.642 respectively. Based on these values, the F1-score can be calculated by taking the geometric mean of the TPR and PPV, resulting in a score of 0.641 at the chosen threshold level (equation (4.5)).

$$\mathrm{TPR} = \frac{\mathrm{TP}}{\mathrm{TP} + \mathrm{FN}} \tag{4.3}$$

$$\mathrm{PPV} = \frac{\mathrm{TP}}{\mathrm{TP} + \mathrm{FP}} \tag{4.4}$$

$$F_1 = 2\frac{\mathrm{TPR} \cdot \mathrm{PPV}}{\mathrm{TPR} + \mathrm{PPV}} \tag{4.5}$$

To quantify the performance of the binary classifier across all threshold, the Area Under Curve for the Prediction-Recall curve (AUCPR) can be computed [101], which results in a value of 0.664. This allows for comparison of the performance of binary classifiers irrespective of the chosen threshold value.

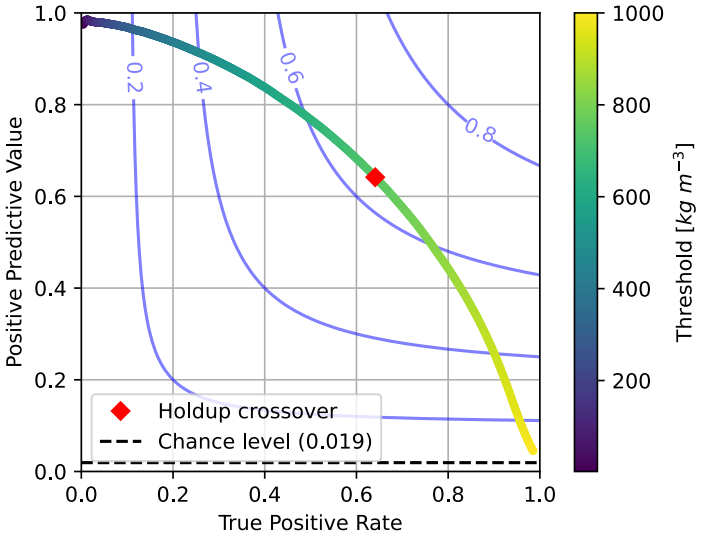

Figure 4.9: Precision-Recall curve over F1-score contours (blue). AUCPR: 0.664, F1-score: 0.641.

4.2.3. Number of angles

In view of exploring possible future upgrade paths for the TU Delft X-ray setup, the effect of adding two more projection angles for a total of five was studied for time-resolved reconstructions. Increasing the number of projection angles makes the linear system being solved less underdetermined and therefore less ill-posed. The projections were once again distributed

uniformly in the angular direction around the geometry origin. CT reconstructions of the bubble field were created using the best performing algorithms for the three angle case: *SIRT+dT* and *TVmin*.

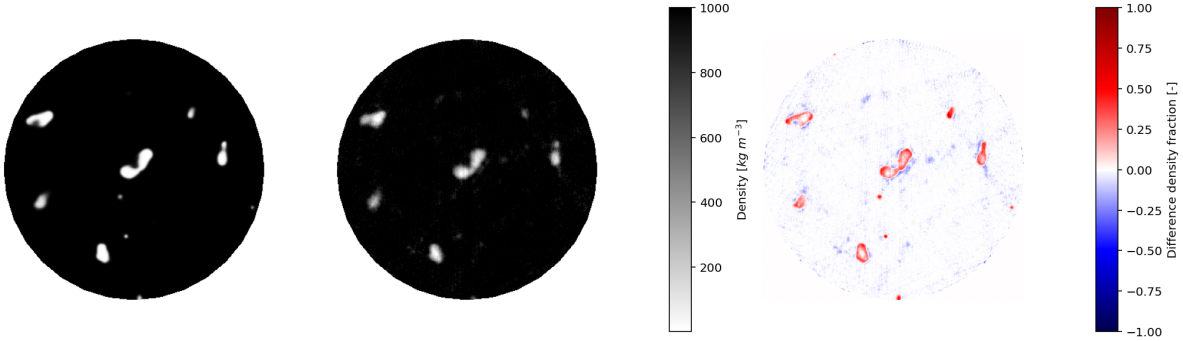

(a) Horizontal slice. Left to right: ground truth, reconstruction, difference.

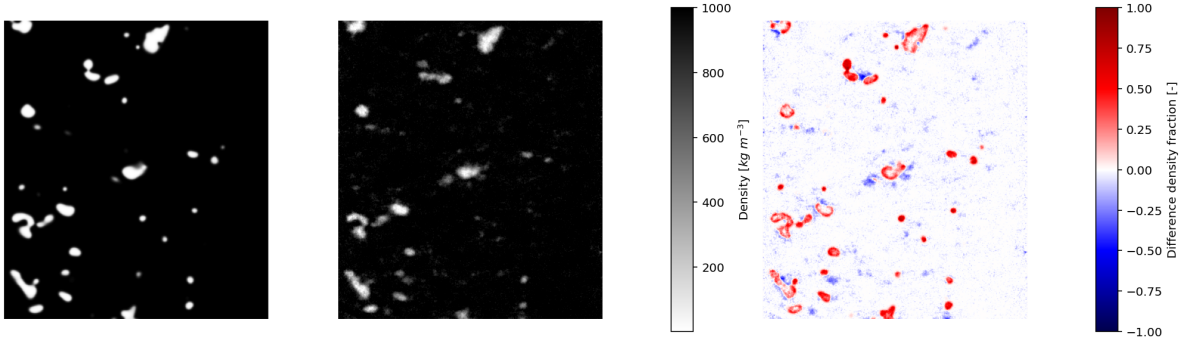

(b) Vertical slice. Left to right: ground truth, reconstruction, difference.

Figure 4.10: *SIRT+dT* reconstruction of the full-scale transient bubble field (case #3) at $t = 5.545\,\mathrm{s}$. Number of angles $= 5$, noise level $= 2\%$, $\alpha = 0.0008$, iterations $= 250$.

Comparing the five angle reconstruction to the three angle reconstruction both visually (figures 4.10 and 4.11) and by NRMSE (table 4.4), there is marked improvement for both methods. *SIRT+dT* does outperform *TVmin* once again. *TVmin* does still shows some significant streaking artefacts, while these are mostly absent from the *SIRT+dT* reconstructions. Both algorithms show significant reductions in the number of spurious bubbles.

The *SIRT+dT* reconstruction was once again used for binary classification using the same method used in section 4.2.2. The resulting confusion matrix and Precision-Recall curve are shown in table 4.5 and figure 4.12 respectively. The results from the five-angle case are compared to the three-angle case in table 4.6. A performance improvement is once again observed with both the F1-score and AUCPR increasing compared to the three-angle case.

These five-angle results indicates that upgrading the TU Delft setup with two additional projection angle would allow for a significant improvement in CT reconstructions. Within the current assumptions, this would allow for the correct classification of about 82% of the air-phase when using the F1-score as the metric. However, this is an optimistic estimate. The increase in scattering noise from the two additional X-ray sources would probably result in less improvement in practice. Furthermore, blurring optical effects such as motion blur and X-ray focus are currently not captured quantitively. Nonetheless, an improvement in CT reconstructions can still be expected despite these caveats.

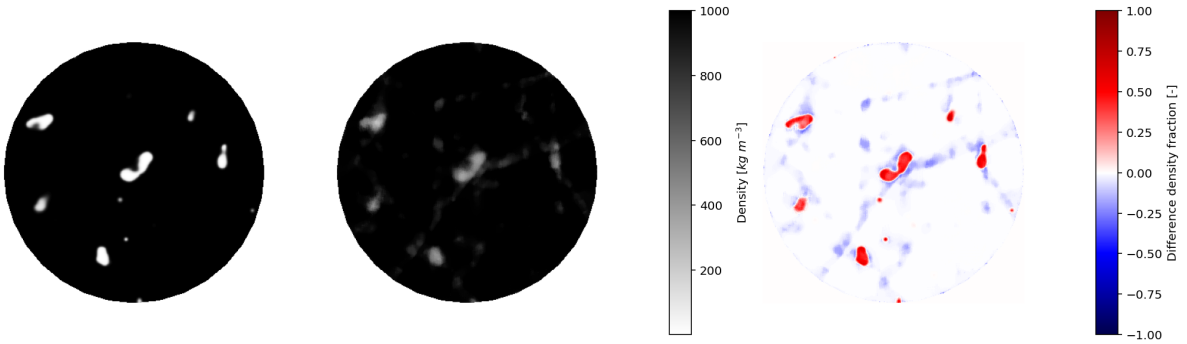

(a) Horizontal slice. Left to right: ground truth, reconstruction, difference.

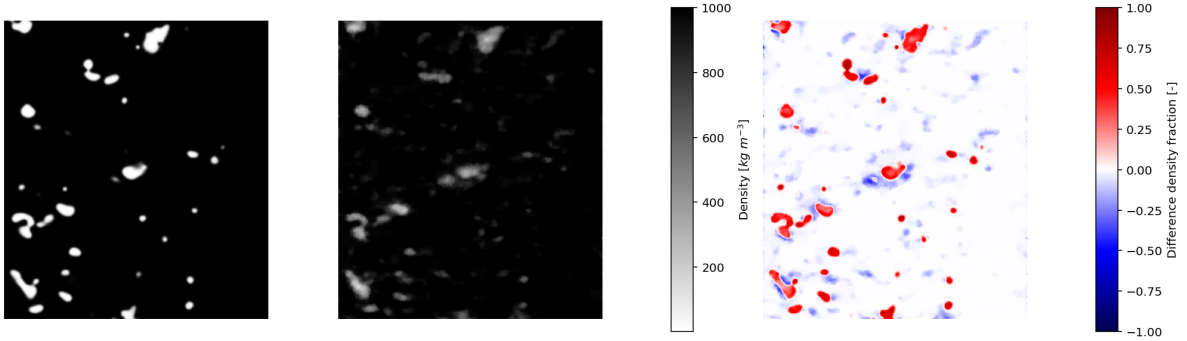

(b) Vertical slice. Left to right: ground truth, reconstruction, difference.

Figure 4.11: *TVmin* reconstruction of the full-scale transient bubble field (case #3) at $t = 5.545\,\mathrm{s}$. Number of angles $= 5$, noise level $= 2\%$, $\alpha = 0.15$, *SIRT+dT* pre-iterations $= 50$, iterations $= 1000$.

Table 4.4: Comparing the NRMSE of reconstruction for 3 and 5 projection angles: time-resolved full-scale (case #3).

Algorithm	Iterations	NRMSE		Change
		3 angles	5 angles	[%]
SIRT+dT	250	0.0867	0.0617	-28%
TVmin	1000	0.0955	0.0779	-18%

Table 4.5: Confusion matrix from binary classifier using density threshold: 696 kg m^{-3}.

	Classified air	Classified water
Actual air	TP: 643,703	FN: 138,977
Actual water	FP: 138,282	TN: 39,645,486

Table 4.6: Change in performance metrics of binary classifier between the five- and three-angle cases.

Number of angles	TPR	PPV	F1-score	AUCPR
3	0.641	0.642	0.641	0.664
5	0.822	0.823	0.823	0.864
Change [%]	+28%	+28%	+28%	+30%

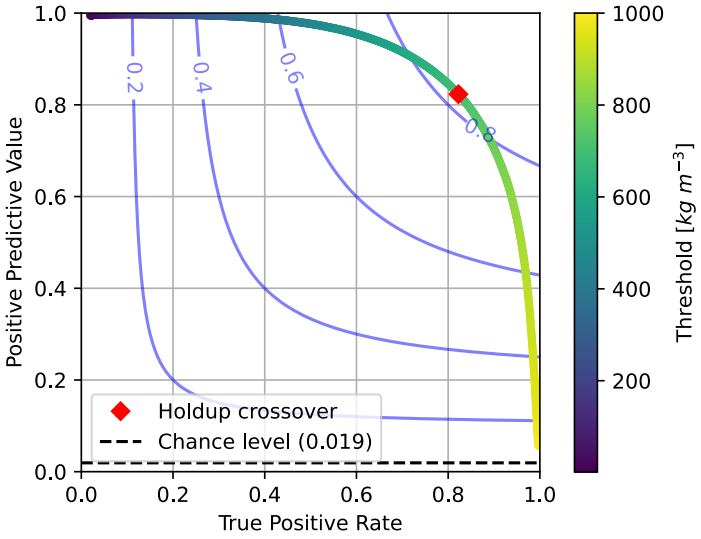

Figure 4.12: Precision-Recall curve over F1-score contours (blue) for 5 angle case. AUCPR: 0.864, F1-score: 0.823.

4.2.4. Time-averaged bubble fields

Applying the reconstruction algorithms to time-averaged data once again requires setting the regularisation constant α. The *TVmin* algorithm will not be applied to time-averaged reconstructions, since the edge-preserving features of this algorithm are not advantageous for smoother time-averaged datasets. The values of α of 0.00035 for *SIRT+sT* and 0.00085 for *SIRT+dT* were found using trial and error to minimise the NRMSE for a noise level of 2% applied to each time step individually. Assuming that the noise is uncorrelated, the averaged noise level $\overline{\mathrm{NL}}$ can be approximated using equation (4.6) based on the noise level applied to each time step NL_s and the number of time steps averaged N_s.

$$\overline{\mathrm{NL}} = \frac{\mathrm{NL}_s}{\sqrt{N_s}} \tag{4.6}$$

All reconstruction methods show an improvement for the time-resolved data over the time averaged data. As with the time-resolved reconstructions, the *SIRT+sT* reconstruction (figure 4.13) does not perform particularly well, showing strong streaking artefacts, salt and pepper noise and a general underestimation of the reconstructed density. The *SIRT+dT* reconstruction shows little to no salt and pepper noise as well as a significant reduction in the streaking artefacts shows in the horizontal slice. The *SIRT+dT* algorithm once again benefits from the relative smoothness of the underlying data. However, the current time-averaged data still shows individual bubble structures due. Increasing the time range over which the data is averaged would likely allow for higher regularisation parameter.

The poor performance of the *SIRT+sT* method can once again be explained by the central tendency to zero of the regularisation, which is not appropriate given the distribution of the underlying data. However, plotting the underlying data as a histogram shows that the time-averaged data does have a central tendency around the mean holdup (figure 4.15). Using this knowledge, the minimisation problem can be modified to move the central tendency of the regularisation terms to the mean holdup value and a new iterative method can be formulated using the regularisation offset β (equations (4.7) and (4.8)).

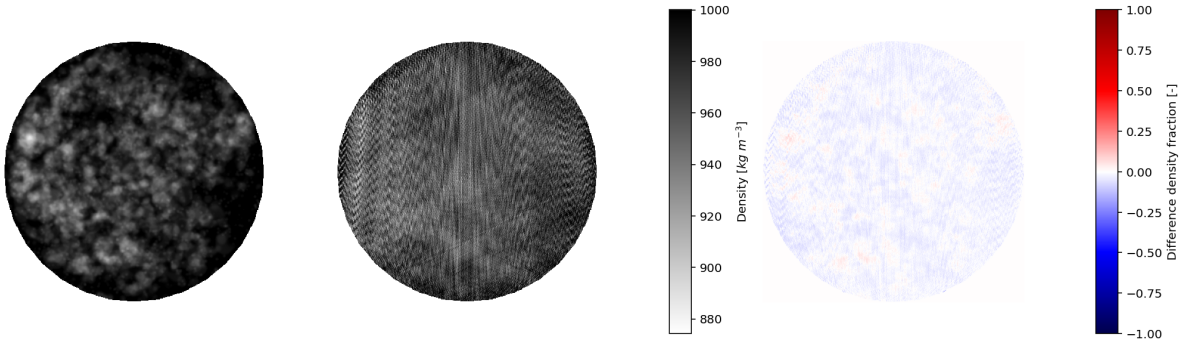

(a) Horizontal slice. Left to right: ground truth, reconstruction, difference.

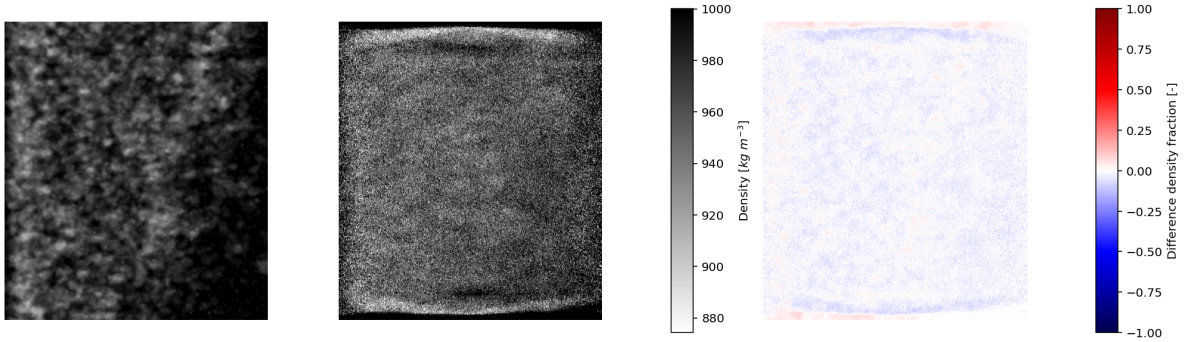

(b) Vertical slice. Left to right: ground truth, reconstruction, difference.

Figure 4.13: *SIRT+sT* reconstruction of the full-scale time-averaged bubble field (case #3) over $5\,\mathrm{s} \leq t \leq 10\,\mathrm{s}$. Number of angles $= 3$, averaged noise level $= 0.19\%$, $\alpha = 0.00035$, iterations $= 250$.

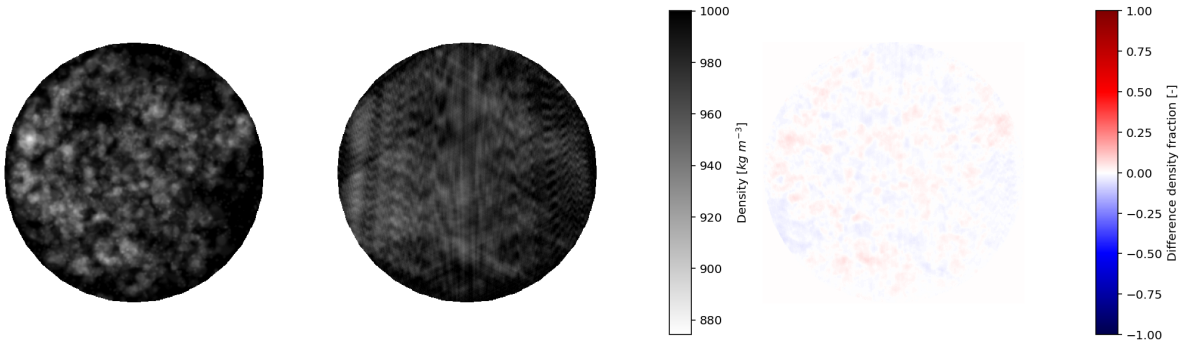

(a) Horizontal slice. Left to right: ground truth, reconstruction, difference.

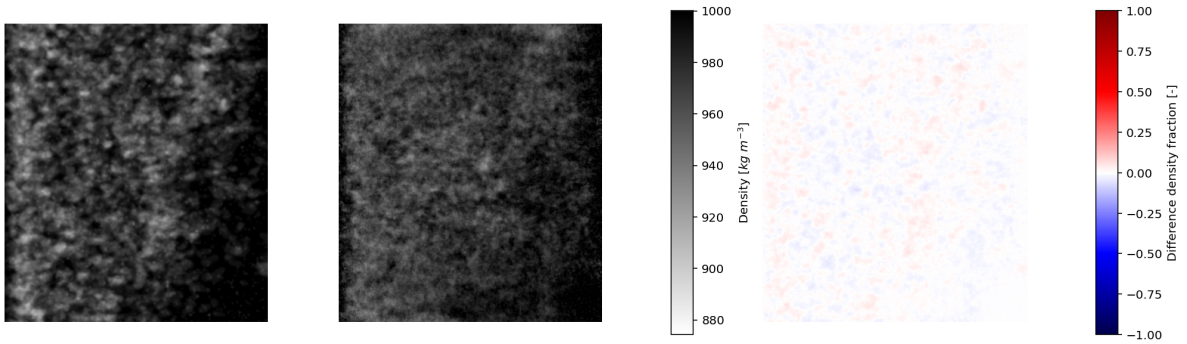

(b) Vertical slice. Left to right: ground truth, reconstruction, difference.

Figure 4.14: *SIRT+dT* reconstruction of the full-scale time-averaged bubble field (case #3) over $5\,\mathrm{s} \leq t \leq 10\,\mathrm{s}$. Number of angles $= 3$, averaged noise level $= 0.19\%$, $\alpha = 0.00085$, iterations $= 250$.

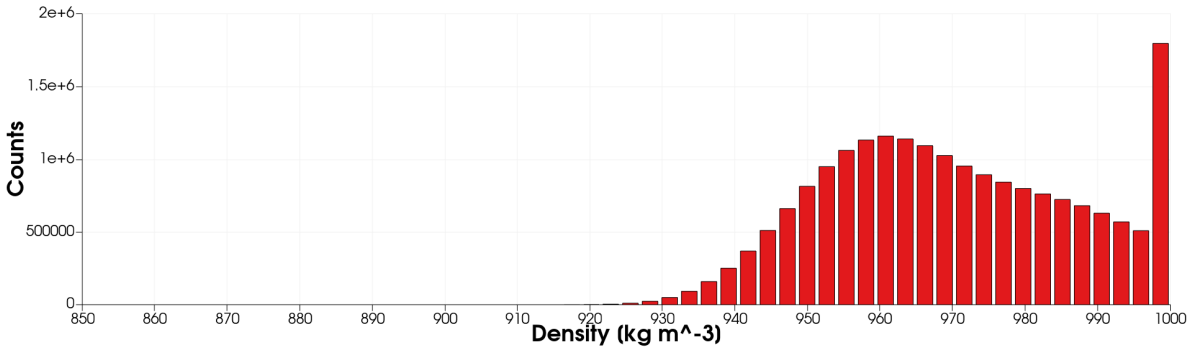

Figure 4.15: Distribution of the density (case #3) above 850 kg m^{-3} for the time-averaged data over $5\,\mathrm{s} \leq t \leq 10\,\mathrm{s}$ (for time-resolved, see appendix D: figure D.3).

$$\arg\min_{\boldsymbol{x}} \left\| \begin{pmatrix} \boldsymbol{A} \\ \sqrt{\alpha}\boldsymbol{I} \end{pmatrix} \boldsymbol{x} - \begin{pmatrix} \boldsymbol{b} \\ \beta \boldsymbol{1} \end{pmatrix} \right\|_2^2 \tag{4.7}$$

$$\boldsymbol{x}^{(k+1)} = P_B \left[\boldsymbol{x}^{(k)} + \lambda \boldsymbol{C} \boldsymbol{A}^T \boldsymbol{R} \left(\boldsymbol{b} - \boldsymbol{A}\boldsymbol{x}^{(k)} \right) - \alpha\lambda \boldsymbol{C} \left(\boldsymbol{x}^{(k)} - \beta \right) \right] \tag{4.8}$$

Using this new reconstruction algorithm *SIRT+sT Offset*, the reconstruction shows no more salt and pepper noise as the regularisation parameter can now be set higher without leading to a global underestimation of the density. Additionally, the streaking artefacts observed in the horizontal slice of both the standard *SIRT+sT* and *SIRT+dT* are absent.

Using the NRMSE of reconstruction (table 4.7), the *SIRT+sT* algorithm is shown to underperform the baseline SIRT algorithm, with an error more than twice as high. The *SIRT+dT* provide an improvement over the baseline. The *SIRT+sT Offset* outperforms both the baseline and *SIRT+dT*. Considering applicability on experimental data, both the *SIRT+dT* and *SIRT+sT Offset* provide better reconstructions than the baseline. While *SIRT+sT Offset* outperforms *SIRT+dT*, it does require the additional step of determining the mean holdup beforehand. Besides, as shown in figure 4.15, the distribution of densities of the time-averaged data is not normal. Therefore, other measures for central tendency such as median or mode may produce better results, though these measures are not measurable using alternate experimental techniques like fibre-optic or pressure probe.

Table 4.7: NRMSE of reconstruction: time-averaged full-scale (case #3).

Algorithm	**Iterations**	**NRMSE**	**Change** [%]
SIRT (DP)	17	0.0160	baseline
SIRT+sT	250	0.0340	+113%
SIRT+dT	250	0.0144	-10%
SIRT+sT Offset	250	0.0137	-14%

4.2.5. Axisymmetric reconstructions

Previous research using CT reconstruction of cylindrical bubble columns have shown that the time-averaged hold-up profile is axisymmetric around the centre point [21, 95]. This assumption can be imposed on the CT reconstructions by averaging three time-averaged projections and their mirror images mirrored along the axial direction. The resulting averaged projection

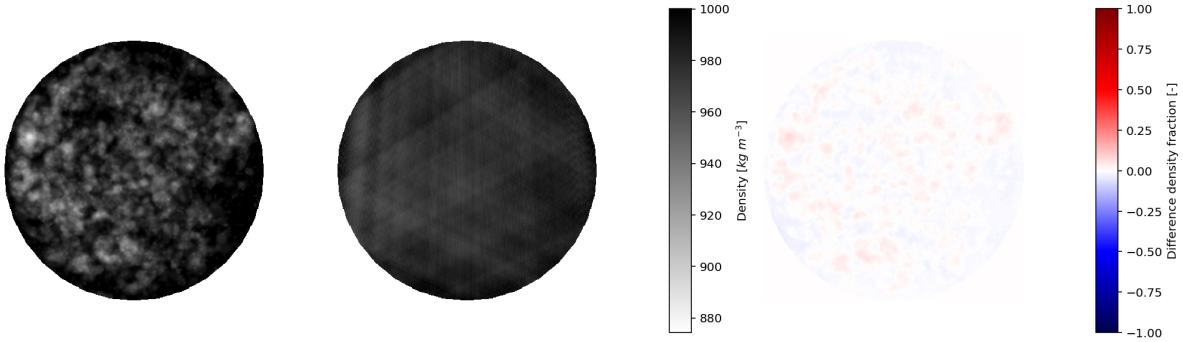

(a) Horizontal slice. Left to right: ground truth, reconstruction, difference.

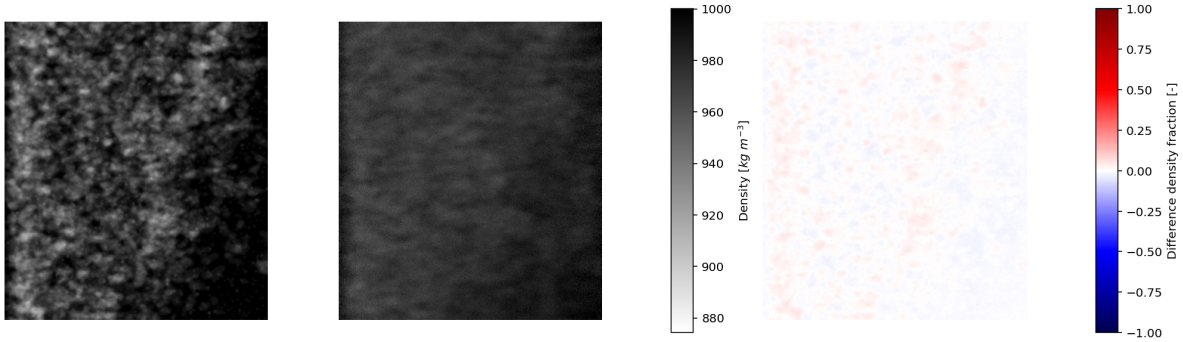

(b) Vertical slice. Left to right: ground truth, reconstruction, difference.

Figure 4.16: *SIRT+sT Offset* reconstruction of the full-scale time-averaged bubble field (case #3) over $5\,\mathrm{s} \leq T \leq 10\,\mathrm{s}$. Number of angles $= 3$, averaged noise level $= 0.19\%$, $\alpha = 0.004$, $\beta = 978\,\mathrm{kg\,m^{-3}}$ iterations $= 250$.

can turned into a sinogram with identical projections along an arbitrary number of angles. Using this sinogram for reconstruction results in an axisymmetric profile. The half-scale column in the bubbly regime (case #1) will be used for these reconstructions, since the flow in the full-scale column simulation is not axisymmetric as shown in section 4.1.1 due to the issues with the inlet resolution. The *SIRT+dT* algorithm was used for the reconstructions, with a regularisation parameter of 0.10 and 0.00085 for the reconstruction with and without the axisymmetric assumptions respectively.

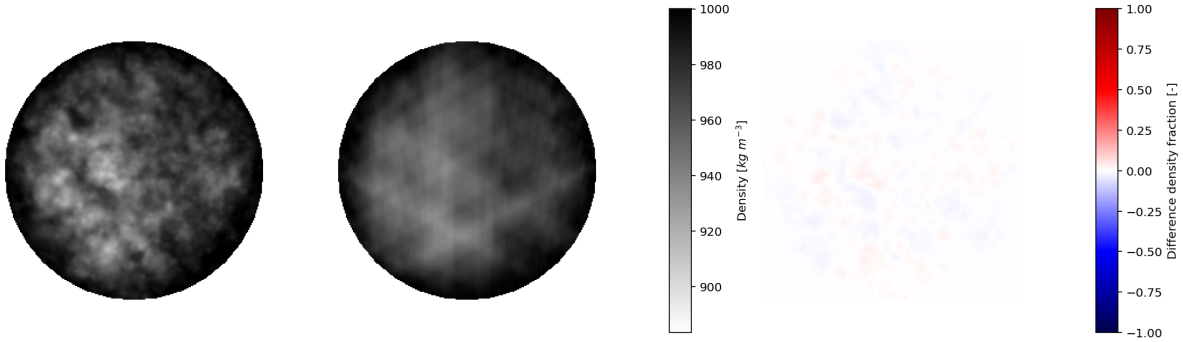

(a) Horizontal slice without axisymmetric assumption. Left to right: ground truth, reconstruction, difference. Number of angles $= 3$, $\alpha = 0.00085$.

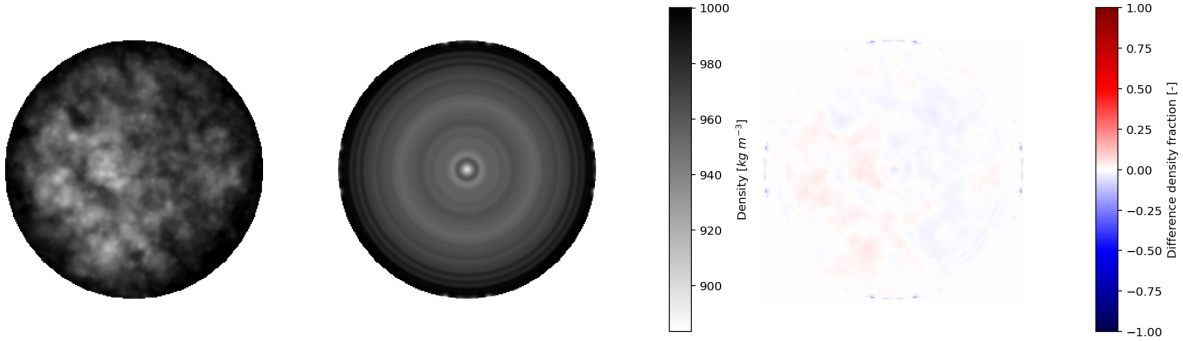

(b) Horizontal slice with axisymmetric assumption. Left to right: ground truth, reconstruction, difference. Number of angles $= 379$, $\alpha = 0.10$.

Figure 4.17: *SIRT+dT* reconstruction of the half-scale time-averaged bubble field (case #1) over $5\,\mathrm{s} < T \leq 15\,\mathrm{s}$. Averaged noise level $= 0.19\%$, iterations $= 250$.

Comparing the reconstructions with and without the axisymmetric assumption (figure 4.17), the effect of the assumption is clearly shown by the concentric rings artefacts. The difference in reconstruction quality is difficult to judge visually. Comparison of the NRMSE shows that the axisymmetric reconstruction has a 22% higher error than the non-axisymmetric reconstruction. The higher error in the axisymmetric reconstruction indicates that the assumption of axisymmetry may not be valid for this system (table 4.8).

In order to determine the degree of axisymmetry, the ground truth and both reconstructions are binned by radial distance. The variance with each of these radial bins is calculated and the resulting variances are averaged. This ‘axial variance’ can be plotted against the number of averaged time steps to determine how many time steps must be averaged in order to assume axisymmetry of the holdup profile (figure 4.18). The resulting plot shows a linear decrease in the axial variance when plotted on a log-log scale. The point were the axial variances overlap can therefore be extrapolated using linear regression. The axial variance of the regular time-averaged reconstruction is expected to reach parity with the axial variance of the axisymmetric reconstruction after averaging data over 30 seconds. For the axial variance of the ground truth

to reach parity with the axisymmetric reconstruction, bubble column data must be averaged over 60 seconds. Note that the axial variance partially depends on the number of bins N_{bins} used when it is calculated as some of the variance arises from the radial direction. Therefore, these time frames apply when a radial resolution of 50 is required. Based on these results, guidelines can be formulated as to when axisymmetric reconstructions are suitable to the underlying data. This comparison between the regular and axisymmetric reconstructions can also be performed without the need for a ground truth.

Asymmetric reconstructions may be able to produce better reconstructions over longer measurement times. However, over shorter measurement times, they provide little no benefit in term of error and only hide the non-axisymmetric perturbations of the hold-up profile which occur over shorter time scales.

Table 4.8: NRMSE of reconstruction: axisymmetric half-scale (case #1).

Algorithm	Iterations	NRMSE
SIRT+dT	250	0.0124
SIRT+dT (axisymmetric)	250	0.0151

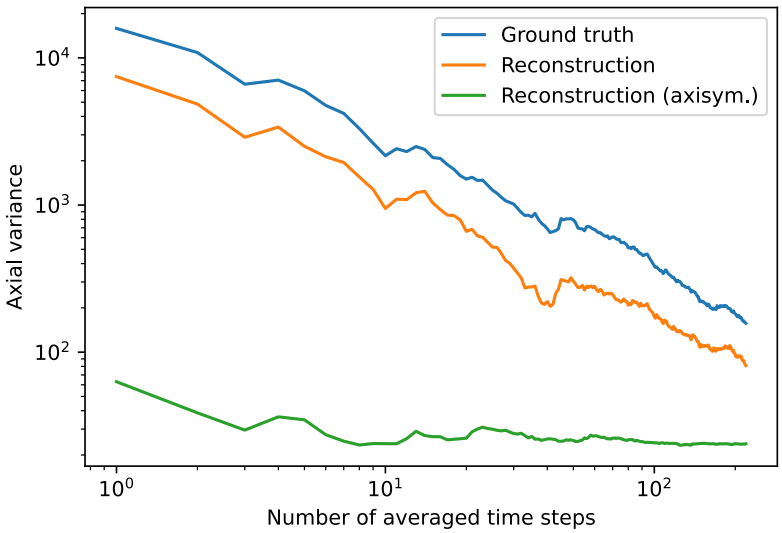

Figure 4.18: Axial variance over the number of averaged time steps. The crossover of ground truth and reconstruction (axisym) is linearly extrapolated to be after averaging 1289 time steps (58 s). The crossover of reconstruction and reconstruction (axisym) is extrapolated to be after averaging 647 time steps (29 s). $N_{bins} = 50$.

5

Conclusion & Future Research

This thesis sought to develop and validate a CFD model capable of reproducing the bubble field within the Volger column. Validation via comparison with the paper by Sanyal et al. [2] showed that half-scale simulations provide an accurate reproduction of the fluid behaviour in regards to holdup and mean velocity. The turbulent kinetic energy shows some deviation for the half-scale heterogeneous churn-turbulent regime, but this is hard to prove for sure without experimental data for this column geometry or comparison with data from case #4. The underresolved sparger inlets result in the mean velocity profile and the associated velocity field being invalid for the full-scale column data. This may be addressed by rerunning the simulation using either a higher resolution or an altered geometry (artificially increasing the sparger hole diameter) for which the greedy meshing algorithm provides less underresolved inlet geometries. The absence of the data for case #4 also limits model validation, though this simulation would suffer from the same underresolution of the inlets as in case #3. Despite these issues, the holdup and turbulent kinetic energy profiles are accurately captured in case #3.

Additional validation methods to be explored in the future include direct comparison of the mean hold-up to the experimental Volger column using pressure probes and comparison of the bubble size distribution using a fibre probe. Rather than using the bubble size distribution derived from fibre probe data, a direct comparison with the data measured by the fibre probe (bubble chord length and interface velocity) may be performed [19]. Overall, the validation of the CFD model shows the limitations of the current bubble column model. The current validation showed that the model does not accurately represent the experimental bubble column in full-scale simulations with regards to the velocity profile, although no severe ‘order of magnitude’ velocity deviations were observed. Despite this issue, the CFD results were still used for the validation of tomographic reconstruction techniques.

This thesis sought to quantify the accuracy and errors of limited-angle CT reconstructions of such a bubble field for both time-averaged and time-resolved data and explore methods of improving the accuracy of these CT reconstructions and give recommendations for future experimental CT setups and reconstruction methods. The error of various tomographic reconstruction techniques was compared to the baseline SIRT algorithm using the continuous Normalised Root Mean Squared Error (NRMSE). Additionally, for time-resolved bubble fields, the discrete performance statistics of PPV, TPR, F-score and AUCPR were determined for both three-angle and five-angle CT setups when using the *SIRT+dT* algorithm.

For time-resolved bubble fields, *SIRT+dT* and *TVmin* were shown to be an improvement over

the baseline SIRT reconstruction algorithm. *TVmin* is currently outperformed by *SIRT+dT* both in terms of error and number of iterations required for convergence. Moving to an alternate implementation could see the *TVmin* algorithm outperform *SIRT+dT*. An improved implementation may include proper boundary conditions with the non-fluid domain when minimising the total variation and a faster alternative to the Chambolle-Pock algorithm, such as a differentiable approximation of the total variation [72, pp. 306–311] [99].

Although these algorithms performed well for the current dataset, generalisation to the experimental setup is limited. Both due to the limitation in the CFD model as well limitations in simulating the source of error such as motion blur and a finite focal spot size. Future research could include quantifying the effects of motion blur on reconstruction, especially the anisotropic blurring effects and possible implementation anisotropic regularisation based on the *SIRT+dT* algorithm. There is also the LASSO reconstruction algorithm which produces sparse CT reconstructions and was not explored in this work [72, pp.263–265]. These sparse reconstructions may provide improved reconstructions over the baseline SIRT method, considering that the bubbles represent areas of almost zero density. Although the implementation of a LASSO solver may be comparable in complexity to the implementation of the *TVmin* solver based on the Chambolle-Pock algorithm [72, pp.303-304].

For time-averaged bubble fields, *SIRT+dT* and *SIRT+sT Offset* were shown to be an improvement over the baseline SIRT reconstruction algorithm. While *SIRT+sT Offset* outperforms *SIRT+dT*, it does require the offset parameter to be determined. Setting this parameter to the mean holdup was shown to be effective in reducing the reconstruction error significantly. Other measures of central tendency such as the mode or median were not explored since there are several methods of experimentally determining the mean holdup independently.

Applying the axisymmetric assumption may lead to improvement in the reconstructions. However, this depends on accumulating data over a sufficiently long time frame that the underlying holdup distribution is axisymmetric. Over shorter time frames axisymmetric reconstruction underperforms the regular time-averaged *SIRT+dT* reconstruction. However, the longer the time frame over which data is gathered, the more the underlying assumption of axisymmetry is valid. The axial variance between the regular reconstruction can be used as a proxy for the axial variance of the ground truth, although it underestimates the actual axial variance by about half.

In terms of recommendations, the *SIRT+dT* algorithm performs best overall for time-resolved reconstructions and second best for time-averaged reconstructions and is therefore the best all-round reconstruction algorithm. The *SIRT+sT Offset* can also be used for time-averaged reconstructions lest the mean holdup is known. It should be emphasised that the performance of the explored reconstruction algorithms relies on choosing the right regularisation parameter value. Although these values can be chosen based on visual inspection of the reconstructions, additional research on rigorous methods of choosing this parameter for these systems is required. In terms of future upgrades to the TU Delft X-ray setup, the addition of two additional source-detector pairs would significantly increase the accuracy of tomographic reconstruction.

References

[1] Lars Puiman et al. 'Alleviating mass transfer limitations in industrial external-loop syngas-to-ethanol fermentation'. In: *Chemical Engineering Science* 259 (Sept. 21, 2022), p. 117770. ISSN: 0009-2509. DOI: 10.1016/j.ces.2022.117770. URL: https://www.sciencedirect.com/science/article/pii/S0009250922003542 (visited on 05/09/2025).

[2] Jayanta Sanyal et al. 'Numerical simulation of gas–liquid dynamics in cylindrical bubble column reactors'. In: *Chemical Engineering Science* 54.21 (Nov. 1, 1999), pp. 5071–5083. ISSN: 0009-2509. DOI: 10.1016/S0009-2509(99)00235-3. URL: https://www.sciencedirect.com/science/article/pii/S0009250999002353 (visited on 09/02/2024).

[3] Biotechnology Innovation Organization. 'Advancing the Biobased Economy: Renewable Chemical Biorefinery Commercialization, Progress, and Market Opportunities, 2016 and Beyond'. In: *Industrial Biotechnology* 12.5 (Oct. 2016), pp. 290–294. ISSN: 1550-9087. DOI: 10.1089/ind.2016.29050.pwi. URL: https://www.liebertpub.com/doi/full/10.1089/ind.2016.29050.pwi (visited on 09/27/2024).

[4] Gabriel Lopez et al. 'From fossil to green chemicals: sustainable pathways and new carbon feedstocks for the global chemical industry'. In: *Energy & Environmental Science* 16.7 (2023), pp. 2879–2909. DOI: 10.1039/D3EE00478C. URL: https://pubs.rsc.org/en/content/articlelanding/2023/ee/d3ee00478c (visited on 09/27/2024).

[5] I. Katharina Stoll, Nikolaos Boukis, and Jörg Sauer. 'Syngas Fermentation to Alcohols: Reactor Technology and Application Perspective'. In: *Chemie Ingenieur Technik* 92.1 (2020), pp. 125–136. ISSN: 1522-2640. DOI: 10.1002/cite.201900118. URL: https://onlinelibrary.wiley.com/doi/abs/10.1002/cite.201900118 (visited on 05/09/2025).

[6] JoséC. Merchuk, Sigal Ben-Zvi (Yona), and Keshavan Niranjan. 'Why use bubble-column bioreactors?' In: *Trends in Biotechnology* 12.12 (Dec. 1, 1994), pp. 501–511. ISSN: 0167-7799. DOI: 10.1016/0167-7799(94)90058-2. URL: https://www.sciencedirect.com/science/article/pii/0167779994900582 (visited on 05/08/2025).

[7] D. Humbird, R. Davis, and J. D. McMillan. 'Aeration costs in stirred-tank and bubble column bioreactors'. In: *Biochemical Engineering Journal* 127 (Nov. 15, 2017), pp. 161–166. ISSN: 1369-703X. DOI: 10.1016/j.bej.2017.08.006. URL: https://www.sciencedirect.com/science/article/pii/S1369703X17302103 (visited on 09/27/2024).

[8] Y. T. Shah et al. 'Design parameters estimations for bubble column reactors'. In: *AIChE Journal* 28.3 (1982), pp. 353–379. ISSN: 1547-5905. DOI: 10.1002/aic.690280302. URL: https://onlinelibrary.wiley.com/doi/abs/10.1002/aic.690280302 (visited on 05/09/2025).

[9] J. J. Heijnen and K. Van't Riet. 'Mass transfer, mixing and heat transfer phenomena in low viscosity bubble column reactors'. In: *The Chemical Engineering Journal* 28.2 (Apr. 1, 1984), B21–B42. ISSN: 0300-9467. DOI: 10.1016/0300-9467(84)85025-X. URL: https://www.sciencedirect.com/science/article/pii/030094678485025X (visited on 05/09/2025).

[10] M. R. Bhole, J. B. Joshi, and D. Ramkrishna. 'CFD simulation of bubble columns incorporating population balance modeling'. In: *Chemical Engineering Science* 63.8 (Apr. 1, 2008), pp. 2267–2282. ISSN: 0009-2509. DOI: 10.1016/j.ces.2008.01.013. URL: https://www.sciencedirect.com/science/article/pii/S0009250908000298 (visited on 05/09/2025).

[11] Giorgio Besagni, Nicolò Varallo, and Riccardo Mereu. 'Computational Fluid Dynamics Modelling of Two-Phase Bubble Columns: A Comprehensive Review'. In: *Fluids* 8.3 (Mar. 2023), p. 91. ISSN: 2311-5521. DOI: 10.3390/fluids8030091. URL: https://www.mdpi.com/2311-5521/8/3/91 (visited on 09/10/2024).

[12] Dale D. McClure et al. 'Towards a CFD model of bubble columns containing significant surfactant levels'. In: *Chemical Engineering Science* 127 (May 4, 2015), pp. 189–201. ISSN: 0009-2509. DOI: 10.1016/j.ces.2015.01.025. URL: https://www.sciencedirect.com/science/article/pii/S0009250915000457 (visited on 05/09/2025).

[13] G. Marrucci. 'A theory of coalescence'. In: *Chemical Engineering Science* 24.6 (June 1, 1969), pp. 975–985. ISSN: 0009-2509. DOI: 10.1016/0009-2509(69)87006-5. URL: https://www.sciencedirect.com/science/article/pii/0009250969870065 (visited on 10/30/2024).

[14] Timothy T. Duignan. 'The surface potential explains ion specific bubble coalescence inhibition'. In: *Journal of Colloid and Interface Science* 600 (Oct. 15, 2021), pp. 338–343. ISSN: 0021-9797. DOI: 10.1016/j.jcis.2021.04.144. URL: https://www.sciencedirect.com/science/article/pii/S002197972100669X (visited on 11/01/2024).

[15] R. Volger, L. Puiman, and C. Haringa. 'Bubbles and Broth: A review on the impact of broth composition on bubble column bioreactor hydrodynamics'. In: *Biochemical Engineering Journal* 201 (Jan. 1, 2024), p. 109124. ISSN: 1369-703X. DOI: 10.1016/j.bej.2023.109124. URL: https://www.sciencedirect.com/science/article/pii/S1369703X23003194 (visited on 09/02/2024).

[16] L. Rueda Villegas et al. 'Image processing for the experimental investigation of dense dispersed flows: Application to bubbly flows'. In: *International Journal of Multiphase Flow* 111 (Feb. 1, 2019), pp. 16–30. ISSN: 0301-9322. DOI: 10.1016/j.ijmultiphaseflow.2018.10.017. URL: https://www.sciencedirect.com/science/article/pii/S0301932218302350 (visited on 03/18/2025).

[17] Yannic Mast and Ralf Takors. 'Novel experimental data-driven bubble breakage model for universal application in Euler-Lagrange multiphase frameworks'. In: *Chemical Engineering Science* 284 (Feb. 5, 2024), p. 119509. ISSN: 0009-2509. DOI: 10.1016/j.ces.2023.119509. URL: https://www.sciencedirect.com/science/article/pii/S0009250923010655 (visited on 09/26/2024).

[18] H. Hikita et al. 'Gas hold-up in bubble columns'. In: *The Chemical Engineering Journal*. An International Journal of Research and Development 20.1 (Jan. 1, 1980), pp. 59–67. ISSN: 0300-9467. DOI: 10.1016/0300-9467(80)85006-4. URL: https://www.sciencedirect.com/science/article/pii/0300946780850064 (visited on 05/09/2025).

[19] Anthony Lefebvre et al. 'A new, optimized Doppler optical probe for phase detection, bubble velocity and size measurements: Investigation of a bubble column operated in the heterogeneous regime'. In: *Chemical Engineering Science* 250 (Mar. 15, 2022), p. 117359. ISSN: 0009-2509. DOI: 10.1016/j.ces.2021.117359. URL: https://www.sciencedirect.com/science/article/pii/S0009250921009246 (visited on 04/02/2025).

[20] Thorsten M. Buzug. *Computed Tomography: From Photon Statistics to Modern Cone-Beam CT*. Springer, June 13, 2008. 521 pp. ISBN: 978-3-540-39407-5.

[21] Jeremy L. Hubers et al. 'X-ray computed tomography in large bubble columns'. In: *Chemical Engineering Science*. 7th International Conference on Gas-Liquid and Gas-Liquid-Solid Reactor Engineering 60.22 (Nov. 1, 2005), pp. 6124–6133. ISSN: 0009-2509. DOI: 10.1016/j.ces.2005.03.038. URL: https://www.sciencedirect.com/science/article/pii/S0009250905002794 (visited on 09/19/2024).

[22] Theodore J. Heindel. 'A Review of X-Ray Flow Visualization With Applications to Multiphase Flows'. In: *Journal of Fluids Engineering* 133.74001 (July 22, 2011). ISSN: 0098-2202. DOI: 10.1115/1.4004367. URL: https://doi.org/10.1115/1.4004367 (visited on 05/09/2025).

[23] Narasimhan Devanathan. 'Investigation of liquid hydrodynamics in bubble columns via a computer automated radioactive particle tracking (CARPT) facility'. D.Sc. thesis. Saint Louis, Missouri, USA: Washington University, May 1991. URL: https://www.proquest.com/openview/d60991a481a11a07f541974916b054aa.

[24] Sujatha Degaleesan. 'Fluid dynamic measurements and modeling of liquid mixing in bubble columns'. D.Sc. thesis. Saint Louis, Missouri, USA: Washington University, Aug. 1997. URL: https://www.proquest.com/openview/24fbad1807f412bb907163d091b9cc7c.

[25] Adriaan B.M. Graas et al. 'X-ray tomography for fully-3D time-resolved reconstruction of bubbling fluidized beds'. In: *Powder Technology* 434 (Feb. 2024), p. 119269. ISSN: 00325910. DOI: 10.1016/j.powtec.2023.119269. URL: https://linkinghub.elsevier.com/retrieve/pii/S0032591023010525 (visited on 09/02/2024).

[26] Sergiu Klainerman and Andrew Majda. 'Singular limits of quasilinear hyperbolic systems with large parameters and the incompressible limit of compressible fluids'. In: *Communications on Pure and Applied Mathematics* 34.4 (1981), pp. 481–524. ISSN: 1097-0312. DOI: 10.1002/cpa.3160340405. URL: https://onlinelibrary.wiley.com/doi/abs/10.1002/cpa.3160340405 (visited on 01/28/2025).

[27] Steven Schochet. 'The mathematical theory of low Mach number flows'. In: *ESAIM: Mathematical Modelling and Numerical Analysis* 39.3 (May 1, 2005), pp. 441–458. ISSN: 0764-583X, 1290-3841. DOI: 10.1051/m2an:2005017. URL: https://www.esaim-m2an.org/articles/m2an/abs/2005/03/m2an01EDP/m2an01EDP.html (visited on 01/28/2025).

[28] Timm Krüger et al. *The Lattice Boltzmann Method: Principles and Practice*. Graduate Texts in Physics. Cham: Springer International Publishing, 2017. ISBN: 978-3-319-44649-3. DOI: 10.1007/978-3-319-44649-3. URL: http://link.springer.com/10.1007/978-3-319-44649-3 (visited on 02/06/2025).

[29] Sydney Chapman and T. G. Cowling. *The Mathematical Theory of Non-uniform Gases: An Account of the Kinetic Theory of Viscosity, Thermal Conduction and Diffusion in Gases*. Cambridge University Press, 1990. 452 pp. ISBN: 978-0-521-40844-8.

[30] Yos Panagaman Sitompul and Takayuki Aoki. 'A filtered cumulant lattice Boltzmann method for violent two-phase flows'. In: *Journal of Computational Physics* 390 (Aug. 1, 2019), pp. 93–120. ISSN: 0021-9991. DOI: 10.1016/j.jcp.2019.04.019. URL: https://www.sciencedirect.com/science/article/pii/S0021999119302529 (visited on 09/12/2024).

[31] Pao-Hsiung Chiu and Yan-Ting Lin. 'A conservative phase field method for solving incompressible two-phase flows'. In: *Journal of Computational Physics* 230.1 (Jan. 1, 2011), pp. 185–204. ISSN: 0021-9991. DOI: 10.1016/j.jcp.2010.09.021. URL: https://www.sciencedirect.com/science/article/pii/S0021999110005243 (visited on 03/12/2025).

[32] Martin Geier, Abbas Fakhari, and Taehun Lee. 'Conservative phase-field lattice Boltzmann model for interface tracking equation'. In: *Physical Review E* 91.6 (June 17, 2015), p. 063309. DOI: 10.1103/PhysRevE.91.063309. URL: https://link.aps.org/doi/10.1103/PhysRevE.91.063309 (visited on 02/06/2025).

[33] J. U Brackbill, D. B Kothe, and C Zemach. 'A continuum method for modeling surface tension'. In: *Journal of Computational Physics* 100.2 (June 1, 1992), pp. 335–354. ISSN: 0021-9991. DOI: 10.1016/0021-9991(92)90240-Y. URL: https://www.sciencedirect.com/science/article/pii/002199919290240Y (visited on 03/12/2025).

[34] *M-Star CFD documentation*. URL: https://docs.mstarcfd.com/index.html (visited on 10/31/2024).

[35] Martin Geier, Andrea Pasquali, and Martin Schönherr. 'Parametrization of the cumulant lattice Boltzmann method for fourth order accurate diffusion part I: Derivation and validation'. In: *Journal of Computational Physics* 348 (Nov. 1, 2017), pp. 862–888. ISSN: 0021-9991. DOI: 10.1016/j.jcp.2017.05.040. URL: https://www.sciencedirect.com/science/article/pii/S0021999117304230 (visited on 11/28/2024).

[36] Martin Geier et al. 'Under-resolved and large eddy simulations of a decaying Taylor–Green vortex with the cumulant lattice Boltzmann method'. In: *Theoretical and Computational Fluid Dynamics* 35.2 (Apr. 1, 2021), pp. 169–208. ISSN: 1432-2250. DOI: 10.1007/s00162-020-00555-7. URL: https://doi.org/10.1007/s00162-020-00555-7 (visited on 11/28/2024).

[37] Y. Ling, S. Zaleski, and R. Scardovelli. 'Multiscale simulation of atomization with small droplets represented by a Lagrangian point-particle model'. In: *International Journal of Multiphase Flow* 76 (Nov. 1, 2015), pp. 122–143. ISSN: 0301-9322. DOI: 10.1016/j.ijmultiphaseflow.2015.07.002. URL: https://www.sciencedirect.com/science/article/pii/S0301932215001524 (visited on 11/18/2024).

[38] Alfred Barnard Basset and John William Strutt. 'III. On the motion of a sphere in a viscous liquid'. In: *Philosophical Transactions of the Royal Society of London. (A.)* 179 (Jan. 1997), pp. 43–63. DOI: 10.1098/rsta.1888.0003. URL: https://royalsocietypublishing.org/doi/abs/10.1098/rsta.1888.0003 (visited on 01/31/2025).

[39] Martin Sommerfeld. *Best Practice Guidelines for Computational Fluid Dynamics of Dispersed Multiphase Flows*. ERCOFTAC, 2008. 129 pp. ISBN: 978-91-633-3564-8.

[40] Marcelo Muniz and Martin Sommerfeld. 'On the force competition in bubble columns: A numerical study'. In: *International Journal of Multiphase Flow* 128 (July 1, 2020), p. 103256. ISSN: 0301-9322. DOI: 10.1016/j.ijmultiphaseflow.2020.103256. URL: https://www.sciencedirect.com/science/article/pii/S030193221930535X (visited on 01/31/2025).

[41] Fuat Odar and Wallis S. Hamilton. 'Forces on a sphere accelerating in a viscous fluid'. In: *Journal of Fluid Mechanics* 18.2 (Feb. 1964), pp. 302–314. ISSN: 1469-7645, 0022-1120. DOI: 10.1017/S0022112064000210. URL: https://www.cambridge.org/core/journals/journal-of-fluid-mechanics/article/abs/forces-on-a-sphere-

accelerating-in-a-viscous-fluid/E7F0995E5C488E2014BFB2A4683331DE (visited on 01/28/2025).

[42] Fuat Odar. 'Verification of the proposed equation for calculation of the forces on a sphere accelerating in a viscous fluid'. In: *Journal of Fluid Mechanics* 25.3 (July 1966), pp. 591–592. ISSN: 1469-7645, 0022-1120. DOI: 10.1017/S0022112066000272. URL: https://www.cambridge.org/core/journals/journal-of-fluid-mechanics/article/verification-of-the-proposed-equation-for-calculation-of-the-forces-on-a-sphere-accelerating-in-a-viscous-fluid/90B5059F252FB43466512822A06EE40D# (visited on 10/09/2024).

[43] Phillip P. Brown and Desmond F. Lawler. 'Sphere Drag and Settling Velocity Revisited'. In: *Journal of Environmental Engineering* 129.3 (Mar. 1, 2003), pp. 222–231. ISSN: 0733-9372. DOI: 10.1061/(ASCE)0733-9372(2003)129:3(222). URL: https://ascelibrary.org/doi/10.1061/%28ASCE%290733-9372%282003%29129%3A3%28222%29 (visited on 10/08/2024).

[44] Akio Tomiyama et al. 'Drag Coefficients of Single Bubbles under Normal and Micro Gravity Conditions'. In: *JSME International Journal Series B* 41.2 (1998), pp. 472–479. DOI: 10.1299/jsmeb.41.472.

[45] R Krishna et al. 'Rise velocity of a swarm of large gas bubbles in liquids'. In: *Chemical Engineering Science* 54.2 (Jan. 1, 1999), pp. 171–183. ISSN: 0009-2509. DOI: 10.1016/S0009-2509(98)00245-0. URL: https://www.sciencedirect.com/science/article/pii/S0009250998002450 (visited on 05/14/2025).

[46] I. Roghair et al. 'On the drag force of bubbles in bubble swarms at intermediate and high Reynolds numbers'. In: *Chemical Engineering Science*. 10th International Conference on Gas–Liquid and Gas–Liquid–Solid Reactor Engineering 66.14 (July 15, 2011), pp. 3204–3211. ISSN: 0009-2509. DOI: 10.1016/j.ces.2011.02.030. URL: https://www.sciencedirect.com/science/article/pii/S0009250911001175 (visited on 05/14/2025).

[47] Akio Tomiyama et al. 'Transverse migration of single bubbles in simple shear flows'. In: *Chemical Engineering Science* 57.11 (June 1, 2002), pp. 1849–1858. ISSN: 0009-2509. DOI: 10.1016/S0009-2509(02)00085-4. URL: https://www.sciencedirect.com/science/article/pii/S0009250902000854 (visited on 01/31/2025).

[48] R. M. Wellek, A. K. Agrawal, and A. H. P. Skelland. 'Shape of liquid drops moving in liquid media'. In: *AIChE Journal* 12.5 (1966), pp. 854–862. ISSN: 1547-5905. DOI: 10.1002/aic.690120506. URL: https://onlinelibrary.wiley.com/doi/abs/10.1002/aic.690120506 (visited on 10/09/2024).

[49] Yixiang Liao and Dirk Lucas. 'A literature review of theoretical models for drop and bubble breakup in turbulent dispersions'. In: *Chemical Engineering Science* 64.15 (Aug. 1, 2009), pp. 3389–3406. ISSN: 0009-2509. DOI: 10.1016/j.ces.2009.04.026. URL: https://www.sciencedirect.com/science/article/pii/S0009250909002759 (visited on 09/26/2024).

[50] Yixiang Liao and Dirk Lucas. 'A literature review on mechanisms and models for the coalescence process of fluid particles'. In: *Chemical Engineering Science* 65.10 (May 15, 2010), pp. 2851–2864. ISSN: 0009-2509. DOI: 10.1016/j.ces.2010.02.020. URL: https://www.sciencedirect.com/science/article/pii/S000925091000093X (visited on 10/03/2024).

[51] Timothy O. Oolman and Harvey W. Blanch. 'Bubble Coalescence in Stagnant Liquids'. In: *Chemical Engineering Communications* 43.4 (May 1, 1986), pp. 237–261. ISSN: 0098-6445. DOI: 10.1080/00986448608911334. URL: https://doi.org/10.1080/00986448608911334 (visited on 11/01/2024).

[52] Michael J. Prince and Harvey W. Blanch. 'Bubble coalescence and break-up in air-sparged bubble columns'. In: *AIChE Journal* 36.10 (1990), pp. 1485–1499. ISSN: 1547-5905. DOI: 10.1002/aic.690361004. URL: https://onlinelibrary.wiley.com/doi/abs/10.1002/aic.690361004 (visited on 10/17/2024).

[53] L.P.B.M. Janssen and M.M.C.G. Warmoeskerken. *Transport Phenomena Data Companion*. 3rd. Delft, Netherlands: VSSD, 2006. ISBN: 978-90-71301-59-9.

[54] J. O. Hinze. 'Fundamentals of the hydrodynamic mechanism of splitting in dispersion processes'. In: *AIChE Journal* 1.3 (1955), pp. 289–295. ISSN: 1547-5905. DOI: 10.1002/aic.690010303. URL: https://onlinelibrary.wiley.com/doi/abs/10.1002/aic.690010303 (visited on 09/26/2024).

[55] Julius C. Rotta. 'Turbulente Scherströmungen'. In: *Turbulente Strömungen: Eine Einführung in die Theorie und ihre Anwendung*. Ed. by Julius C. Rotta. Wiesbaden: Vieweg und Teubner Verlag, 1972, pp. 127–186. ISBN: 978-3-322-91206-0. URL: https://doi.org/10.1007/978-3-322-91206-0_3 (visited on 10/28/2024).

[56] Ryoichi Kuboi, Isao Komasawa, and Tsutao Otake. 'Behavior of Dispersed Particles in Turbulent Liquid Flow'. In: *Journal of Chemical Engineering of Japan* 5.4 (1972), pp. 349–355. DOI: 10.1252/jcej.5.349.

[57] S. M. Bhavaraju, T. W. F. Russell, and H. W. Blanch. 'The design of gas sparged devices for viscous liquid systems'. In: *AIChE Journal* 24.3 (1978), pp. 454–466. ISSN: 1547-5905. DOI: 10.1002/aic.690240310. URL: https://onlinelibrary.wiley.com/doi/abs/10.1002/aic.690240310 (visited on 10/29/2024).

[58] Yannic Mast and Ralf Takors. 'Transferring Bubble Breakage Models Tailored for Euler-Euler Approaches to Euler-Lagrange Simulations'. In: *Processes* 11.4 (Apr. 2023), p. 1018. ISSN: 2227-9717. DOI: 10.3390/pr11041018. URL: https://www.mdpi.com/2227-9717/11/4/1018 (visited on 09/30/2024).

[59] F. Lehr, M. Millies, and D. Mewes. 'Bubble-Size distributions and flow fields in bubble columns'. In: *AIChE Journal* 48.11 (2002), pp. 2426–2443. ISSN: 1547-5905. DOI: 10.1002/aic.690481103. URL: https://onlinelibrary.wiley.com/doi/abs/10.1002/aic.690481103 (visited on 09/26/2024).

[60] Boris Boshenyatov. 'Laws of Bubble Coalescence and their Modeling'. In: *New Developments in Hydrodynamics Research*. Aug. 1, 2012, pp. 211–240.

[61] Boris Boshenyatov. 'LAWS OF BUBBLE COALESCENCE AND THEIR MODELING'. In: *Journal of Magnetohydrodynamics and Plasma Research* 18.4 (Oct. 1, 2013), p. 331. ISSN: 10834729.

[62] John A. Thomas et al. 'A mechanistic approach for predicting mass transfer in bioreactors'. In: *Chemical Engineering Science* 237 (June 29, 2021), p. 116538. ISSN: 0009-2509. DOI: 10.1016/j.ces.2021.116538. URL: https://www.sciencedirect.com/science/article/pii/S0009250921001032 (visited on 10/30/2024).

[63] Roman Zakrzewski. 'Development of a novel scale-down method to study pH and dissolved oxygen heterogeneities in mammalian cell cultures'. Doctoral. UCL (University College London), Oct. 28, 2022. 239 pp. URL: https://discovery.ucl.ac.uk/id/eprint/10157903/ (visited on 10/30/2024).

[64] Hooman Yadollahi Farsani et al. ‘Modeling mass transfer in stirred microbioreactors’. In: *Chemical Engineering Science* 248 (Feb. 2, 2022), p. 117146. ISSN: 0009-2509. DOI: 10.1016/j.ces.2021.117146. URL: https://www.sciencedirect.com/science/article/pii/S0009250921007119 (visited on 10/03/2024).

[65] D. Eijsberg. ‘A Lattice-Boltzmann CFD study of the hydrodynamics relevant for industrial fermentation processes’. M.Sc. thesis. Delft, Netherlands: TU Delft, Feb. 2, 2023. URL: https://resolver.tudelft.nl/uuid:06afea4a-bd83-4596-ba7d-50952f2103bc (visited on 10/31/2024).

[66] Christopher L. Oliveira et al. ‘CFD-based bioreactor model with proportional–integral–derivative controller functionality for dissolved oxygen and pH’. In: *Biotechnology and Bioengineering* 121.2 (2024), pp. 655–669. ISSN: 1097-0290. DOI: 10.1002/bit.28598. URL: https://onlinelibrary.wiley.com/doi/abs/10.1002/bit.28598 (visited on 10/31/2024).

[67] Christian Weiland, Alexandra von Kameke, and Michael Schlüter. ‘Trajectory-based breakup modelling for dense bubbly flows’. In: *Chemical Engineering Journal* 499 (Nov. 1, 2024), p. 155726. ISSN: 1385-8947. DOI: 10.1016/j.cej.2024.155726. URL: https://www.sciencedirect.com/science/article/pii/S1385894724072176 (visited on 10/31/2024).

[68] Martin Sommerfeld, Evgueni Bourloutski, and Dirk Bröder. ‘Euler/Lagrange Calculations of Bubbly Flows with Consideration of Bubble Coalescence’. In: *The Canadian Journal of Chemical Engineering* 81.3 (2003), pp. 508–518. ISSN: 1939-019X. DOI: 10.1002/cjce.5450810324. URL: https://onlinelibrary.wiley.com/doi/abs/10.1002/cjce.5450810324 (visited on 10/29/2024).

[69] J. C. Lee and T. D. Hodgson. ‘Film flow and coalescence-I Basic relations, film shape and criteria for interface mobility’. In: *Chemical Engineering Science* 23.11 (Nov. 1, 1968), pp. 1375–1397. ISSN: 0009-2509. DOI: 10.1016/0009-2509(68)89047-5. URL: https://www.sciencedirect.com/science/article/pii/0009250968890475 (visited on 11/07/2024).

[70] Chung-Hur Lee, L.E. Erickson, and L.A. Glasgow. ‘Bubble Breakup and Coalescence in Turbulent Gas-Liquid Dispersions’. In: *Chemical Engineering Communications* 59.1 (Sept. 1, 1987), pp. 65–84. ISSN: 0098-6445. DOI: 10.1080/00986448708911986. URL: https://doi.org/10.1080/00986448708911986 (visited on 10/31/2024).

[71] Stijn Rommens. ‘Effect of Salts on Gas Bubble Sizes: Investigating the Role of Ion Redistribution Along the G/L-Interface to Explain Bubble Coalescence Inhibition in Bubble Columns’. M.Sc. thesis. Delft, Netherlands: TU Delft, June 2023.

[72] Per Christian Hansen, Jakob Jorgensen, and William R. B. Lionheart. *Computed Tomography: Algorithms, Insight, and Just Enough Theory*. SIAM, Sept. 25, 2021. 356 pp. ISBN: 978-1-61197-667-0.

[73] Jens Gregor and Jeffrey A. Fessler. ‘Comparison of SIRT and SQS for Regularized Weighted Least Squares Image Reconstruction’. In: *IEEE transactions on computational imaging* 1.1 (Mar. 2015), pp. 44–55. ISSN: 2333-9403. DOI: 10.1109/TCI.2015.2442511. URL: https://www.ncbi.nlm.nih.gov/pmc/articles/PMC4608542/ (visited on 12/06/2024).

[74] Jacques Hadamard. ‘Sur les problèmes aux dérivées partielles et leur signification physique’. In: *Princeton university bulletin* (1902), pp. 49–52.

[75] A. van der Sluis and H. A. van der Vorst. 'SIRT- and CG-type methods for the iterative solution of sparse linear least-squares problems'. In: *Linear Algebra and its Applications* 130 (Mar. 1, 1990), pp. 257–303. ISSN: 0024-3795. DOI: 10.1016/0024-3795(90)90215-X. URL: https://www.sciencedirect.com/science/article/pii/002437959090215X (visited on 12/11/2024).

[76] Marcel Beister, Daniel Kolditz, and Willi A. Kalender. 'Iterative reconstruction methods in X-ray CT'. In: *Physica Medica: European Journal of Medical Physics* 28.2 (Apr. 1, 2012), pp. 94–108. ISSN: 1120-1797, 1724-191X. DOI: 10.1016/j.ejmp.2012.01.003. URL: https://www.physicamedica.com/article/S1120-1797(12)00004-X/fulltext (visited on 12/09/2024).

[77] Peter Gilbert. 'Iterative methods for the three-dimensional reconstruction of an object from projections'. In: *Journal of Theoretical Biology* 36.1 (July 1, 1972), pp. 105–117. ISSN: 0022-5193. DOI: 10.1016/0022-5193(72)90180-4. URL: https://www.sciencedirect.com/science/article/pii/0022519372901804 (visited on 12/11/2024).

[78] Victor S. Ryaben'kii and Semyon V. Tsynkov. *A Theoretical Introduction to Numerical Analysis*. New York: Chapman and Hall/CRC, Nov. 2, 2006. 552 pp. ISBN: 978-0-429-14339-7. DOI: 10.1201/9781420011166.

[79] Per Christian Hansen and Jakob Sauer Jørgensen. 'AIR Tools II: algebraic iterative reconstruction methods, improved implementation'. In: *Numerical Algorithms* 79.1 (Sept. 1, 2018), pp. 107–137. ISSN: 1572-9265. DOI: 10.1007/s11075-017-0430-x. URL: https://doi.org/10.1007/s11075-017-0430-x (visited on 12/11/2024).

[80] Tommy Elfving, Per Christian Hansen, and Touraj Nikazad. 'Semiconvergence and Relaxation Parameters for Projected SIRT Algorithms'. In: *SIAM Journal on Scientific Computing* 34.4 (Jan. 2012), A2000–A2017. ISSN: 1064-8275. DOI: 10.1137/110834640. URL: https://epubs.siam.org/doi/10.1137/110834640 (visited on 01/16/2025).

[81] Per Christian Hansen, Jakob Sauer Jørgensen, and Peter Winkel Rasmussen. 'Stopping Rules for Algebraic Iterative Reconstruction Methods in Computed Tomography'. In: *2021 21st International Conference on Computational Science and Its Applications (ICCSA)*. 2021 21st International Conference on Computational Science and Its Applications (ICCSA). Sept. 2021, pp. 60–70. DOI: 10.1109/ICCSA54496.2021.00019. URL: https://ieeexplore.ieee.org/document/9732394 (visited on 04/25/2025).

[82] Antonin Chambolle and Thomas Pock. 'A First-Order Primal-Dual Algorithm for Convex Problems with Applications to Imaging'. In: *Journal of Mathematical Imaging and Vision* 40.1 (May 1, 2011), pp. 120–145. ISSN: 1573-7683. DOI: 10.1007/s10851-010-0251-1. URL: https://doi.org/10.1007/s10851-010-0251-1 (visited on 01/17/2025).

[83] Pierre Paleo. *pierrepaleo/ChambollePock*. Nov. 19, 2024. URL: https://github.com/pierrepaleo/ChambollePock (visited on 12/19/2024).

[84] Emeric Boigné, Dilworth Y. Parkinson, and Matthias Ihme. 'Towards Data-Informed Motion Artifact Reduction in Quantitative CT Using Piecewise Linear Interpolation'. In: *IEEE Transactions on Computational Imaging* 8 (2022), pp. 917–932. ISSN: 2333-9403. DOI: 10.1109/TCI.2022.3215096. URL: https://ieeexplore.ieee.org/document/9920189 (visited on 01/20/2025).

[85] Delft High Performance Computing Centre (DHPC). *DelftBlue Supercomputer (Phase 2)*. https://www.tudelft.nl/dhpc/ark:/44463/DelftBluePhase2. 2024.

[86] Peter M. Wilkinson, Arie P. Spek, and Laurent L. van Dierendonck. 'Design parameters estimation for scale-up of high-pressure bubble columns'. In: *AIChE Journal* 38.4 (1992), pp. 544–554. ISSN: 1547-5905. DOI: 10.1002/aic.690380408. URL: https://onlinelibrary.wiley.com/doi/abs/10.1002/aic.690380408 (visited on 05/09/2025).

[87] Nicholas W. Geary and Richard G. Rice. 'Bubble size prediction for rigid and flexible spargers'. In: *AIChE Journal* 37.2 (1991), pp. 161–168. ISSN: 1547-5905. DOI: 10.1002/aic.690370202. URL: https://onlinelibrary.wiley.com/doi/abs/10.1002/aic.690370202 (visited on 09/13/2024).

[88] Mattia Polli et al. 'Bubble size distribution in the sparger region of bubble columns'. In: *Chemical Engineering Science* 57.1 (Jan. 1, 2002), pp. 197–205. ISSN: 0009-2509. DOI: 10.1016/S0009-2509(01)00301-3. URL: https://www.sciencedirect.com/science/article/pii/S0009250901003013 (visited on 09/17/2024).

[89] *Critical Surface Tension and Contact Angle with Water for Various Polymers (sort by contact angle)*. URL: https://www.accudynetest.com/polytable_03.html?sortby=contact_angle (visited on 01/27/2025).

[90] Hongyu Zhang et al. 'MC3T3-E1 cell response to stainless steel 316L with different surface treatments'. In: *Materials Science and Engineering: C* 56 (Nov. 1, 2015), pp. 22–29. ISSN: 0928-4931. DOI: 10.1016/j.msec.2015.06.017. URL: https://www.sciencedirect.com/science/article/pii/S0928493115301442 (visited on 01/27/2025).

[91] Martin Geier et al. 'The cumulant lattice Boltzmann equation in three dimensions: Theory and validation'. In: *Computers & Mathematics with Applications* 70.4 (Aug. 1, 2015), pp. 507–547. ISSN: 0898-1221. DOI: 10.1016/j.camwa.2015.05.001. URL: https://www.sciencedirect.com/science/article/pii/S0898122115002126 (visited on 11/28/2024).

[92] Maike Kuschel et al. 'Validation of Novel Lattice Boltzmann Large Eddy Simulations (LB LES) for Equipment Characterization in Biopharma'. In: *Processes* 9.6 (June 2021), p. 950. ISSN: 2227-9717. DOI: 10.3390/pr9060950. URL: https://www.mdpi.com/2227-9717/9/6/950 (visited on 10/10/2024).

[93] Wim van Aarle et al. 'The ASTRA Toolbox: A platform for advanced algorithm development in electron tomography'. In: *Ultramicroscopy* 157 (Oct. 1, 2015), pp. 35–47. ISSN: 0304-3991. DOI: 10.1016/j.ultramic.2015.05.002. URL: https://www.sciencedirect.com/science/article/pii/S0304399115001060 (visited on 04/04/2025).

[94] Wim van Aarle et al. 'Fast and flexible X-ray tomography using the ASTRA toolbox'. In: *Optics Express* 24.22 (Oct. 31, 2016), pp. 25129–25147. ISSN: 1094-4087. DOI: 10.1364/OE.24.025129. URL: https://opg.optica.org/oe/abstract.cfm?uri=oe-24-22-25129 (visited on 04/04/2025).

[95] Sailesh B Kumar. 'Computed Tomographic Measurements of Void Fraction and Modeling of the Flow in Bubble Columns'. PhD thesis. Boca Raton, Florida, USA: Florida Atlantic University, Dec. 1994. URL: https://www.proquest.com/openview/5d34b78fae8b0c52366b0abfd63fde3b.

[96] B. C. Ong et al. 'Computed Tomographic Investigation of the Influence of Gas Sparger Design on Gas Holdup Distribution in a Bubble Column'. In: *Industrial & Engineering Chemistry Research* 48.1 (Jan. 7, 2009), pp. 58–68. ISSN: 0888-5885. DOI: 10.1021/ie800516s. URL: https://doi.org/10.1021/ie800516s (visited on 09/24/2024).

[97] M. C Ruzicka et al. 'Homogeneous–heterogeneous regime transition in bubble columns'. In: *Chemical Engineering Science* 56.15 (Aug. 1, 2001), pp. 4609–4626. ISSN: 0009-2509. DOI: 10.1016/S0009-2509(01)00116-6. URL: https://www.sciencedirect.com/science/article/pii/S0009250901001166 (visited on 02/03/2025).

[98] Osborne Reynolds. 'IV. On the dynamical theory of incompressible viscous fluids and the determination of the criterion'. In: *Philosophical Transactions of the Royal Society of London. (A.)* 186 (Jan. 1, 1895), pp. 123–164. DOI: 10.1098/rsta.1895.0004. URL: https://royalsocietypublishing.org/doi/abs/10.1098/rsta.1895.0004 (visited on 04/11/2025).

[99] Paul Rodriguez and Brendt Wohlberg. 'Efficient Minimization Method for a Generalized Total Variation Functional'. In: *IEEE Transactions on Image Processing* 18.2 (Feb. 2009), pp. 322–332. ISSN: 1941-0042. DOI: 10.1109/TIP.2008.2008420. URL: https://ieeexplore.ieee.org/abstract/document/4729670 (visited on 05/07/2025).

[100] Gürol Canbek, Tugba Taskaya Temizel, and Seref Sagiroglu. 'PToPI: A Comprehensive Review, Analysis, and Knowledge Representation of Binary Classification Performance Measures/Metrics'. In: *SN Computer Science* 4.1 (Oct. 16, 2022), p. 13. ISSN: 2661-8907. DOI: 10.1007/s42979-022-01409-1. URL: https://doi.org/10.1007/s42979-022-01409-1 (visited on 05/07/2025).

[101] Daniel Berrar. *Performance Measures for Binary Classification*. May 20, 2024. DOI: 10.1016/B978-0-12-809633-8.20351-8. URL: https://dberrar.github.io/papers/Berrar_EBCB_2nd_edition_Performance_Measures_preprint.pdf (visited on 05/06/2024).

[102] Konstantin Bulatov et al. 'Monitored Reconstruction: Computed Tomography as an Anytime Algorithm'. In: *IEEE Access* 8 (2020), pp. 110759–110774. ISSN: 2169-3536. DOI: 10.1109/ACCESS.2020.3002019. URL: https://ieeexplore.ieee.org/abstract/document/9115485 (visited on 09/23/2024).

A

M-Star code review / implementation

A.1. Mast and Takors bubble breakup model

Code from the supplemental materials from ”Novel experimental data-driven bubble breakage model for universal application in Euler-Lagrange multiphase frameworks” by Yannic Mast and Ralf Takors (2024). [17].

Modifications

- The usage of double precision floating point numbers for a function evaluated on the GPU is questionable.
- The sum of the random number ”rand” on line 22 leads to a random number in the range [0, 0.555], which in turn leads to an over-prediction of symmetric bubble breaks.
- The usage of a constant EDR (line 4) in the DSD is justified in a previous paper of Mast and Takors by stating: ‘The influence of ε on the original DSD was smaller compared to d, as indicated by the exponents in [equation (2.28) in section 2.2.2]. The effect of ε on DSD was therefore neglected entirely by replacing it with a constant.’[58] The modified model includes a variable ε based on the local variable considering the negligible computational burden of having it be included.

Original code

```
double di;
double integral[500];
double fb;
double ep=.65;
double st=0.072;
double density=1000.0;
double We=density*powf(e,.666667)*powf(d_p,1.6666667)/st;

if(We>6.1&&tsb_p>.03){
        doBreakup=true;
        for (int i=1;i<500;i++){
                di=d_p*powf(((double)(i)/1000),(1.0/3.0));
                integral[i]=.5641895/((double)(i)/1000)*exp(-9.0/4.0*powf(log(di
                    *1.319508*powf(ep,(2.0/5.0))*powf(density,(3.0/5.0))/powf(st
                    ,(3.0/5.0))),2));
                integral[i]=integral[i]/(1+erf((3.0/2.0*(log(d_p*1.04729*powf(
                    density,(3.0/5.0))*powf(ep,(2.0/5.0))/powf(st,(3.0/5.0)))))));
        }
        for (int i=1;i<500;i++){
                integral[i]=integral[i-1]+integral[i];
        }
        for (int i=1;i<500;i++){
                integral[i]=integral[i]/integral[499]/2;
        }
        double rn=rand+rand/10+rand/100;
        int  i=1;
        while (!(rn<integral[i-1])&&(i<500)){
                i=i+1;
        }
        fb=((double)(i)/1000);

        fv=fb;

}
```

Modified code

```
//note: since this expression is executed on the GPU, using double precision
    floats are not feasible.
float di; // daughter bubble diameter                    [m]
float integral[500];
const float sigma=0.072; // surface tension              [N m-2]
const float density=1000.0; // fluid density    [kg m-3]

// calculate dimensionless turbulent Weber number
float We=density*powf(e,.666667)*powf(d_p,1.6666667)/sigma;

if(We>6.1 && tsb_p>.03){ // When We is larger than 6.1 and no break-up has occured
     for more than .03 seconds, enact breakup
        doBreakup=true;
        // Calculate the DSD, based on Lehr et al.
        for (int i=1;i<500;i++){
                di=d_p*powf(((float)(i)/1000),(1.0/3.0));
                integral[i]=.5641895/((float)(i)/1000)*exp(-9.0/4.0*powf(log(di
                    *1.319508*powf(e,(2.0/5.0))*powf(density,(3.0/5.0))/powf(sigma
                    ,(3.0/5.0))),2));
                integral[i]=integral[i]/(1+erf((3.0/2.0*(log(d_p*1.0472941*powf(
                    density,(3.0/5.0))*powf(e,(2.0/5.0))/powf(sigma,(3.0/5.0)))))))
                    ;
        }
```

```
        for (int i=1;i<500;i++){
                integral[i]=integral[i-1]+integral[i];
        }
        for (int i=1;i<500;i++){
                integral[i]=integral[i]/integral[499]/2;
        }
        int  i=1;
        while (!(rand<integral[i-1])&&(i<500)){
                i++;
        }
        fv=((float)(i)/1000);
}
```

A.2. Sommerfeld bubble coalescence model

```
const float Cc = 0.25; // constant for contact time     [-]

const float sigma = 0.072; // surface tension           [N m-2]

const float h0 = 1e-3; // initial film thickness        [m]
const float hf = 1e-6; // final film thickness          [m]

float un; // normal component collison velocity         [m s-1]

{
    float dvij_x = vx_p1 - vx_p2;
    float dvij_y = vy_p1 - vy_p2;
    float dvij_z = vz_p1 - vz_p2;

    float dxij = x_p1 - x_p2;
    float dyij = y_p1 - y_p2;
    float dzij = z_p1 - z_p2;

    un = (dvij_x*dxij + dvij_y*dyij + dvij_z*dzij)*rnorm3df(dxij, dyij, dzij);
}

float Rij = d_p1*d_p2 / (d_p1 + d_p2); // compute harmonic mean radius [m]

float t_drain = powf(rho * Rij * Rij * Rij / (16 * sigma), 0.5) * logf(h0/hf); //
    drainage time [s]
float t_cont = Cc * Rij / un; // contact time [s]

doCoalesce = (t_drain <= t_cont); // Coalescence condition
```

B

Hadamard Criteria

The Hadamard criteria [74] in the context of our problem can be defined as follows:

1. A solution exists; for the image vector, there exist a object vector which solves the problem.
2. The solution is unique; for the image vector, there exist only one associated object which solves the problem.
3. The solution is stable; for a large or small change in the image vector, there is a proportional change in the object vector.

The first Hadamard criterium can be addressed by solving the least-squares problem shown in equation (B.1) rather than directly solving the linear system, since it provides a solution even when the system is inconsistent. The least-squares solution $\boldsymbol{x}_{LS}$ is the solution such that residual vector $\boldsymbol{b} - \boldsymbol{A}\boldsymbol{x}_{LS}$ is minimised and orthogonal to the range of $\boldsymbol{A}$.

$$\min_{\boldsymbol{x}} \|\boldsymbol{A}\boldsymbol{x} - \boldsymbol{b}\|_2^2 \tag{B.1}$$

The second criterium becomes relevant when $\boldsymbol{A}$ is underdetermined, since an underdetermined system has infinitely many least-squares solutions. The system matrix $\boldsymbol{A}$ is underdetermined when the rank of the matrix r is less than the number of columns N. CT problems are generally rank deficient, especially when using angle-limited data. This can be resolved by applying additional constraints to the solution through regularisation based on prior knowledge of the system. Methods of regularisation are explored in detail in section 2.3.2. Methods such as SIRT converge to the minimum-norm least-squares solution when a null-vector is used as the initial object vector [75]. The minimum-norm least-squares solution refers to the solution with the smallest $\|\boldsymbol{x}\|$ which satisfies the least-square solution. The advantage of the minimum-norm least-squares solution is that it has no components in the null space of the system matrix and hopefully all components of the solution can be attributed to the data [79, pp. 32-33]. The minimum-norm least-squares solution $\boldsymbol{x}_{LS}^0$ is defined as follows (equation (B.2)):

$$\boldsymbol{x}_{LS} = \arg\min_{x} \|x\|_2 \quad \text{subject to} \quad \boldsymbol{A}^T\boldsymbol{A}\boldsymbol{x} = \boldsymbol{A}^T\boldsymbol{b} \tag{B.2}$$

The third and final criterium can be quantified using the condition number κ. Let $\bar{\boldsymbol{x}}$ and $\bar{\boldsymbol{b}}$ be the ground truth for the object and image vectors and let $\boldsymbol{e}$ be a perturbation (error) vector in

$\boldsymbol{b}$ (equation (B.3)). The condition number represents the upper bound of by how much a perturbation in the image vector $\boldsymbol{b}$ is amplified in the reconstructed object vector (equation (B.4)). The condition number κ of a problem can be calculated based on the product of the matrix norms $\|\cdot\|$ of the matrix $\boldsymbol{A}$ and its inverse $\boldsymbol{A}^{-1}$ or its Moore-Penrose pseudoinverse if the matrix is not invertible $\boldsymbol{A}^{\dagger}$.

$$\boldsymbol{A}\bar{\boldsymbol{x}} = \bar{\boldsymbol{b}}, \quad \boldsymbol{A}\boldsymbol{x} = \boldsymbol{b} = \bar{\boldsymbol{b}} + \boldsymbol{e} \tag{B.3}$$

$$\frac{\|\boldsymbol{x} - \bar{\boldsymbol{x}}\|}{\|\bar{\boldsymbol{x}}\|} \leq \mathrm{Cond}(\boldsymbol{A}) \frac{\|\boldsymbol{e}\|}{\|\bar{\boldsymbol{b}}\|} \tag{B.4}$$

$$\mathrm{Cond}(\boldsymbol{A}) = \|\boldsymbol{A}\|\|\boldsymbol{A}^{-1}\| \quad or \quad \|\boldsymbol{A}\|\|\boldsymbol{A}^{\dagger}\| \tag{B.5}$$

In the L^2-norm, the condition number can be calculated based on the maximum and minimum singular values of the matrix $\boldsymbol{A}$ using Singular Value Decomposition (SVD) (equations (B.6) to (B.8)). The matrix $\boldsymbol{A}$ is considered ill-conditioned when the condition number is large. This means that the reconstruction is very sensitive to noise in the image data as is shown in equation (B.4). If the condition number is infinite or higher than machine accuracy, the least-squares problem is not solvable without regularisation. This also explains why underdetermined matrices are not solvable without regularisation, as rank-deficient matrices have $r - n$ number of 0 valued singular values. Regularisation methods, such as Tikhonov regularisation and the implicit regularisation of iterative methods, address this problem by filtering low singular values such that the matrix condition improves.

$$\boldsymbol{A} = \boldsymbol{U}\boldsymbol{\Sigma}\boldsymbol{V}^T, \quad \boldsymbol{A}^{\dagger} = \boldsymbol{V}\boldsymbol{\Sigma}^{-1}\boldsymbol{U}^T \tag{B.6}$$

$$\boldsymbol{\Sigma} = diag(\sigma_i, \sigma_{i+1}, \ldots, \sigma_N), \quad with\ \sigma_i \geq \sigma_{i+1} \geq \cdots \geq \sigma_N \tag{B.7}$$

$$\sigma_{max}(\boldsymbol{A}) = \sigma_0, \quad \sigma_{max}(\boldsymbol{A}^{\dagger}) = \sigma_N^{-1} \equiv \sigma_{min}^{-1}(\boldsymbol{A}) \tag{B.8}$$

$$\begin{aligned} \mathrm{Cond}(\boldsymbol{A}) &= \|\boldsymbol{A}\|_2\|\boldsymbol{A}^{\dagger}\|_2 \\ &= \sigma_{max}(\boldsymbol{A}) \cdot \sigma_{max}(\boldsymbol{A}^{\dagger}) \\ &= \frac{\sigma_{max}(\boldsymbol{A})}{\sigma_{min}(\boldsymbol{A})} \end{aligned} \tag{B.9}$$

C

Shepp-Logan Phathoms

The 3D Shepp-Logan phantom is used to show the performance of the various reconstruction algorithms under idealised conditions at a high number of projection angles (table 3.9).

C.1. Semiconvergence

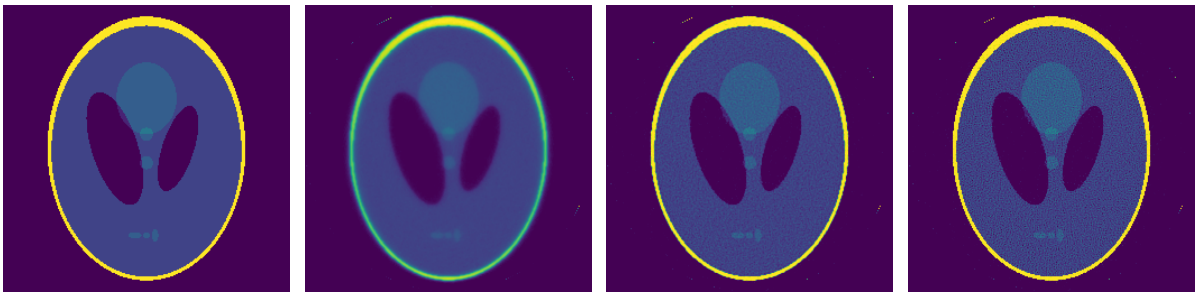

(a) Shepp-Logan phantom ground truth

(b) SIRT reconstruction after 50 iterations.

(c) SIRT reconstruction at semiconvergence according to DP (539 iterations).

(d) SIRT reconstruction after 5000 iterations.

Figure C.1: SIRT reconstructions of the central slice of the 3D Shepp-Logan phantom using 379 angles.

The effects of semiconvergence (see section 2.3.2) in the SIRT method was demonstrated by varying the number of iterations (figure C.1). At lower iterations (figure C.1b), the larger structures are clearly present but the higher frequency structures are yet to be resolved due to the implicit regularisation present in the SIRT method. At very high iterations (figure C.1d), salt and pepper noise appear due to overfitting to high-frequency noise. The discrepancy principle stopping rule is applied to find that semiconvergence is reached after approximately 483 iterations (figure C.1c). This can be verified by plotting the Normalised Root Mean Square Error (NRMSE) of the central slice of the reconstruction over the number of iterations (figure C.2). Here, the NRMSE is defined as the Euclidean norm of the absolute error over the Euclidean norm of the ground truth (equation (C.1)) [102]. The reconstruction error decreases initially but starts increasing after around 850 iterations, while the residual keeps decreasing monotonically even after 5000 iterations.

$$\mathrm{NRMSE} = \frac{\|\boldsymbol{x}^{(k)} - \bar{\boldsymbol{x}}\|_2}{\|\bar{\boldsymbol{x}}\|_2} \tag{C.1}$$

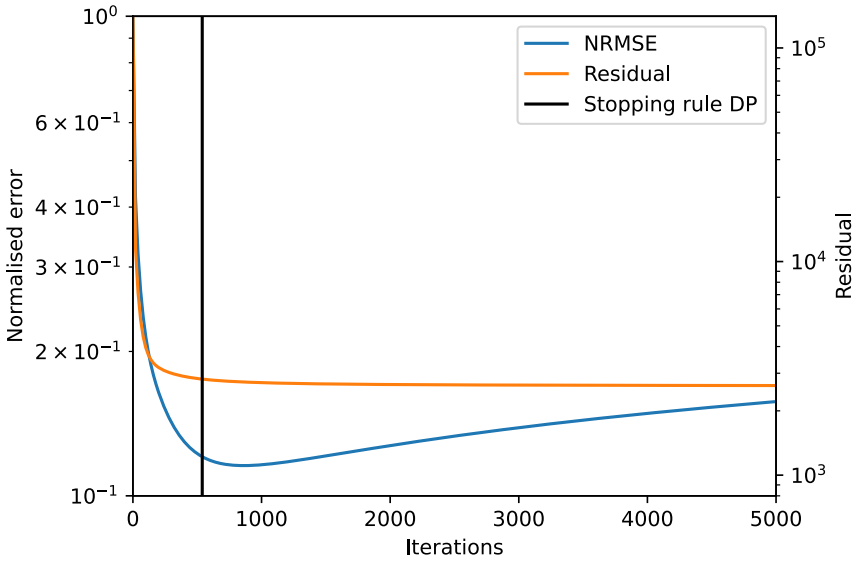

Figure C.2: Illustration of semiconvergence based on the NRMSE of the central slice of the Shepp-Logan phantom reconstruction.

C.2. Regularised methods

The results produced by the SIRT algorithm can be compared to the reconstructions produced by *SIRT+sT*, *SIRT+dT* and *TVmin* reconstruction algorithms. These algorithms apply explicit regularisation. Hence, a regularisation parameter must be set to determine the strength of the regularisation. Varying the strength of regularisation shows the bias introduced into the reconstructions by each methods (figure C.3). All methods are run for 500 iterations, except the *TVmin* algorithm which is given 5000 iterations since it converges more slowly due to the different underlying solving algorithm.

Visually, increasing the regularisation parameter reduces the noise in all reconstructions. Looking at *SIRT+sT*, at high values of α the yellow outer shell is diminished, since standard Tikhonov regularisation pushes the distribution of values to a normal distributions centred on zero. *SIRT+dT* smooths the edges in the reconstruction, as the algorithm attempts to minimise the gradients in the image. Compared to *SIRT+sT*, it leaves the higher attenuation areas at the correct values, except for the thin structures. The TVmin algorithm conserves edges the best, especially at high alpha values, but shows artefacts at lower values. This may be an issue with the implementation of the gradient operator rather than a weakness in the method itself [84].

The reconstruction error can be quantified using the NRMSE between the reconstruction and the ground truth (table C.1). Although all reconstruction algorithms showed a visual reduction in noise, only the *TVmin* algorithm performs well at high regularisation weights. *TVmin* performs well on the Shepp-Logan phantom, since minimising the total variation results in a piecewise function with discrete jumps in the attenuation at edges. The *SIRT+sT* and *SIRT+dT* perform better on phantoms with smoother transitions in attenuation.

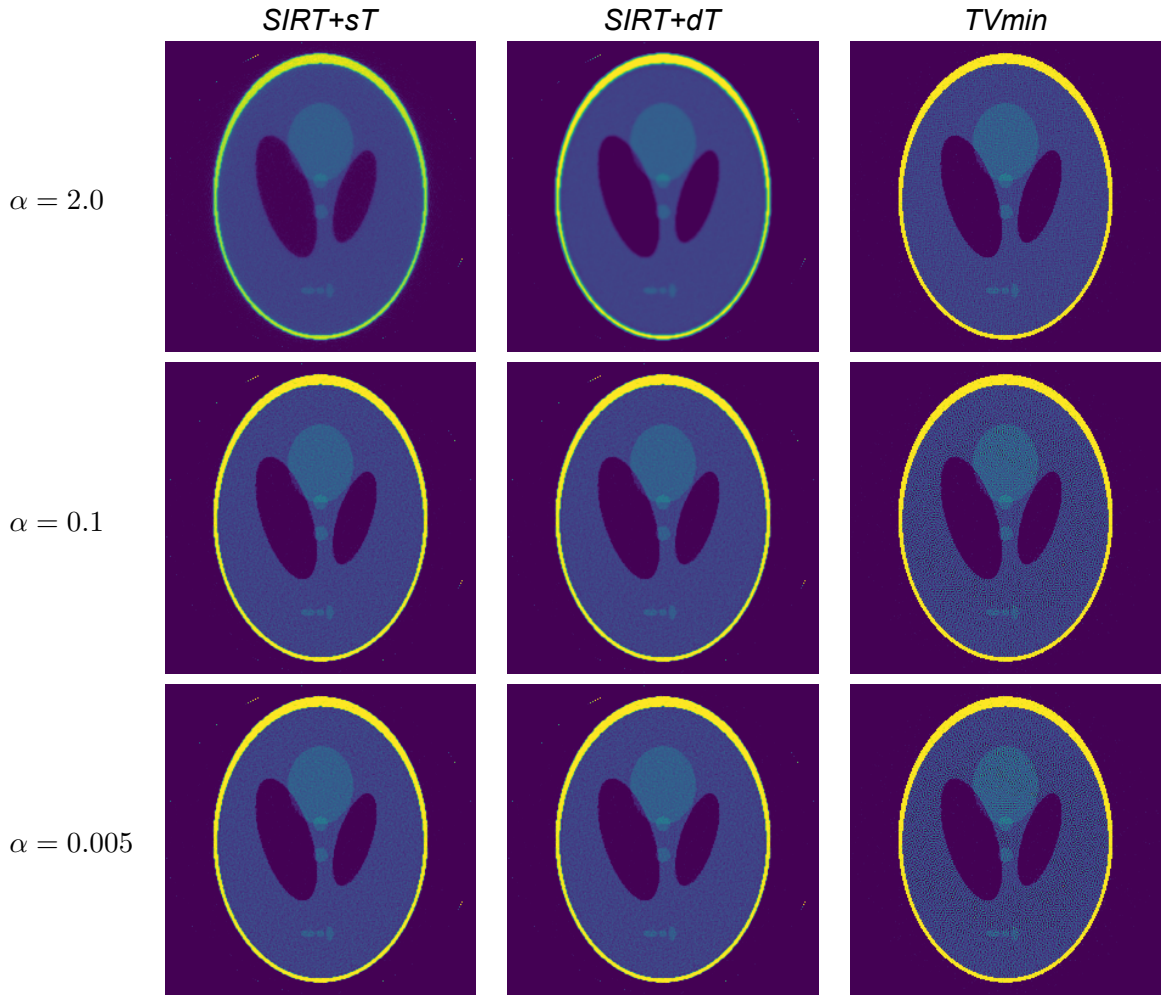

Figure C.3: Effect of the regularisation parameter α for different reconstruction algorithms. Number of angles $= 379$, noise level $= 2\%$, iterations (*SIRT+sT* / *SIRT+dT* / *TVmin*) $= 500, 500, 5000$.

Table C.1: Tabulated reconstruction errors for the reconstruction algorithms on the 3D Shepp-Logan phantom for various regularisation weights.

Regularisation	**Reconstruction algorithms**		
parameter α	*SIRT+sT*	*SIRT+dT*	*TVmin*
2.0	0.214	0.235	0.109
0.1	0.130	0.141	0.228
0.005	0.125	0.126	0.251

D

Additional figures

D.1. LB density
D.2. Fluid kinetic and potential energy
D.3. Density distribution

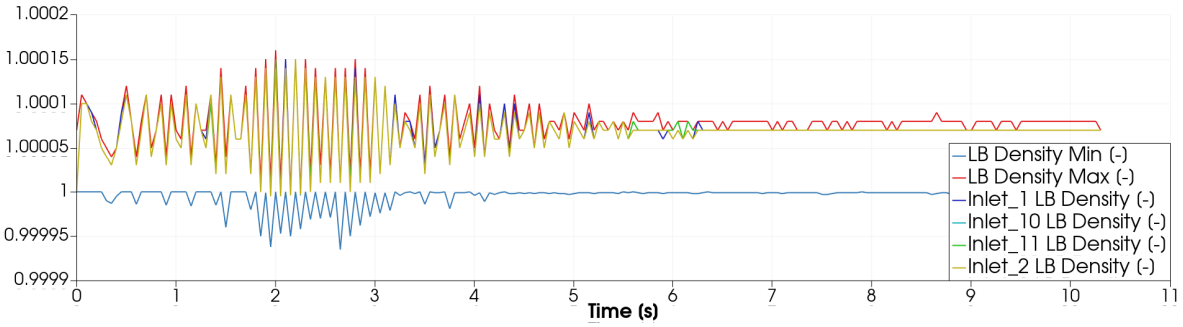

(a) case #3

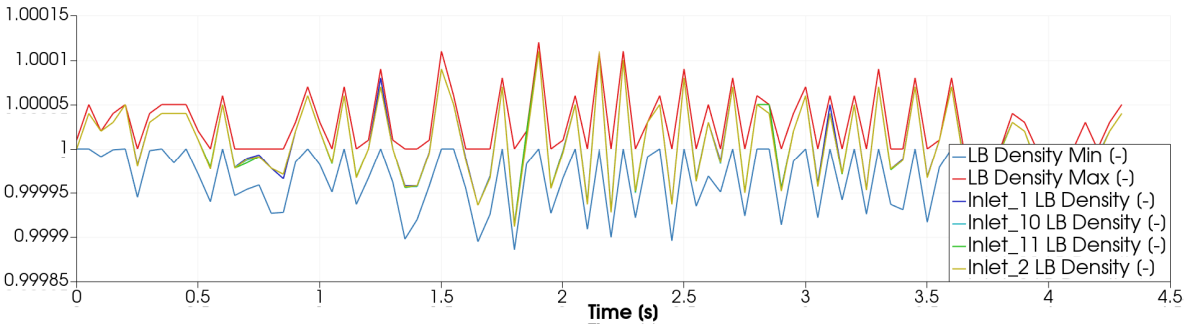

(b) case #4 (incomplete)

Figure D.1: Lattice Boltzmann density over time.

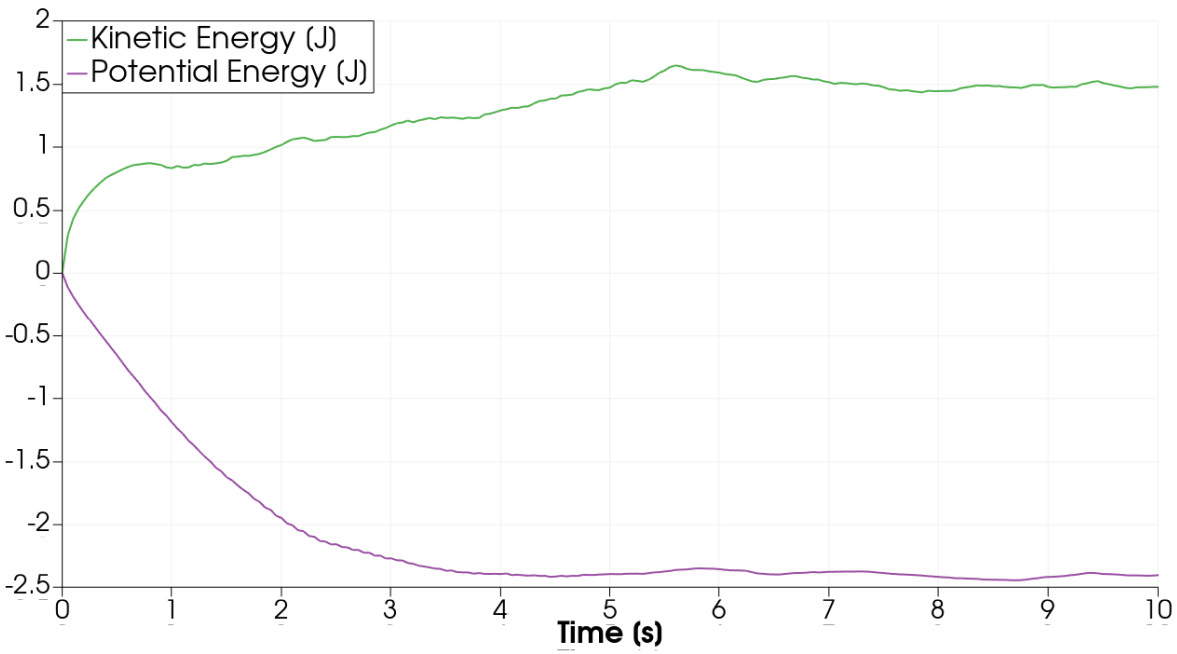

Figure D.2: Fluid kinetic and potential energy (case #3) in Joule over time. Note that the flow reaches energy equilibrium after approximately 5 s.

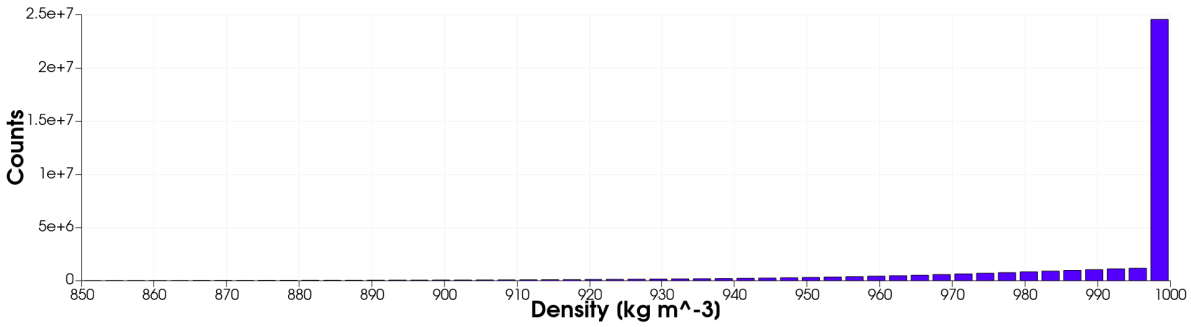

(a) Time-resolved density distribution. $t = 5.545\,\mathrm{s}$.

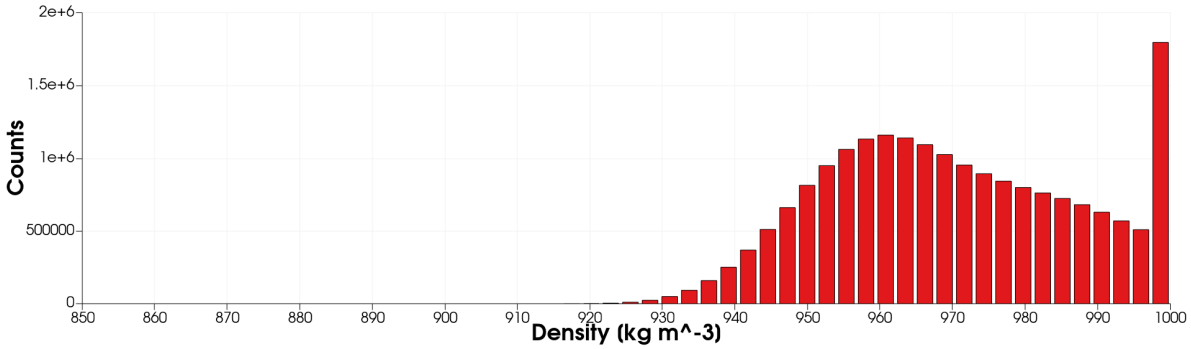

(b) Time-averaged density distribution. $5\,\mathrm{s} \leq t \leq 10\,\mathrm{s}$.

Figure D.3: Distribution of the densities (case #3) above 850 kg m^{-3} for the time-resolved and time-averaged data.